University of California

Santa Barbara

Probing Photocarrier Dynamics with Scanning Ultrafast Electron Microscopy

A dissertation submitted in partial satisfaction

of the requirements for the degree

Doctor of Philosophy

in

Mechanical Engineering

by

Usama Choudhry

Committee in charge:

Professor Bolin Liao, Chair
Professor Samantha Daly
Professor Susanne Stemmer
Professor John Harter

December 2023

The Dissertation of Usama Choudhry is approved.

Professor Samantha Daly

Professor Susanne Stemmer

Professor John Harter

Professor Bolin Liao, Committee Chair

November 2023

Probing Photocarrier Dynamics with Scanning Ultrafast Electron Microscopy

by

Usama Choudhry

Acknowledgements

Graduate research is seldom carried out in isolation, and there are a lot of people who have contributed towards my PhD journey. First, I'd like to thank my advisor Bolin Liao, who hired me as his first student in 2017. He has taught me a great deal about optical spectroscopy, electron microscopy, and building a cutting-edge research laboratory. Bolin's guidance and mentorship has been invaluable, and his continuous drive for knowledge and willingness to explore new ideas has been very inspiring. He has allowed me to approach the problems posed by my projects with a great deal of freedom which has been invaluable to my development as a researcher.

The Liao research group has been a wonderful environment for my graduate studies. I'm particularly grateful to Shengying Yue and Alejandro Vega-Flick for their mentorship during my first few years of study. Yu Li and Taeyong Kim's efforts also contributed a great deal to my research. I'm also thankful to the current SUEM team who's contributions have been integral to my work and who will go on to accomplish many great things with the instrument.

Outside of UCSB, Darin Randall and Jarid Barajas from Thermofisher Scientific have been a great aid to this work. We have made a lot of unique modifications to our SEM which has resulted in a lot of broken equipment and strange requests to our service engineers, and their knowledge and helpfulness has been irreplaceable.

Thank you to my friends, both from back home and here in Santa Barbara. You have challenged and inspired me both in research and in life, and for that I am very grateful. Finally, I would not be where I am now without the love and support of my family, and especially my parents. This thesis would not have been possible without them.

Curriculum Vitæ

Usama Choudhry

Education

2023	Ph.D. in Mechanical Engineering (Expected), University of California, Santa Barbara.
2019	M.S. in Mechanical Engineering, University of California, Santa Barbara.
2016	B.S. in Mechanical Engineering, University of Connecticut

Publications

- T. Kim, S. Park, V. Iyer, B. Shaheen, U. Choudhry, Q. Jiang, G. Eichman, R. Gnabasik, B. Lawrie, K. Zhu and B. L. Liao, "Mapping the pathways of photo-induced ion migration in organic-inorganic hybrid halide perovskites", Nature Communications, **14**, 1846, 2023.

- U. Choudhry, F. Pan, X. He, B. Shaheen, T. Kim, R. Gnabasik, G. A. Gamage, H. Sun, A. Ackerman, D.-S. Yang, Z. Ren and B. L. Liao, "Persistent hot carrier diffusion in boron arsenide single crystals imaged by ultrafast electron microscopy", Matter, **6**, 206, 2023.

- U. Choudhry, T. Kim, M. Adams, J. Ranasinghe, R. Q. Yang and B. L. Liao, "Tutorial: Characterizing microscale energy transport in materials with transient grating spectroscopy", Journal of Applied Physics, **130**, 231101, 2021.

- T. Kim, S. Oh, U. Choudhry, C. Meinhart, M. L. Chabinyc and B. L. Liao, "Transient strain induced electronic structure modulation in a semiconducting polymer imaged by scanning ultrafast electron microscopy", Nano Letters, **21**, 9146, 2021.

- Y. Li, U. Choudhry, J. Ranasinghe, A. Ackerman and B. L. Liao, "Probing surface photovoltage effect using photo-assisted secondary electron emission", Journal of Physical Chemistry A, **124**, 5246, 2020.

- U. Choudhry, S. Y. Yue and B. L. Liao, "Origins of significant reduction of lattice thermal conductivity in graphene allotropes", Physical Review B, **100**, 165401, 2019.

Abstract

Probing Photocarrier Dynamics with Scanning Ultrafast Electron Microscopy

by

Usama Choudhry

The dynamics of photo-excited charge carriers near defects and interfaces plays a fundamental role in determining the efficiency and performance of a wide variety of optoelectronic and solar devices. Conventional optical pump-probe optical spectroscopies possess femtosecond temporal resolution, but their spatial resolution is constrained by the optical diffraction limit. One option to achieve simultaneously high temporal and spatial resolution is to integrate femtosecond lasers with electron microscopes. By coupling femtosecond photon pulses to the cathode in an electron microscope, it is possible to generate ultrafast, sub-picosecond electron pulses that are not constrained by optical diffraction.

Scanning ultrafast electron microscopy (SUEM) is a recently developed photon-pump electron-probe technique that uses short electron pulses to image the response of a sample surface after the impact of a photon pulse. SUEM is highly sensitive to surface charge dynamics, and has been used to study photocarrier diffusion in uniform materials and near interfaces. This dissertation describes the development process of SUEM at UCSB and documents various technical challenges encountered during its construction.

SUEM is then used to visualize the diffusion of photocarriers in BAs, a semiconductor with a unique phonon band structure and ultrahigh thermal conductivity. We

observed ambipolar diffusion at low optical fluence with persistent hot carrier dynamics for above 200 ps, which can likely be attributed to the large frequency gap between acoustic and optical phonons, the same feature that is responsible for the high thermal conductivity. At higher optical fluence, we observed spontaneous electron-hole separation. Our results show BAs is an attractive optoelectronic material combining high thermal conductivity and excellent photocarrier transport properties.

Once thought to be an ordinary semiconductor, α-$RuCl_3$ is a Mott-Hubbard insulator and host to a variety of exotic physics, including predictions of a photoinduced insulator-to-metal transition. We use SUEM to image the response of α-$RuCl_3$ to photoexcitation. At low optical fluences, SUEM images show uniform bright contrast and slow carrier diffusion. At higher fluences, the material response becomes non-linear, potentially due to the predicted phase transition.

This thesis establishes SUEM as a platform to study the spatio-temporal evolution of excited carriers on extreme time and length scales. It then demonstrates its potential to study photocarrier transport in emerging and scientifically relevant systems. Future iterations of SUEM can continue improve upon spatial and temporal resolution and integrate other SEM detectors in order to be expanded into a versatile characterization platform.

Contents

List of Figures

List of Tables

Chapter 1

Introduction

The complex interplay between charge, lattice, and spin degrees of freedom determines the observed electronic properties of materials. These interactions typically occur on timescales ranging from 10^{-18} to 10^{-9} seconds. Maiman's demonstration of stimulated emission from his first ruby laser opened the door to a new paradigm of physics and materials study [1], but it was the later development of Q-switching and mode-locking that pushed pulse widths into the pico- and femtosecond regime [2–6], allowing for the stimulation and probing of matter at extreme timescales. The scope and nature of ultrafast optical spectroscopies is both incredibly deep and far-reaching. Techniques including but not limited to transient absorption and transient grating spectroscopy (TGS) [7] have applications ranging from the study of the dynamics of electrons [8–10], atoms and molecules [11–13], lattice dynamics [14, 15], biological processes [16, 17], and many more. The development of attosecond spectroscopy, for which the Nobel Prize in Physics in 2023 was awarded to Pierre Agostini, Ferenc Krausz, and Anne L'Huillier, further pushes the envelope on temporal resolution and enables the observation of a new regime of electron

dynamics [18–21]. However, while optical spectroscopies have proven to be an invaluable tool for probing material dynamics over the last 50 years, their spatial resolution is fundamentally bounded by the optical diffraction limit.

In microscopy, this issue was circumvented by Max Knoll and Ernst Ruska in 1931 with the development of the electron microscope [22]. Electrons have a de Broglie wavelength of 0.067 Å at 30 keV and 0.025 Å at 200 keV, giving electron microscopes spatial resolution that is limited only by their own design. Various methods to develop sub-picosecond electron pulses were developed from the 1970s through the early 2000s [23], culminating in the development of techniques like ultrafast electron diffraction (UED) [24] and ultrafast electron microscopy (UEM) [25]. While these techniques have simultaneously attained extreme spatial and temporal resolutions, they still have some drawbacks, as UED was designed as a reciprocal space technique and thus lacks any ability to produce real space data sets while UEM is limited in its sensitivity to surface charge carrier concentrations due to the sample preparation requirements of a transmission electron microscope (TEM). In the last decade, scanning ultrafast electron microscopy (SUEM) has been developed in order to address this gap in functionality [26].

In SUEM electron pulses are raster scanned across a sample surface in order to image its state after photoexcitation. The presence of excited carriers modulates the emission of secondary electrons (SEs) from the top few nanometers of the sample surface, allowing SUEM to image the evolution of surface carrier concentrations with nanometer spatial resolution and femtosecond temporal resolution. Since its establishment, SUEM has been used to produce novel studies such as observing carrier dynamics at a p-n junction [27], anisotropic carrier diffusion in 2D materials [28], and the effects of thickness induced band-bending on charge transfer [29].

The purpose of this thesis is to document the development of SUEM at UCSB, advance the understanding of its operation, and apply it to study carrier dynamics in scientifically relevant systems.

This work is organized as follows. Chapter 2 reviews the SUEM literature as well as adjacent techniques including optical spectroscopies and pulsed electron probe experiments like UED and UEM. Chapter 3 describes the development of SUEM at UCSB and details various instrumentation processes and challenges. Chapter 4 presents SUEM experiments on the hot carrier relaxation dynamics in boron arsenide, a material with ultrahigh thermal conductivity and unique phonon properties. Chapter 5 covers a preliminary study on excited carrier dynamics in a Mott-Hubbard insulator and Kitaev candidate material α-$RuCl_3$. Chapter 6 summarizes the thesis and suggests future improvements and potential directions for SUEM.

Chapter 2

Background

2.1 Optical Spectroscopies

Ultrafast optical spectroscopies are a ubiquitous tool for studying dynamical processes in matter. A vast stable of elaborate techniques have been developed ranging from complex spectroscopic techniques to simple pump-probe experiments, allowing for the extraction of a great deal of information on various photo-physical processes. The fundamental principle of pump-probe experiments is quite simple. Two synchronized light pulses are employed, the excitation or "pump" and a delayed "probe". The pump pulse induces a transient change in some material property of the sample, such as its absorptivity or reflectivity, while the probe pulse monitors the change in said property over time. By controlling the delay between the two pulses, the full response of a sample to photoexcitation can be mapped.

Pump-probe experiments have a rich history dating back to 1899, when Abraham and Lemoine used the discharge from condenser plates to concurrently trigger a spark

source and a Kerr-cell shutter [30]. By varying the delay path between their spark source and Kerr cell, they were able to measure the response of the Kerr effect in a carbon disulfide sample. In 1949, Norrish and Porter used flash photolysis, a pump-probe technique which uses light pulses from gas-discharge flash-lamps, to study the intermediates produced in well known photochemical reactions [31]. They received the 1967 Nobel Prize in Chemistry for this work. Ahmed Zewail received the 1999 Nobel Prize in Chemistry for the development of femtochemistry, which pioneered the more extremme temporal resolutions required to resolve molecular motion [32, 33].

Transient absorption (or reflection) spectroscopy is perhaps the most widely utilized and conceptually simple pump-probe technique. In general, a pump pulse excites carriers within a sample from their ground states to an excited state and this rearrangement of carriers results in a change in the absorption of the sample. The delayed probe monitors this change in absorption and by varying the delay time between the two pulses via an optical delay line, the dynamics of the system can be monitored in real time. The nature of the decay in the change of absorption can be used to reconstruct the carrier dynamics of the material. An ideal system might employ tunable pump pulse energies allowing for the excitation of specific transitions and a broadband probe in order to observe as many relaxation channels as possible [34, 35]. This versatility makes transient absorption spectroscopy a very powerful technique, and it has been used to study a diverse array of problems across many fields including biological processes [36–38], semiconductors [39–41], water-splitting [42–45], nanostructures [46–48], and condensed matter systems hosting exotic electronic phases [49–53].

Another optical technique which has been developed in the Liao group at UCSB is transient grating spectroscopy (TGS) [7, 54–56]. In TGS, shown in Fig. 2.1, a pair of optical pump beams are split and then coherently superposed onto a sample. The two

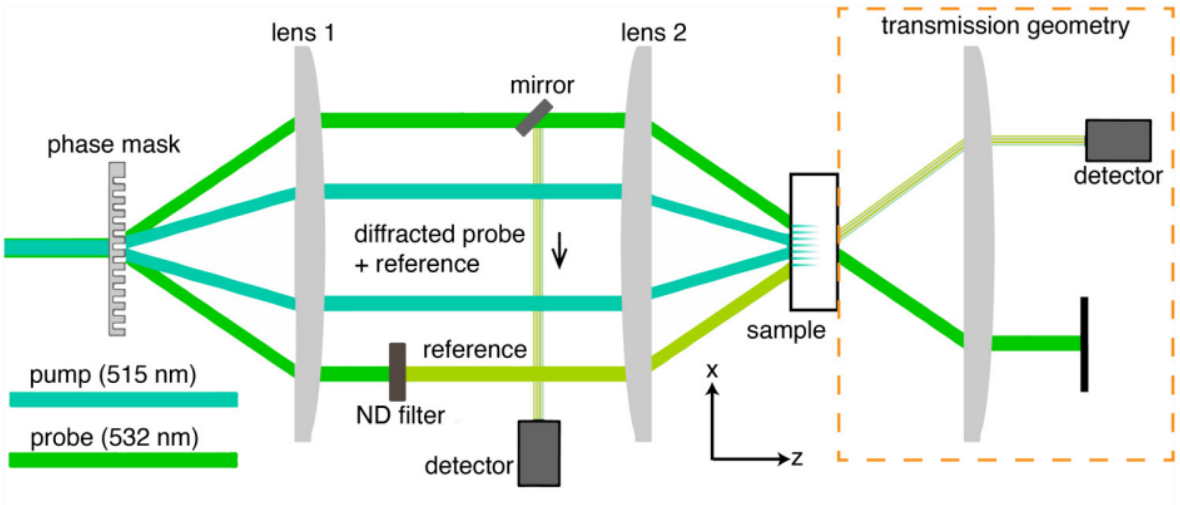

Figure 2.1: **Schematic of Transient Grating Spectroscopy Setup** A schematic of a TGS setup, as configured in the Liao group. Both transmission and reflection geometries can be used based off of sample morphology. The periodicity of the grating can be adjusting using the phase mask. Figure adapted from [7].

pump beams interfere with one another and form a one-dimensional sinusoidal spatial grating that produces a one-dimensional material response. The decay of this "transient grating" carries information about the relaxation and transport in the material and can be detected by a probe that is diffracted off of the grating. TGS can be used to study the transport and relaxation of a range of energy carriers including electrons, phonons and spins, and the transport length scale being studied can be tuned by varying the period of the transient grating. TGS has been employed to study unique physics problems including the measurement of quasi-particle diffusion in high-temperature superconductors [57], spin-Coulomb drag in GaAs quantum wells [58], quasi-ballistic phonon transport in silicon membranes [59], second-sound in graphite [14], and charging dynamics in lithium batteries [56].

The development of lasers employing shorter and shorter pulses, including into the attosecond regime [20], allows optical spectroscopies unparalleled temporal resolution.

Their control over spatial resolution is more limited. TGS allows some control over the length scale being probed via tuning of the spatial period of the transient grating. Transient absorption microscopy (TAM) has been developed to visualize photocarrier transport [60, 61]. However, all optical techniques are limited by the optical diffraction limit, necessitating the development of the pulsed electron probe.

2.2 Pulsed Electron Probe Techniques

2.2.1 Ultrafast Electron Diffraction

In continuous electron diffraction, a beam of probing electrons is accelerated onto some specimen where they are then elastically scattered by the positive ions [62, 63]. In crystalline materials, the lattice functions as a diffraction grating and scatters the electrons, forming diffraction patterns. These patterns can be analyzed in order to extract information about the crystal structure of the sample. Similarly, gas phase electron diffraction (GED) can be used to determine the structure of free molecules [64, 65]. In order to observe transient changes to crystal or molecular structure, the ultrafast nature of optical spectroscopies needed to be coupled into conventional electron diffraction [66].

The initial development of pulsed electron beams originates from streak camera technology, with demonstrations of subpicosecond electron pulses dating to the 1970s [23, 67]. In short, the image converter tube in a streak camera is used to produce spatial and temporal recreations of input optical pulses, with the length of the produced electron pulses being limited by either the electron flux generated (and thus, the space charge effect) or the specific streak camera being used. Mourou and Williamson pioneered picosecond electron diffraction, using 100 ps electron pulses generated from a streak

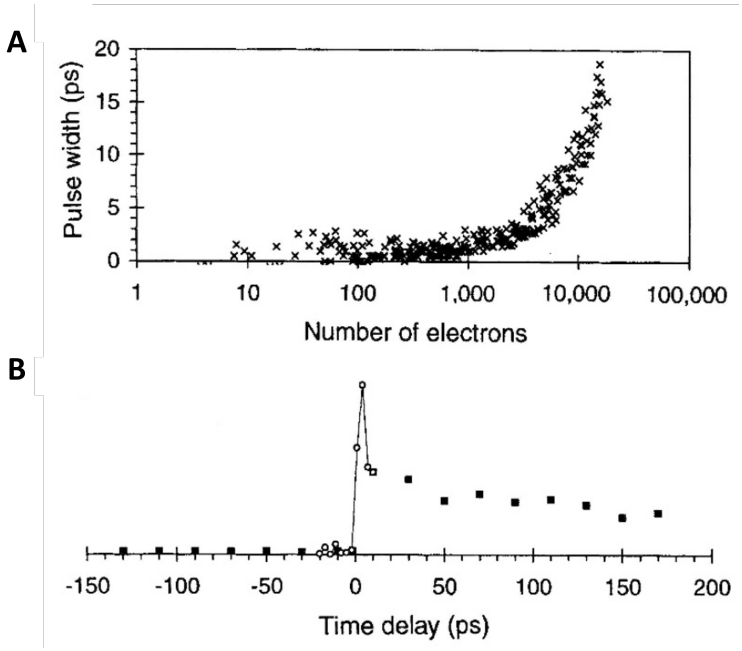

Figure 2.2: **Electron Pulse Characterization in UED** (a) The measured electron pulse width as a function of the number of electrons per pulse. Electron pulse widths were measured using a streak camera. (b) Diffracted intensity vs time delay. The transient change was induced by photo-induced ionization by the pump pulse, which deflects the probing electrons. Figure adapted from [72].

camera to generate electron diffraction patterns from thin aluminum samples [68]. They later were able to generate 20 ps pulses which they used to observe laser-induced melting of aluminum films [69]. Elsayed-Ali et al. later developed time resolved reflection high energy electron diffraction (RHEED) in which they were able to generate ∼100-200 ps electron pulses using a picosecond laser [70, 71].

The Zewail group at Caltech proposed the notion of performing electron diffraction with sub-picosecond electron pulses in 1991 [73, 74], with Williamson et al. reporting the development of their first UED system in 1992 [75]. The first generation UED consisted of a femtosecond laser, an electron column, a molecular beam assembly, and a CCD camera to record the generated diffraction patterns. They generated photon pulses as short as 60 fs using a colliding pulse mode-locked ring dye laser, which they used to

both excite the molecular beam to initialize a reaction and to generate electron pulses. In lieu of using a streak camera, they focused one arm of their femtosecond pulse train onto a gold photocathode. By limiting the fluence incident on the cathode in order to minimize space charge repulsion they were able to generate electron pulses as short as 1 ps, though they experienced broadening to >10 ps when using electron currents comparable to continuous gas phase electron diffraction experiments. However, this first iteration of UED simply recorded diffraction patterns using a pulsed electron beam and did not record the temporal evolution of the initiated reaction.

In 1997, Williamson, Cao et al. reported the first time resolved UED experiment with picosecond resolution [72]. To accomplish this, they developed a new system with an improved detection system capable of efficiently capturing diffracted electrons in order to allow the low electron fluxes necessary to maintain picosecond temporal resolution. They also developed the capability to measure the pulsewidth of their electron probe and made the first demonstration of the ability to clock a picosecond electron probe to dynamics initialized optically, as shown in Fig. 2.2.

Initial efforts in the development of UED were aimed towards probing molecular dynamics in the gas phase [72, 77, 78]. Later iterations of the Caltech UED systems, as well as systems produced by other groups, were designed for studying dynamics in solid media, then dubbed ultrafast electron crystallography (UEC) [24, 76, 79, 80]. To do this, the experimental scheme incorporated ultra high vacuum (UHV) chambers, shown above in Fig. 2.3, in order to facilitate clean sample preparation, characterization, and efficient collection of scattered electrons, enabling the reconstruction of atomic motion in response to excitation by analyzing the changes in intensity in the observed Bragg spots and Laue zones [66, 81]. Subsequently, UED has been used to study a diverse array of problems including structural dynamics of surfaces and interfaces [76, 82, 83], solid-liquid

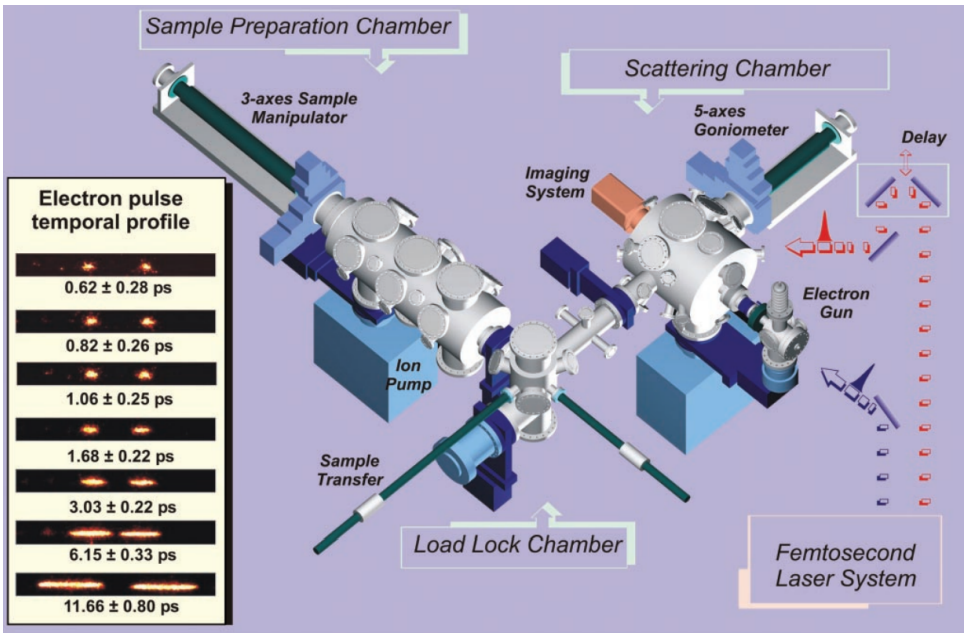

Figure 2.3: **Schematic of Typical UED System** Schematic showing a typical UED system including sample preparation and scattering chambers, pump and electron probe generation paths, and the imaging system. The inset shows electron probe pulsewidths as a function of electrons per pulse. Figure adapted from [76].

phase transitions [80, 84], probing non-equilibrium phases [85, 86], and electron-phonon coupling [87, 88].

While UED is now a mature technique, recent evolutions have continued to push its capabilities. The development of mega-electron-volt UED offers the ability to perform experiments with greatly improved temporal and reciprocal space resolution [89–93]. However, as a diffraction based experiment, UED is fundamentally unable to resolve real-space dynamics and perform sub-diffraction limit "imaging".

2.2.2 Ultrafast Electron Microscopy

Transmission electron microscopy possesses subnanometer spatial resolution, making it the ultimate imaging tool at ultrashort length scales. In 2005, Lobastov et al.

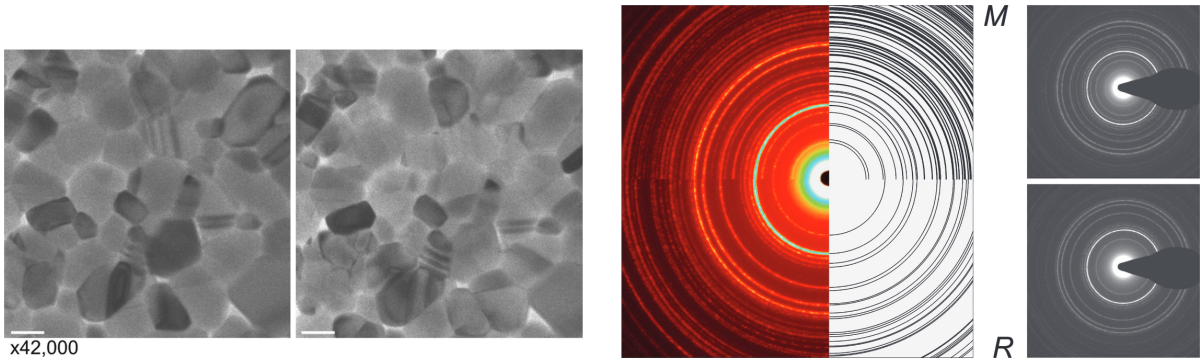

Figure 2.4: The images on the left shows UEM images taken before and after the laser induced phase transition. The right shows UEM diffraction patterns obtained before and after the phase transition. M and R denote the diffraction patterns of the monoclinic and rutile phases respectively. Figure adapted from [25].

reported the development of UEM at Caltech [94]. This first iteration of UEM consisted of a Ti:sapphire oscillator interfaced with an FEI Tecnai T12 120 kV TEM with a LaB_6 source. The output of the laser was split, with one arm exciting the sample under study and the other used to generate electron pulses. The Ti:sapphire was used in lieu of higher pulse energy systems in order to suppress space-charge effects present in early UED experiments as well as nanosecond TEM techniques [95] by weakly illuminating the TEM cathode so as to generate one electron per pulse on average. The initial proof-of-concept images did not show any dynamics, rather, images of stained rat cells that were taken using the pulsed source showed comparable quality to those taken with conventional TEM. This was the first reported use of a femtosecond pulsed laser to conduct pump-probe experiments in an electron microscope.

In 2006, Grinolds et al. performed direct time-resolved imaging and diffraction analysis of a phase transition in VO_2 using UEM [25]. VO_2 undergoes a first-order phase transition at $\sim$67°C from a monoclinic phase to a rutile phase. They drove the phase transition by pumping their sample with 776 nm pulses. They were able to obtain time resolved images and diffraction patterns before and after the phase transition, as shown

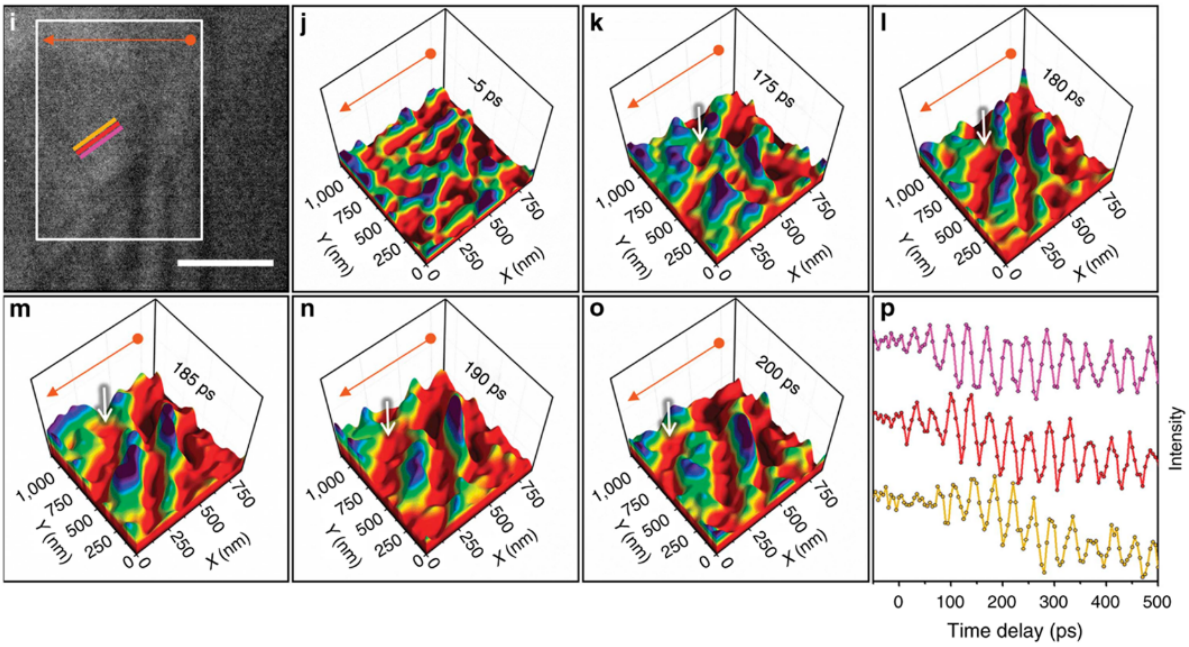

Figure 2.5: The top left image shows a bright-field UEM image of a WSe_2 flake. The next series of images shows surface plots along a single direction that highlight the propagation of a phonon wavefront. The final image shows the average image intensity from the colored regions in the bright field image over time. The phase velocities and periods correspond to a phonon mode in WSe_2. Figure adapted from [97].

in Fig. 2.4. By analyzing the change in the diffraction patterns with time, they were able to determine the timescale over which the structure rearranged on an atomic level.

A second iteration of UEM, reported by Park et al., was based on the coupling of an FEI Tecnai TF20 200 kV TEM with a Clark-MXR Yb-doped fiber oscillator/amplifier system [96]. The incorporation of the doped fiber based optical source enabled UEM to access much higher pulse energies and lower repetition rates, allowing UEM to probe a greater range of dynamics.

Since its initial demonstrations, UEM has been widely used to study material dynamics across its multiple modes of operation. Using real space imaging, UEM has been used to study photo-induced structural dynamics [98–100]. The optical pump pulse

produces an electronic response, which generates structural dynamics. The generated dynamics can then produce time-dependent contrast variations. Similar to conventional TEM, bright and dark field images can be obtained, and contrast can be enhanced by blocking electrons that scatter at high angles. Figure 2.5 shows the generation and propagation of acoustic phonons in WSe_2 [97]. Cremons et al. were able to observe the emergence of acoustic phonons near defects and interfaces, which they attributed to a strain nucleation mechanism initiated by the photoexcitation. Similar studies have been performed on MoS_2 flakes [101], in plasmonic systems [102], and on Fe-pnictide compounds [103].

Ultrafast electron diffraction studies have also been performed extensively on the UEM platform [100, 104–106], often in concert with real-space imaging [99, 107–110]. Similar to the aforementioned study on VO_2, van der Veen et al, used the combined detection modes in UEM to study a photoinduced phase transition in Fe(pyrazine)$Pt(CN)_4$ nanoparticles [107]. They were able to observe the structural phase transition one particle at a time using their real space images, which they corroborated by tracking the evolution of the diffraction peak positions.

UEM, like UED, enjoys continual development and technological improvement. The incorporation of an electron-energy spectrometer allows UEM systems to study time-resolved inelastic scattering processes and has lead to the development of photo-induced near-field electron microscopy (PINEM), which has been used to study electron-plasmon interactions [111–113]. Flannigan et al. have described the necessary improvements necessary to achieve sub-nm spatial resolution in UEM [114]. The development of attosecond electron beams is also a very active field of research [115–119].

2.3 Scanning Ultrafast Electron Microscopy

2.3.1 Operating Principles

Construction of an SUEM is similar to the general scheme of UEM or UED. The setup requires the coupling of a conventional SEM with an ultrafast laser. The UCSB setup is comprised of a Quanta FEG 650 from Thermofisher Scientific (formerly FEI) and an IMPULSE doped-fiber laser from Clark MXR, while setups constructed elsewhere such as Sandia National Lab [120] and Delft [121–123] utilize different hardware. Typically, the output of the laser is frequency doubled and quadrupled using non-linear optical processes, with one arm being used as the pump beam by focusing it onto a sample in the SEM chamber while the other is directed towards the electron source and used to generate electron pulses. The time delay between the optical pump and the electron probe is controlled by sending the pump beam through variable delay line. The pulsed primary electrons (PEs) are accelerated into the sample chamber and raster scanned across the sample. Secondary electrons (SEs) are generated as a result of the impact between the PEs and the sample and are collected by a detector. The resulting signal is processed and formed into images. By varying the delay time between the optical pump and the electron probe, snapshots of the excited carrier distribution can be obtained at different times after excitation. Figure 2.6 shows a schematic of a typical SUEM setup.

Because it is based on an SEM platform, SUEM can be used to characterize the same variety of samples as SEM, including both bulk and microscopic samples. The ability to characterize bulk samples represents a major advantage over UEM due to the simpler sample preparation and better dissipation of heat deposited by the optical pump. In concert with the lower PE energy, it also allows for the study of surface sensitive dynamics due to the small escape depth of SEs, another advantage over UED and UEM.

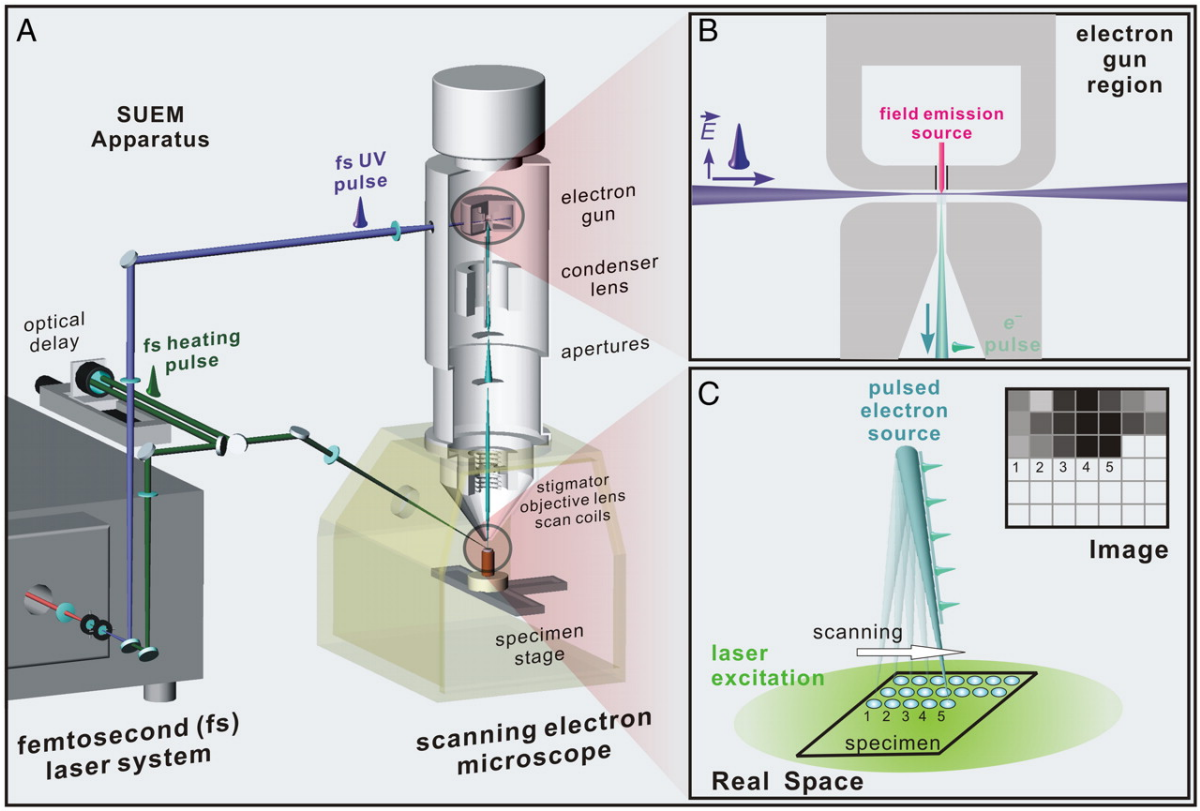

Figure 2.6: **SUEM Schematic** (a) A schematic of the SUEM setup combining a femtosecond ultrafast laser with a scanning electron microscope (SEM). (b) Side view of UV optical beam and pulsed electron beam in the SEM column (c) Schematic of SEM sample chamber showing pump excitation, pulsed electron beam scanning and image construction. Figure adapted from [124].

While the photoemission configuration is the most common SUEM construction, it is possible to pulse the beam using an electron beam blanker rather than via photoemission. Garming et al. have described an SUEM consisting of an FEI Quanta 200 FEG and a Coherent Ti:Saph laser [121–123]. They generate 100 ps pulses using a system that deflects the electron beam over blanking aperture placed in the electron column. This technique has the advantage of increased brightness and stability at the cost of a degradation in temporal resolution.

2.3.2 Contrast Mechanisms

There are several electron matter interactions that occur within the interaction volume generated by the impact of the electron beam with the sample, as shown in Fig. 2.9. The size of this interaction volume depends on the PE energy, as well as the properties of the sample, and can extend from a few hundred nm to a few μm [125]. The primary imaging modality of SUEM generates images through the collection of SEs. SEs are generated through inelastic collisions between the high energy PEs and weakly bound electrons within the sample. If the electrons generated by the PEs have a sufficiently high energy when they reach the sample surface they are emitted into the vacuum of the SEM chamber as SEs. The absorption of the pump laser pulse modulates the emission of SEs, producing the image contrast present in SUEM.

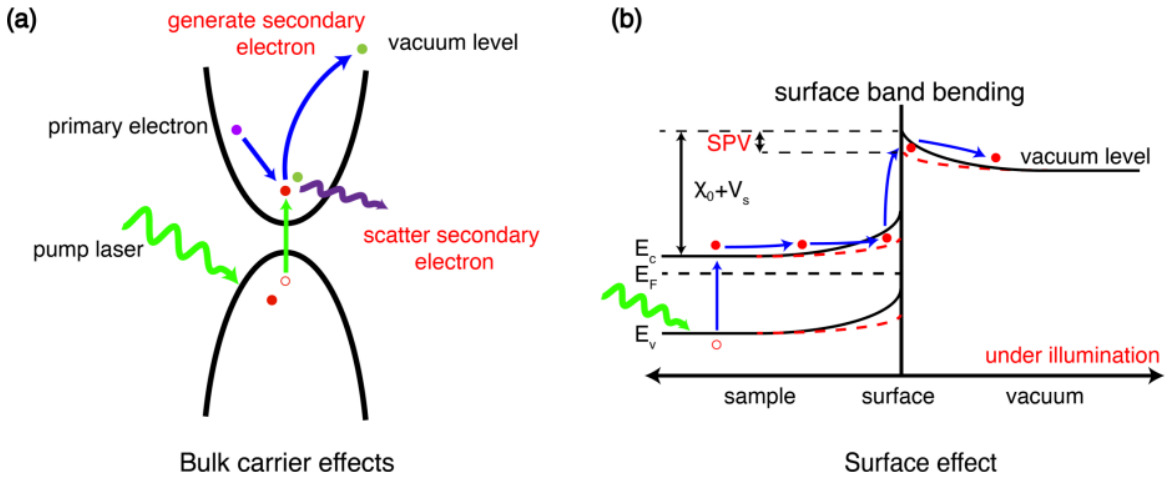

Figure 2.7: This schematic shows proposed SUEM contrast mechanisms. The left shows bulk effects that can modulate SE emission. The presence of photocarriers can both increase the rate of SE generation (due to their higher energy) and scatter SEs during their transport. The right shows a schematic of the surface photovoltage effect in n-type Si. The black (red) bands correspond to the energy band diagram without (with) photoexcitation. χ_0 is the electron affinity, and V_s is the surface band bending induced by pinning of the Fermi level. Photocarriers can compensate for surface band bending and reduce the effective barrier for SEs to reach the vacuum level. Figure adapted from [126].

The proposed mechanisms for producing this contrast can broadly be broken down into two categories, bulk effects and surface effects, as shown in Fig. 2.7. Photoexcitation generates excited electron-hole pairs in the bulk. These photoexcited carriers possess a higher energy, and thus, have a higher probability of being emitted as SEs when scattered by a PE. This should produce bright contrast in SUEM images. This has been the widely used interpretation in many of the initial SUEM studies [27, 28, 127, 128]. Additionally, these bulk carriers can scatter with SEs as they transport to the surface. This functions as an energy loss mechanism and can produce a decrease in SE emission, and dark SUEM contrast [129].

Figure 2.7b illustrates the surface photovoltage effect in n-type Si. On semiconductor surfaces, defects and dangling bonds pin the surface Fermi level and generate surface trap states within the band gap [130]. These states trap majority charge carriers at the surface, which results in a net charge redistribution within a small space-charge region. Thus, a thin electric field is produced in this region while the bulk remains neutral. This field can either increase or decrease the transport of SEs into the vacuum depending on the direction of the band bending. In fact, this phenomena produces the different image intensities present in n- and p-type semiconductors [131], as can be seen in Fig. 2.11 for Si. In the n-type case illustrated in Fig. 2.7, the bands bend upward near the surface, creating a barrier for SE escape. Photoexcitation compensates for the surface band bending, essentially bending the bands downwards, and thus reduce the barrier for SE emission, resulting in a net gain in SE contrast.

Li et al. used a standard SEM and a pulsed laser source to detect the SPV effect [132]. In this method, the pulsed optical laser transiently induces an SPV which is then monitored by a continuous electron beam. They measured the change in the SE emission as a function of optical fluence, primary electron beam energy, and the intensity

modulation frequency of the optical probe. They were able to observe an increase in SE emission in illuminated n-type Si and a decrease in p-type Si, corresponding to upward and downward band bending induced by the SPV.

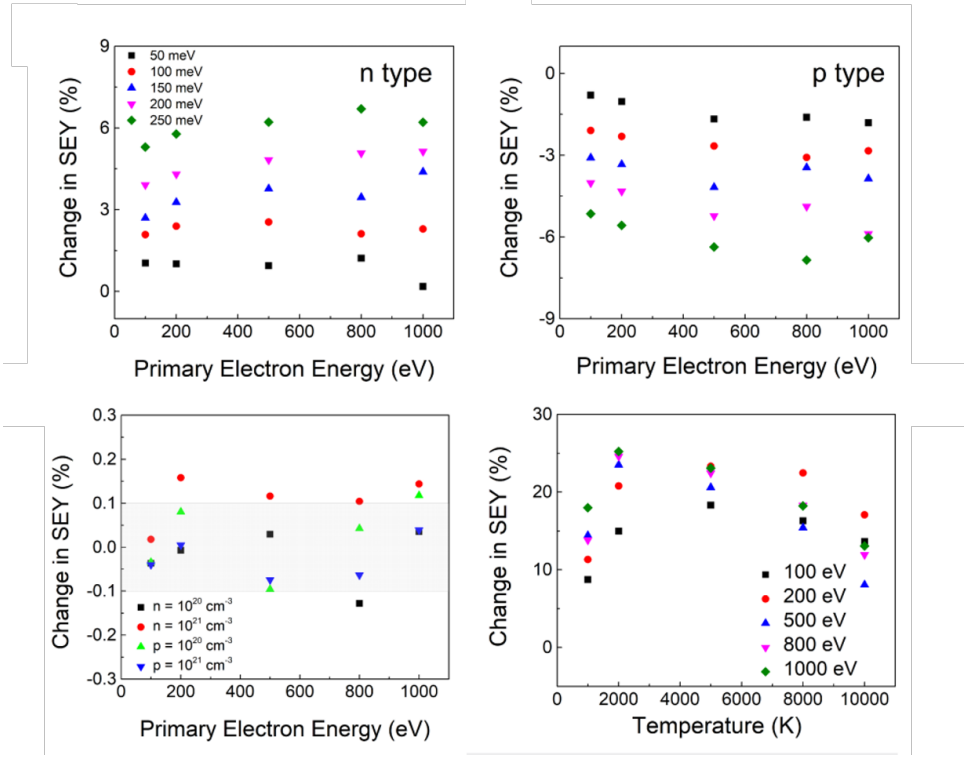

Figure 2.8: This figure shows the calculated change in SE yield due to various mechanisms. The top two figures show the change in SE yield due to the SPV effect in n- and p- type Si. The bottom left shows the change in yield due to bulk effects, which is seen to be negligible. The bottom right shows the change in SE yield due to the presence of hot carriers. Figure adapted from [126].

Ellis et al. used SUEM to study the dynamics of excited carriers at an Si interface buried below a 1 μm thick thermal oxide layer [120]. Pinning of the Fermi level in their p-Si/SiO_2 samples resulted in the interfacial charge and downward band bending into the p-Si layer. The pump light is absorbed by the buried p-Si layer, while the SEs are emitted primarily from the SiO_2 layer, as the oxide is significantly thicker than the expected SE escape depth. They propose that the contrast observed in their images results from the transport of electron-hole pairs to the p-Si/SiO_2 interface where they are captured by

trap states and reduce the interfacial charge, thus modulating the electric field in the SiO_2 and changing the observed SE emission.

While the works of Li et al. and Ellis et al. aided in developing understanding on the effect of photoexcitation on the SPV effect, the previously described bulk effects have not been quantified. Ouyang et al. used Monte Carlo simulations and time-dependent density functional theory calculations to study the impact of photoexcitation on SE emission [126]. Using Si as a model system, they studied both bulk effects as well as surface effects. They found that the SPV effect effect had a considerable effect on the SE yield, while the effect of bulk carriers was negligible. However, they also found that the presence of hot carriers, electrons with a high effective temperature, could have a significant impact on the collected SEs. While this study provided important insights into SUEM contrast mechanisms, it was limited to low PE energies due to the poor computational scaling at higher PE energies resulting from the increase in generated SEs that need to be tracked.

2.3.3 Other Electron-Matter Interactions

While SUEM is primarily concerned with changes in SE contrast, in principle, other electron-matter interactions that are detected by an SEM can also be time resolved. Electron backscatter diffraction (EBSD) is a well established technique used to characterize the microstructural and crystallographic properties of crystalline and polycrystalline samples [133]. In EBSD, primary electrons are accelerated into a sample where they are both elastically and inelastically scattered. The elastically scattered electrons may travel through the sample in a fashion that satisfies the Bragg condition, $2dsin\theta = n\lambda$, for any set of atomic planes, where d is the spacing between planes, θ is the Bragg angle, λ is the

electron wavelength, and n is the order of diffraction. The diffracted electrons are imaged by a phosphor where they form patterns composed of bands, known as Kikuchi bands, which correspond to atomic planes in the sample [134]. These diffraction patterns, which include the Kikuchi bands and a diffuse background formed from inelastically scattered electrons, contain information about the crystal structure and crystallographic orientation of the region of the sample from which they originate.

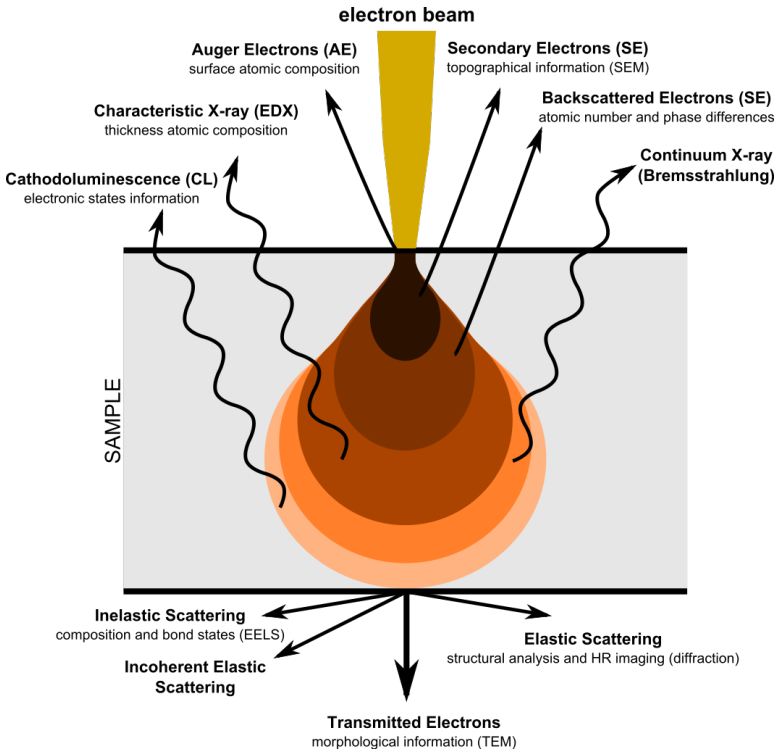

Figure 2.9: This schematic shows the various electron-matter interactions that occur when the primary electron beam interacts with the sample, as well as the overall interaction volume produced. While the interaction volume can be large, SEs are generally emitted from the top few nm of the sample surface. This figure is used from: Claudionico∼commonswiki (https://commons.wikimedia.org/wiki/File:Electron_Interaction_with_Matter.svg), https://creativecommons.org/licenses/by-sa/4.0/legalcode

Mohammed et al. have produced the only reported time-resolved EBSD diffraction patterns, shown in Fig. 2.10. Using a fluence of 0.4 mJ/cm^2, they observed vertical shifts in some of the Kikuchi bands, which they attributed to a change in lattice spacing from

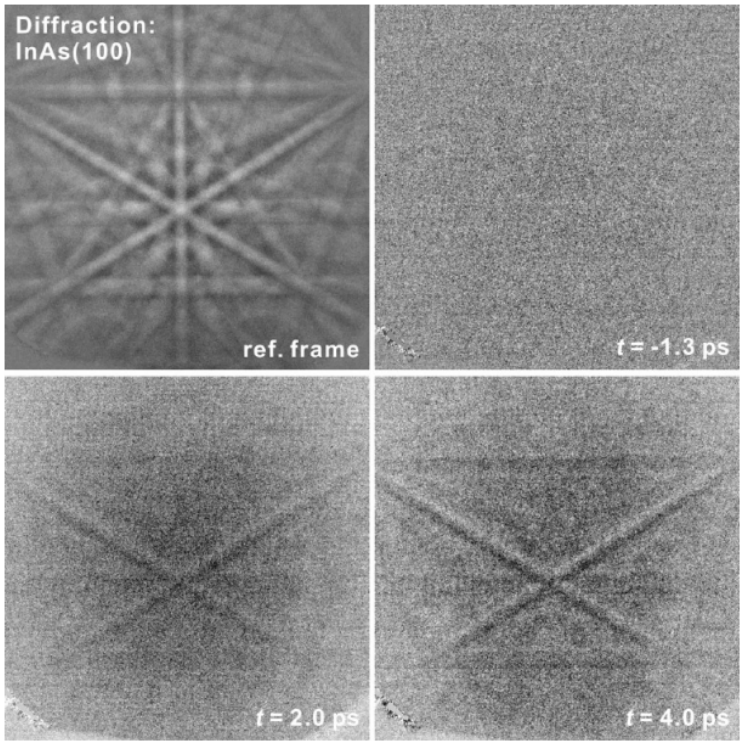

Figure 2.10: This figure shows time-resolved EBSD patterns taken from InAs. The top left is the reference diffraction pattern. The top right shows a difference pattern at negative time, showing no change before the pump pulse arrives. The bottom two patterns show changes in contrast in some of the Kikuchi bands. The figure is adapted from [135].

thermal expansion.

Cathodoluminescence is the process by which impinging electrons on a material produce the emission of photons, and is essentially the inverse process of the photoelectric effect. In SEM, the high energy PEs lose energy through inelastic scattering, which leads to the aforementioned generation of secondary electrons. Secondary electrons that have not reached the vacuum level can excite valence electrons in the material to the conduction band. The subsequent recombination produces a photon. The emitted photons can be collected in the SEM chamber and the produced spectra can be analyzed.

Sola-Garcia et al. have reported the development of a pump-probe cathodolu-

minescence spectroscopy setup based off an SUEM design [136–138]. They used their pump-probe CL spectroscopy to study nitrogen-vacancy (NV) center conversion dynamics. In pump-probe CL, the electron pulse functions as a pump, while the photon beam was used to optically probe the NV center [138].

While the focus of this thesis, and the SUEM field in general, is on photo-induced changes in SE emission, integrating other time-resolved signals produced by the electron-matter interactions in the SEM would make SUEM a powerful multi-platform characterization tool.

2.3.4 History

SUEM was first developed by the Zewail group at Caltech in the early 2000s. The first report on SUEM was published in 2010 [124] and described its initial development, including characterization of the electron pulses obtained from the zirconium-oxide-coated tungsten [ZrO_x/W(100)] cathode under various illumination conditions. Yang et al. also show an EBSD diffraction pattern using the pulsed electron beam and some static SEM images taken with the pulsed electron beam. The first time-resolved images and diffraction patterns were presented by Mohammed et al. in 2011 [135]. They reported SE difference images on crystalline silicon and CdSe(0001) and time-resolved EBSD patterns of InAs(100). They also report some initial findings on the relationship between the SE signal rise time and the number of electrons in the probing pulse, showing that the rise time increases as the number of electrons in the probing pulse increases due to space-charge repulsion.

The first use of SUEM to investigate carrier dynamics in a semiconducting system was reported by Cho et al. in 2014 [129]. They used SUEM to image the doping and

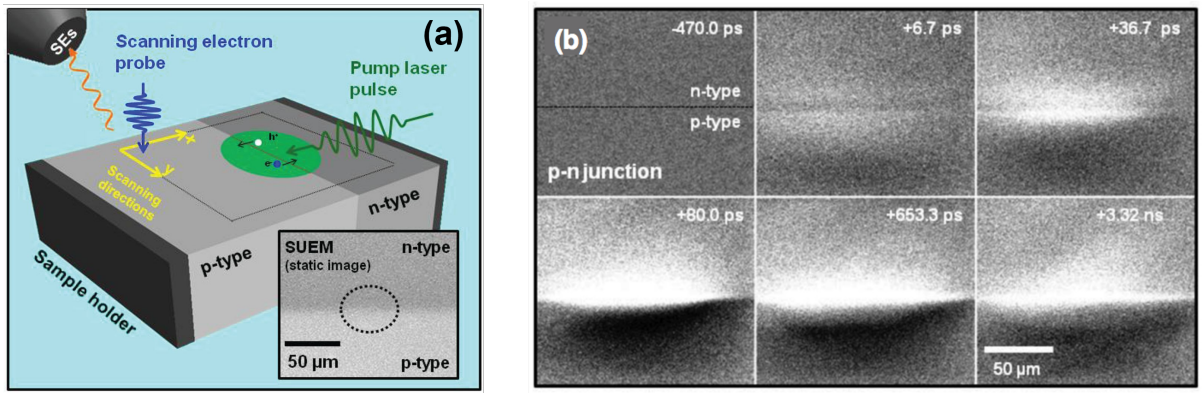

Figure 2.11: **SUEM Images at Si p-n Junction** (a) Schematic of Si p-n junction measurement, with pump pulse aimed at the junction. (b) Several snapshots from SUEM images at a p-n junction. No contrast is visible at -470 ps. Shortly after excitation, the contrast is uniformly bright. After 10s of ps, the potential of the junction separates carriers, and after a few ns they begin to relax to equilibrium. Figure adapted from [27].

carrier concentration-dependent dynamics in gallium arsenide (GaAs) substrates. They cleaved their samples in situ in order to probe the GaAs(110) plane which does not possess any dangling bonds and therefore presents a bulk-like band structure without surface band-bending effects [139]. They measured undoped, n-type, and p-type GaAs samples at various dopant concentrations and observed significant differences in the carrier dynamics as a result of both the doping type and level. They also observed negative time contrast in all of their GaAs samples, which has been replicated at UCSB, as shown in Appendix A. They attribute this to an electron energy loss mechanism wherein the initial electron pulse creates internal SEs which lose their energy due to carrier-carrier and carrier-phonon scattering. The subsequent optical pulse then suppresses overall SE contrast by exposing the internal SEs to additional scattering events.

In 2015, Najafi et al. used SUEM to image the transport of photoexcited carriers across a Si p-n junction [27], marking the first instance SUEM was used to study interfacial transport. They used p-n junction diodes consisting of phosphorus-doped n-

type Si (1.4×10^{14} cm^{-3}) grown on boron-doped n-type Si (9.4×10^{18} cm^{-3}) resulting in an intrinsic junction potential of 0.79 V. Figure 2.11 shows selected contrast images taken from an experiment in which the pump pulse was trained directly onto the junction interface. Immediately after excitation, the contrast on both sides of the junction is uniformly bright, similar to what the authors report for the individual layers. Within 37 ps, the junction begins to sort the excited carriers and bright and dark contrast is visible in the n- and p-type regions respectively. After 80 ps, transport across the junction has peaked and the overall contrast, and therefore, number of carriers is at a maximum. Over the next few nanoseconds, the junction equilibrates and the overall contrast level decreases. The SUEM images show carrier separation for 10s of microns away from the junction, in contrast to expected behavior from the drift-diffusion model where carrier drift is expected to occur within the depletion layer [140]. The authors attribute this to ballistic-type motion from the hot carriers excited by the pump pulse, causing them to be transported far from the junction.

A later SUEM study on pristine n- and p-type Si analyzed the the spatiotemporal evolution of excited electron and hole populations and found evidence of multiple distinct transport regimes [127]. By analyzing the second moment $\langle R^2 \rangle$ of the spatial distributions of the excited carriers, given by:

$$\langle R^2 \rangle(t) = \frac{\sum_{i,j}(x_i^2 + y_j^2) I(x_i, y_j, t)}{\sum_{i,j} I(x_i, y_j, t)} \tag{2.1}$$

where $I(x_i, y_j, t)$ is the intensity at a particular pixel located at (x_i, y_j) at time t, the authors were able to identify a super-diffuse transport regime for times less than 200 ps, where the carriers were observed to have a transient diffusivity $D \propto \partial \langle R^2 \rangle / \partial t$ almost three orders of magnitude greater than the room temperature diffusivity. After

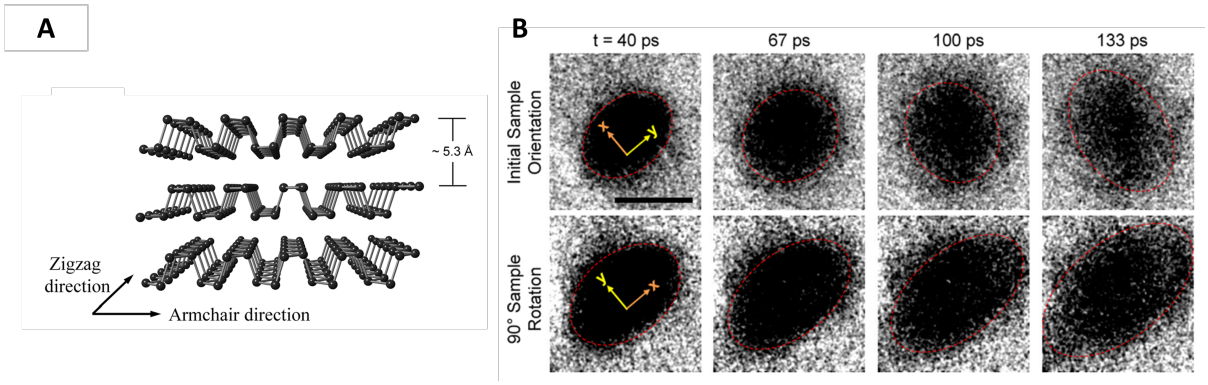

Figure 2.12: **SUEM Images of Black Phosphorus** (a) Black phosphorus crystal structure, showing layered structure and armchair and zigzag directions. (b) SUEM images from black phosphorus flake. The orange and yellow arrows in the two rows denote the armchair (x-) and zigzag (y-) directions. The sample was rotated 90°between the two measurements, highlighting the preferential diffusion of hot carriers along the armchair (x-) direction. Figure adapted from [28, 141].

~500 ps, the excited carriers were found to have relaxed and exhibited a more expected steady-state diffusivity $D_0 \approx 30$ cm^2/s. The authors consider the excited carriers as a hot non-degenerate electron gas and ascribe the super-diffuse transport regime to the large pressure gradient in the carrier population that is generated by the laser pulse. They modeled their results by using a diffusion equation with an initial Gaussian carrier distribution and by assuming a decaying diffusivity to account for the cooling of the hot carriers, and reported good agreement with their experiments.

In 2017, Liao et al. used SUEM to image anisotropic photocarrier dynamics in black phosphorus [28]. Black phosphorus is a layered 2D material with a tunable band gap ranging from 0.3 eV in bulk samples to 1.3 eV in single layers [142–144]. It also possesses a puckered orthorhombic crystal structure [145], shown in Fig. 2.12A, resulting in highly anisotropic near-equilibrium charge carrier mobility along its zigzag and armchair directions. The authors used SUEM to image and confirm the presence of highly anisotropic in-plane carrier transport. Using a similar scheme to [127], they analyze their images, shown in Fig. 2.12B, by calculating the angle-dependent variance

σ, given as:

$$\sigma(\theta,t) = \frac{\int\int \rho(r,t)(r\cdot\hat{\theta})^2 d^2r}{\int\int \rho(r,t)d^2r} - \left(\frac{\int\int \rho(r,t)(r\cdot\hat{\theta})d^2r}{\int\int \rho(r,t)d^2r}\right)^2 \tag{2.2}$$

where $\hat{\theta}$ is a unit vector corresponding to some angle θ and $\rho(r,t)$ is the local excited carrier concentration, which can be approximated by the pixel intensity $I(r,t)$ of the SUEM images. By analyzing the rate of change of the variance of the carrier distribution, Liao et al. determined that the ratio of the diffusivities along the armchair and zigzag directions was approximately 15. This is much higher than values measured by steady-state experiments [146] or predicted by first-principles calculations [147], and demonstrates both the difference between near-equilibrium and hot-carrier dynamics and the ability of SUEM to observe the latter.

SUEM has also been used to image dynamics in polymers and amorphous materials. Najafi et al. used SUEM to image surface acoustic wave (SAW) generation and propagation in poly(3-hexylthiophene) (P3HT) thin films [148]. They were able to measure the propagation velocity of the generated SAWs and used it to calculate the Young's modulus of their sample. Liao et al. used SUEM to image the hot carrier dynamics in hydrogenated amorphous silicon (a-Si:H) [128]. They observed an initial fast diffusion, attributed to high temperature hot carriers, followed by charge trapping of electrons and holes due to band-tail and deep defect states which arise due to the materials amorphous nature. The authors also observe a spatial separation of electrons and holes, evidenced by the bright ring and dark center region in the SUEM images, show in Fig. 2.13. They conclude that this feature is a direct visualization of "relaxation semiconductor" behavior, where charge separation had been previously predicted [149]. In a relaxation semiconductor, the large dielectric relaxation time, given by $\tau_d = (\epsilon\epsilon_0)/\sigma$ (where ϵ is the relative permittivity, ϵ_0 is the permittivity of free space, and σ is the electrical conductivity)

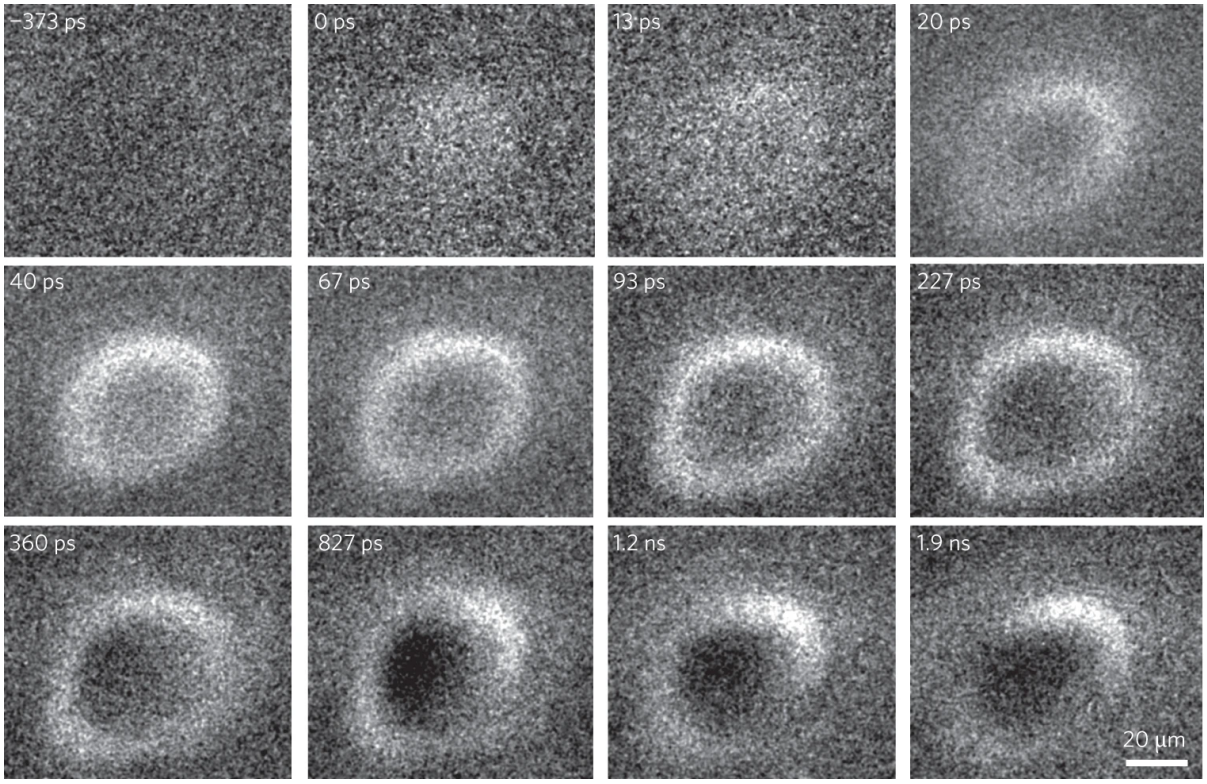

Figure 2.13: **SUEM Images of Amorphous Silicon** SUEM images taken on a-Si:H samples. The initial contrast is bright, with a bright ring and dark center beginning to form after 20 ps. The bright ring then expands rapidly for 100 ps before its size stabilizes. The center region then becomes darker until its intensity peaks at 870 ps. The contrast then begins to fade over the next few ns. Figure adapted from [128].

suggests that the electric field generated by the separated carriers is weak and cannot be quickly neutralized via conduction. This observation showcased SUEM's ability to characterize a varied set of materials and its utility in verifying physical theories.

In addition to the seminal works produced by the pioneering Caltech SUEM setup, additional contributions have been made by the SUEM developed at KAUST. Sun et al. characterized their setup and reported temporal and spatial resolutions of 650 fs and 5 nm respectively [150]. They also measured dynamics on CdSe single crystals and powder films and observed different dynamics for the two samples, which they attributed to different surface morphologies. They also observed negative time contrast on CdSe, similar to

that reported by Cho et al. on GaAs [129], which they ascribed to an "electron-photon dynamical probing" regime in which the pump photons suppress SE emission. Shaheen et al. later reported a thickness dependence of the SUEM signal in CdSe films [151]. Khan et al. used SUEM to measure differences in carrier dynamics in InGaN nanowires before and after surface passivation with octadylthiol (ODT), concluding from their SUEM images that surface carrier recombination was reduced after ODT treatment [152]. Later, Bose, Adhikari et al. measure Si doped InGaN nanowires and conclude that Si doping introduces leads to a slower electron release rate which results in a slow increase in SUEM image contrast, but a faster signal decay at later times [153]. Similarly, Bose, Ashok et al. employed SUEM to map surface trap states in copper indium gallium selenide nanocrystals ($Cu_{0.96}In_{0.56}Ga_{0.48}Se_2$ or CIGSe) before and after surface passivation by ZnS bombardment, observing that the ZnS bombardment reduces the density of surface trap states [154]. Meizyte et al. then found that electron trapping channels on CIGSe-ZnS films are further reduced by the deposition of a thin NaF layer [155].

El-Zohry et al. used SUEM to measure carrier diffusion on CdTe single crystals [156]. They measured diffusion coefficients of ~40,000 and ~14,460 cm^2/s from the (110) and (111) surfaces, around 10^4 times larger than the accepted bulk value. In contrast, they observed no significant diffusion on the (211) faces. They attributed the high carrier diffusion observed on the (110) and (111) surfaces to weak electron-phonon coupling, the absence of surface trapping states, and the presence of a local surface potential. They attributed the difference in diffusion between the (110) and (111) surfaces to the higher electron density in (111), which increased the rates of electron-electron scattering and thus reduced the measured diffusivity. In contrast, they claim that the polar (211) surface formed surface oxide layers that produced surface-trap states which inhibited diffusion.

Similarly, Nughays et al. used SUEM to measure carrier diffusion lengths in

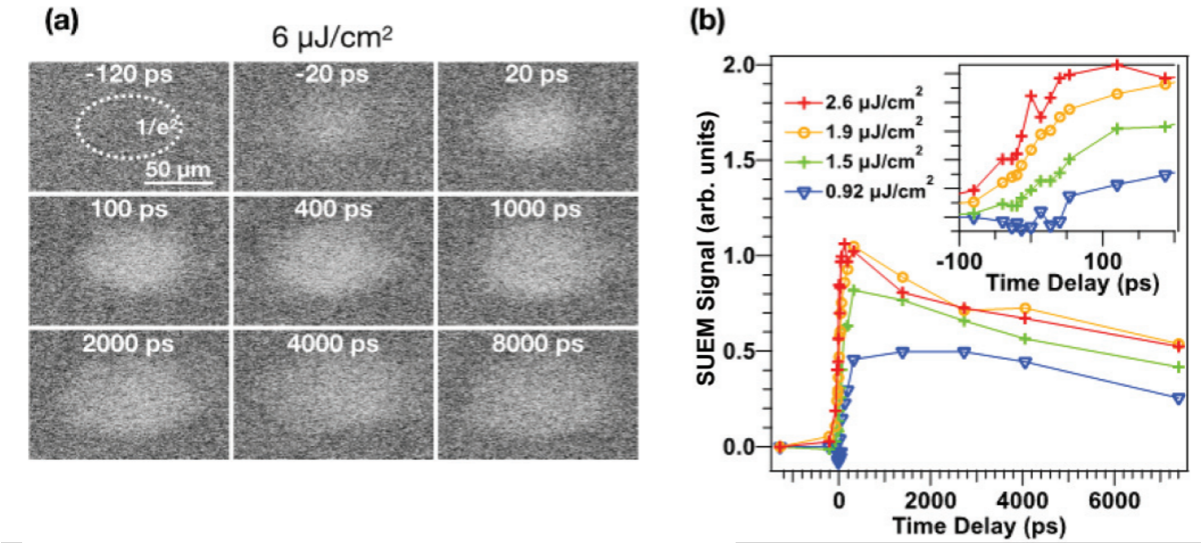

Figure 2.14: The right image shows SUEM images from the buried p-Si/SiO_2 interface. The rapid expansion of contrast is attributed to vertical diffusion from the buried interface to the vacuum level, rather than lateral diffusion of carriers. The right shows the SUEM signal for various fluences. At sufficiently high fluence, the peak signal level saturates. Figure adapted from [120].

different crystal orientations of the perovskite methylammonium lead iodide (MAPI) [157]. They measured a surface charge carrier diffusion length of 20 μm for the (001) orientation, but did not observe any diffusion when probing (100). They attributed this observation to a difference in surface trap state density.

As mentioned previously, Ellis et al. have reported on the development of SUEM at Sandia National Laboratory [120]. Their SUEM consists of a Philips/FEI XL30s SEM coupled to a 532 nm Fianium HYLASE fiber laser (2 MHz, 10 ps). They perform shot to shot modulation of their pump beam at 1 MHz using an EOM and utilize a lock-in amplifier to construct their images. They detect SEs using a custom built microchannel plate (MCP) detector, which offers superior rejection of pump light compared to standard Everhart-Thornley detectors (ETD). They perform SUEM experiments on a buried p-Si/SiO_2 interface, and observe a saturation in material response with increasing fluence,

as shown in Fig. 2.14. They attribute this to charge trapping at the buried interface, and model their results by assuming that the interface functions as a saturable sink for the diffusing electrons. They also observe a rapid initial expansion of contrast within 10s of ps, similar to the work described in [127], but they ascribe this to vertical carrier diffusion near the presence of the saturable sink.

Garming et al. described the development of SUEM that also incorporates lock-in detection [121]. Their setup utilizes a 95 MHz Coherent Vitara-T Ti:Saph oscillator with a FEI Quanta 200 FEG SEM. However, unlike the other mentioned instances of SUEM, they utilize a beam blanker to modulate their electron beam rather than coupling with the femtosecond laser source. While this improves the stability and brightness of the pulsed electron beam, it limits temporal resolution to ∼100 ps. Using their lock-in SUEM, they characterized the impact of different surface termination of GaAs (111) surfaces on surface carrier dynamics. They also performed some novel modifications of their microscope by installing an optical microscope below their sample stage, allowing them to produce optical pumps with sub-micron spot size, but limiting them to the study of thin samples [122]. They used their sub-micron pump to study relaxation dynamics in MoS_2 flakes. They later used their SUEM to pump an atomic force microscope cantilever tip and were able to image its oscillations [123].

Chapter 3

Development of SUEM at UCSB

3.1 Basic Configuration

Construction of an SUEM is similar to the general scheme of UEM or UED. The setup requires the coupling of an electron source, in this case an SEM, with an ultrafast laser. The UCSB setup is very similar to the original Caltech configuration [124,129,135], and is comprised of a Quanta 650 from Thermofisher Scientific and an IMPULSE laser from Clark MXR, as shown in Fig. 3.1. The IMPULSE is a Yb-doped fiber oscillator/amplifier system that outputs 250 fs pulses with a center wavelength of 1030 nm. It provides pulses with energies up to 10 μJ and with a tunable repetition rate between 200 kHz and 25 MHz. The output of the laser is frequency doubled and quadrupled using β-BaB_2O_4 (BBO) crystals to 515 nm and 257 nm respectively. Typically, the 257 nm beam is directed towards the electron source and used to generate electron pulses while the 515 nm beam is used as the pump beam by focusing it onto a sample in the SEM chamber, though in principle the fundamental beam or any of the other harmonics can

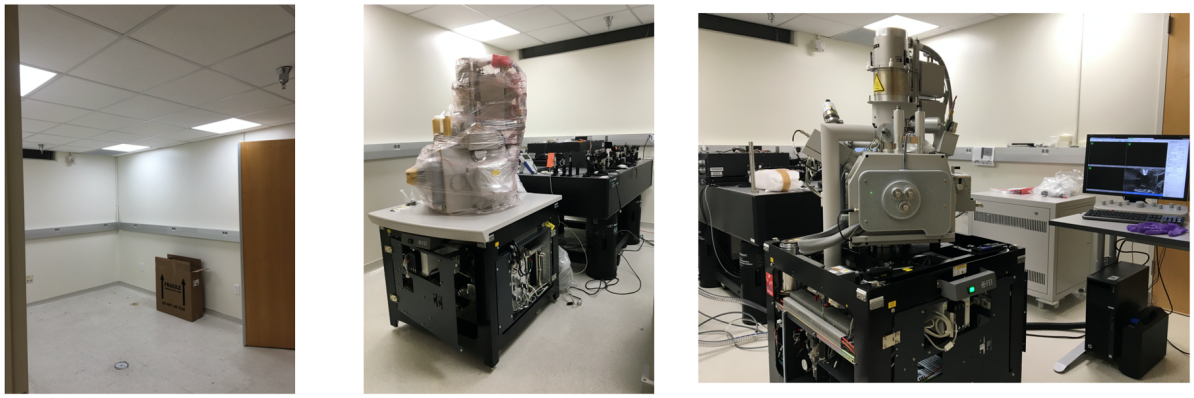

Figure 3.1: **Timelapse of SUEM construction at UCSB** The constituent components, including the Quanta 650 and IMPULSE laser, were purchased and assembled over the course of two years.

be used as the pump. The final focusing lens for the pump is placed in a kinematic mount inside of the SEM chamber in order to focus the beam as tightly as possible. The time delay between the optical pump and the electron probe is controlled by sending the pump beam through a 600 mm long variable delay line, allowing for a range of time delays up to 4 nanoseconds. The pulsed primary electrons (PEs) are accelerated into the sample chamber and raster scanned across the sample. Secondary electrons (SEs) are generated as a result of the impact between the PEs and the sample and are collected by a detector. The resulting signal is processed and formed into images. By varying the delay time between the optical pump and the electron probe, snapshots of the excited carrier distribution can be obtained at different times after excitation.

3.2 Optical Configuration

The UCSB SUEM system consists of three tiers of optics, as seen in Fig. 3.2. The first tier, constructed on a normal optical table, consists of the femtosecond laser and most of the optics responsible for conditioning the pump and probe beams. Periscopes

on the table send the pump and probe beams to the second and third tiers, respectively. The second tier, located on a large optical breadboard mounted to the optical table, directs the pump beam into the SEM chamber and a motorized mirror mount controls its alignment onto the SEM sample stage. The third tier is used to focus the probe beam onto the SEM photocathode.

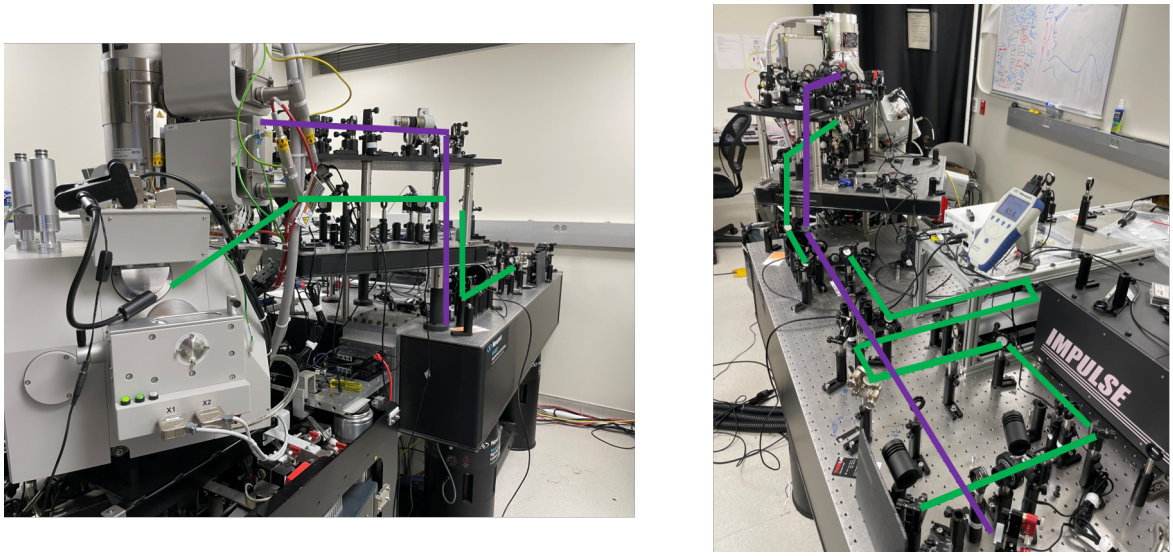

Figure 3.2: **The beam path across multiple tiers of optics.** The femtosecond laser is placed on the optical table, where harmonic generation and beam conditioning is performed. The second tier is used to send the beam into the SEM and align it onto the sample. The third tier is used to focus the probe onto the cathode in order to generate electron pulses. The approximate paths of the pump and probe are traced in green and purple respectively.

A schematic for the beam path on the first tier is shown in Fig. 3.3. The femtosecond laser source used in this SUEM setup emits 250 fs pulses with a center wavelength of 1030 nm. The maximum power output is 20 W and the repetition rate is tunable between 200 kHz and 25 MHz. A repetition rate of 5 MHz is typically used, as at lower rates the delay between pulses makes measurements prohibitively lengthy, and at higher rates the pulse energy becomes too low. The fundamental beam is focused using a 200 mm lens, with the focused beam waist being located between two pieces of BBO crystal. The

BBOs are placed in 3-axis mounts in order to allow for proper critical phase-matching for Type 1 second harmonic generation (SHG). The BBO #1 is used to generate the second harmonic at 515 nm (2.4 eV), while BBO #2 is used to generate the fourth harmonic at 257 nm (4.8 eV). The focal point is placed between the two BBOs in order to simplify the optical path. More efficient harmonic generation could be achieved by focusing the fundamental beam onto BBO #1 in order to generate the second harmonic, separating the second harmonic, and then refocusing it onto BBO #2 in order to generate the fourth harmonic. Previous iterations of the SUEM utilized the third harmonic (343 nm, 3.6 eV). For type 1 third harmonic generation (THG), a time delay compensator was placed after the BBO used for SHG in order to improve temporal overlap of pulses in the THG crystal, and a dual waveplate was used to rotate the orthogonal polarizations produced during SHG into parallel polarizations.

After harmonic generation, harmonic separating mirrors are used to isolate the second and fourth harmonics from the fundamental. The fourth harmonic is loosely focused using a 100 cm lens, and then sent up a periscope to the third tier of optics where it is used as the photoelectron generation beam. The second harmonic is used as the pump, and is collimated using a 60 cm lens and then sent through an acousto-optic modulator (AOM) which is used to modulate its intensity with a frequency in the range of 10s of kHz. The pump is then sent through an optical delay line and a 1:3 beam expander before being sent to a periscope and up to the second tier.

Figure 3.4 shows schematics of the optical path on the second and third tiers. After the periscope, a series of mirrors direct the beam into the SEM chamber. Because of the angle of the viewport into the SEM chamber, the final two mirrors are tilted on a third axis so that the height of the beam waist above the table can be adjusted high enough to ensure normal incidence on the optical window and focusing lens. The

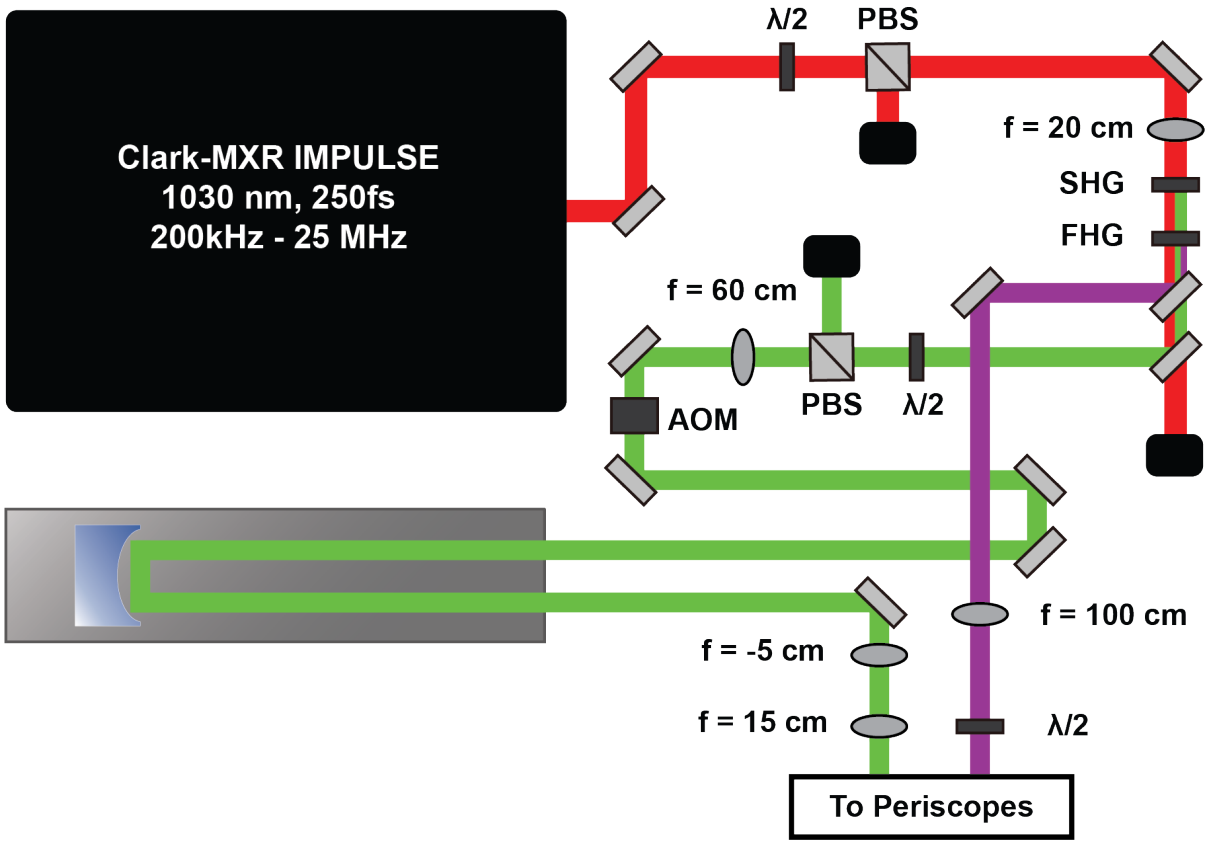

Figure 3.3: **A schematic of the beam path on bottom optical table** The bottom optical table is used to generate and condition the pump and probe beams. This configuration is used when the 515 nm beam is used as the pump. PBS - polarizing beam splitter, AOM - acousto-optic modulator, $\lambda/2$ - half waveplate

final mirror is a dichroic mirror on a motorized mount. This motorized mount is used to control the placement of the beam on the sample. A camera is placed behind the dichroic mirror and is used to image the sample to aid with the process of pump beam alignment.

After being sent to the third tier, the probe beam is sent through a 1:2 expander. It is then sent back and forth down the bread board in order to ensure that the pump and probe paths are of rough equal length, ensuring that the overlap between the pump and probe beams overlap within the delay stage range. After a second 1:2 expander, the beam is then focused into the SEM column using a 20 cm lens that is placed on a motorized x-y-z translation stage. The final mirror in the path is also a dichroic, and a

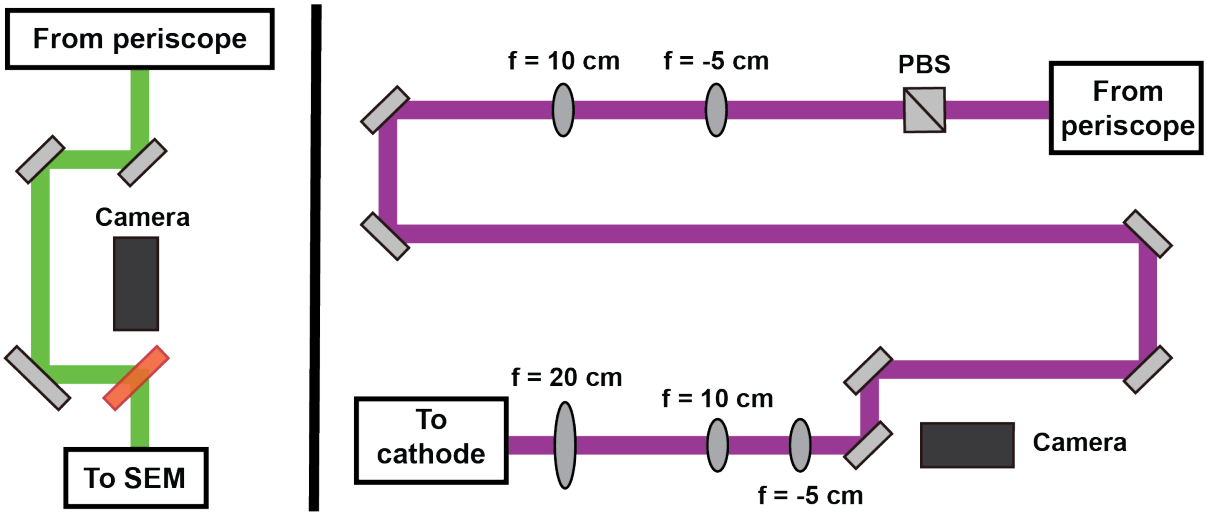

Figure 3.4: **A schematic of the beam path on the upper tiers.** The left shows a simplified schematic of the beam path on the middle tier of optics. A camera behind the final dichroic mirror is used to image the beam on the sample. The final optic is on a motorized stage in order to control the beam on the sample. The right shows the beam path on the top tier. The probe beam is expanded twice before being sent into the SEM column.

camera is placed behind it in order to image the photocathode.

It should be noted that the schematics shown here use the 515 nm beam as the pump. Alternative beam paths have been constructed to allow for pumping with 1030 nm and 257 nm, but are not shown here.

3.3 Achieving Photoemission

The central technical challenge in achieving a functional SUEM is obtaining a pulsed electron beam. While LaB_6 emitters are occasionally used in SEM, most systems utilize tungsten cathodes. The Quanta 650 utilized in this setup uses a Schottky field effect emitter made out of zirconium-oxide-coated tungsten (ZrO_x/W), shown in Fig. 3.5. The ZrO_x coating reduces the work function of W from 4.5 eV to ~2.8 eV at high

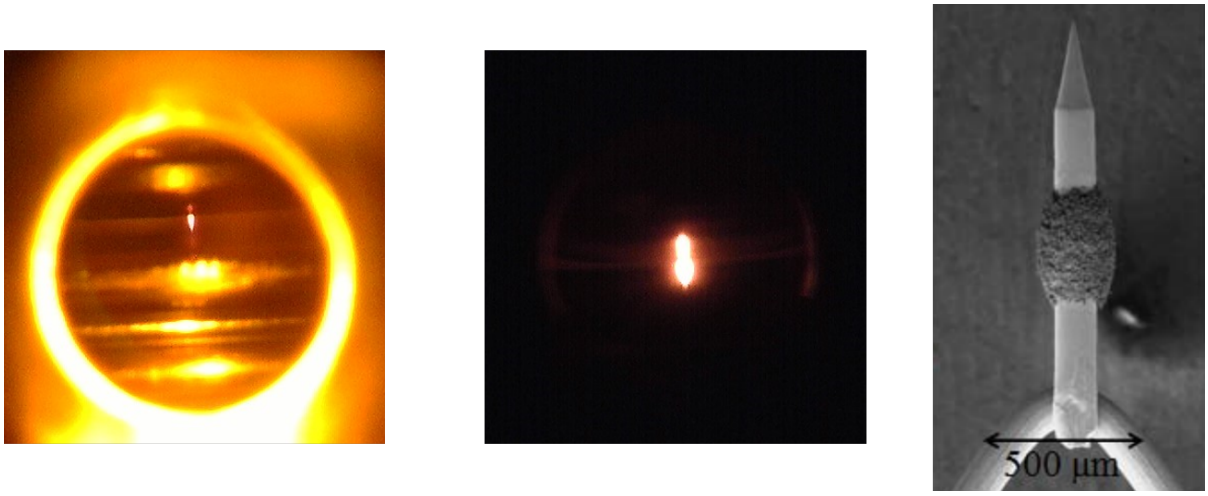

Figure 3.5: **Pictures of ZrO_x/W cathode in SEM.** The left shows the ZrO_x/W cathode through the viewport in the column while under a 2.1 A heating current. The center shows the cathode with a standard 2.4 A heating current. A heating current of 1.4 A is typically used in photoelectron mode. The right shows an image of a typical ZrO_x/W cathode, taken from [162]. The bulb in the center of the shaft is the ZrO_x.

temperatures [158–160]. A strong electrostatic field (extraction voltage or V_{ext}) is also applied to the tip, which further reduces the work function via the Schottky effect. The change in the work function is given by [161]:

$$\Delta\phi = \sqrt{\frac{e^3 F}{4\pi\epsilon_0}} \tag{3.1}$$

where $\Delta\phi$ is the change in the work function, e is the elementary charge, F is the applied electric field strength, and ϵ_0 is the vacuum permittivity. Applying a field on the order of $\sim 10^7$ V/cm lowers the work function by another $\sim$1.2 eV, allowing electrons to tunnel through the barrier when the cathode is heated to 1800 K (corresponding to a filament current of $\sim$2.4 A) [124, 159, 160].

In order to generate the pulsed electron beam, the filament heating current and extraction voltage are reduced to suppress thermionic emission from the source. It should be noted that given that the work function of W is smaller than the photon energy of the

probe beam, the set points for the heating current and V_{ext} are somewhat arbitrary. Some testing in out group has shown that varying V_{ext} has a negligible impact on photoemission performance. A viewport in the SEM column that is normally used to measure the temperature of the cathode is used for optical access. Images of the cathode under different heating currents are shown in Fig. 3.5.

The final focusing lens used in this setup is placed on a Newport x-y-z translation stage driven by piezo nanopositioners. A UV fused silica (UVFS) lens with a designed focal length of 20 cm is used. This is an approximate value, as due to the sharp change of UVFS's index of refraction in the UV spectrum, the effective focal length of this lens can be quite different depending on the wavelength used. The lens maker's equation for a thin plano-convex lens in air is given by:

$$\frac{1}{f} = \frac{n-1}{R} \tag{3.2}$$

where f is the focal length, n is the index of refraction, and R is the radius of curvature of the lens. For UVFS at 257 nm, the effective focal length of the final lens is ∼18.5 cm. The diameter of the SEM column is approximately 14 cm, so the final lens and translation stage were place approximately 11.5 cm from the viewport window.

The initial alignment of the probe beam onto the tip is quite challenging, as there is no feedback on the accuracy of the alignment until the beam is incident on the tip, and therefore, it is difficult to determine how close or how far the beam is from the tip when it is not properly aligned. In order to send the beam to the general region of the tip, a camera is placed behind the final turning mirror in the probe path and used to image the tip. The probe beam is then aligned so that it is roughly colinear with the tip, as determined by the reflection of the beam off of the viewport window. Due to the

small acceptance angle of the window/tip system, this rough alignment is sufficient to place the focused beam in the general region of the cathode.

Given the size of the emitter shaft relative to the tip, shown in Fig. 3.5, it is far more likely that the the alignment process will at first strike the shaft rather than the tip. When the beam is incident on the shaft, weak thermal emission due to laser heating on the order of a few fA is produced. The best way to measure this is through a picoammeter, which measured the current dissipated through the SEM chamber walls. At steady state, this measured current will be equivalent to the total current entering the chamber through the column, minus the generated secondary electrons. In order to mitigate this, a Faraday cup [163] cup can be used to contain SEs and ensure that all PEs are dissipated through the grounded chamber. The image generated through the SEM UI can also be monitored for small changes in contrast.

Once the probe beam is directed into the column and in the general region of the cathode, the most straightforward method to find photoemission is simply to raster scan the beam through the column. After scanning across an appropriate region horizontally, if no increase in current is observed, the lens is translated upwards in order to move the beam waist in the column upwards, and then another horizontal scan is repeated. This procedure is repeated until an increase in emission is observed. The lens is translated upwards after each horizontal scan rather than downwards as if the beam is not incident on the tip after one scan, assuming the range of the scan is correct, then the tip must necessarily be located higher up in the column.

In cases where finding thermal emission is difficult, the filament heating current can be increased so as to produce some residual thermal emission. This can increase the change in current when the beam hits the tip from a few fA to a few pA. However, the

Time (min)	Current (pA)
0	14.5
2	13
5	10.5
10	7.1
15	5.4
20	3.7
25	2.75
30	1.85
35	1.3
40	0.85

Table 3.1: This table shows the decay of residual thermal emission when using a 1.4 A heating current, V_{ext} = 3800 V, and C1 = 1400V.

residual thermal emission will decay as the tip cools via radiation and its work function increases, producing a moving background that can make small changes hard to perceive. Table 3.1 shows the typical rate of decay of thermal emission. In this case the heating current is low while the value of V_{ext} is high, but in principle the behaviour should be similar in the inverse case.

Once suspected thermal emission is found, it is fairly straightforward to confirm if it is laser induced. Blocking the laser beam while capturing an image should result in a reduction in image contrast, as shown in Fig. 3.6, or in a reduction in the measured current. Once laser induced emission is confirmed, the beam should be centered onto the shaft by translating the lens horizontally until the measured current or observed image contrast is maximized. After that, the lens is translated downwards until it is incident on the tip. It is easy to identify when the beam is focused onto the tip, as the photoelectron current produced when the beam is on the tip is multiple orders of magnitude greater than the laser heating induced thermal emission. However, as the beam is translated downward, some horizontal course corrections may be necessary as the cathodes are not necessarily perfectly vertically oriented.

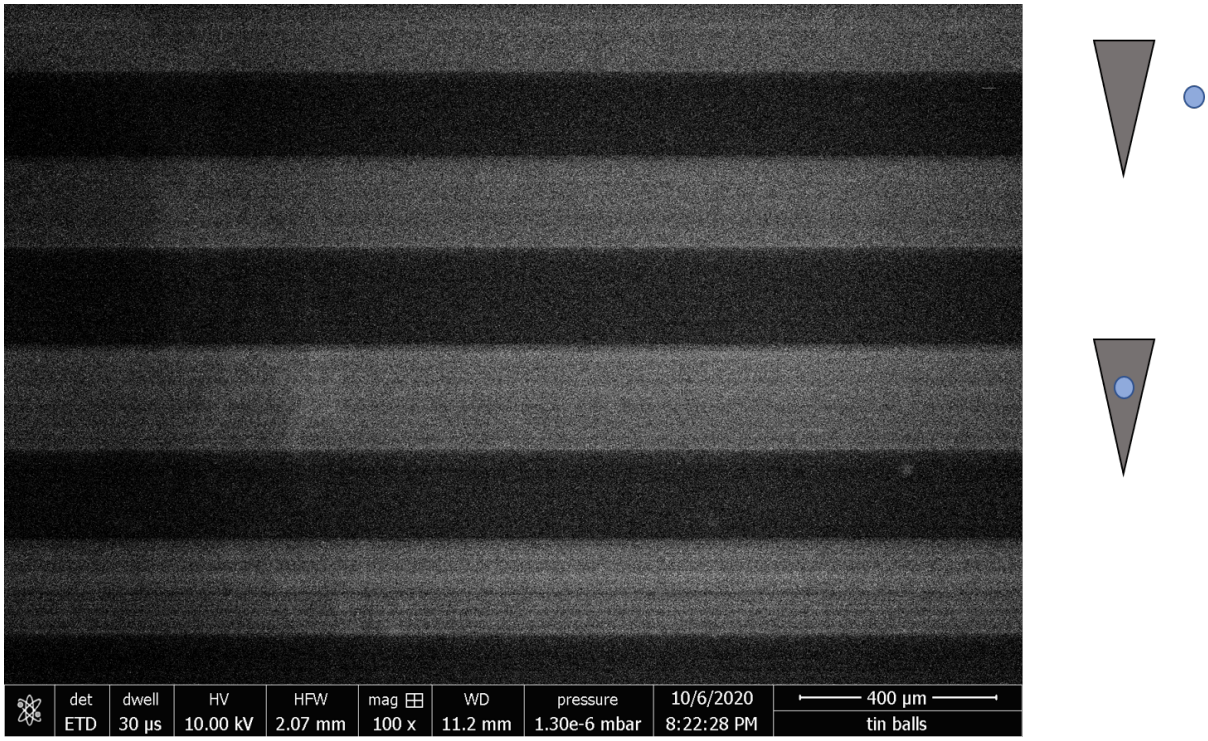

Figure 3.6: The presence of laser induced thermal emission can be easily verified by blocking and unblocking the probe beam while capturing an image. When the laser is blocked, the image contrast decreases significantly.

Also, it should be noted that the laser generated current does not increase monotonically as the beam is translated down the cathode. The current increases when it is incident on the ZrO_x bulb, but then decreases as the beam is translated further down. As it is translated even further down, the current begins to increase as the shaft tapers to a dip due to its decreased heat capacity. Once the beam approaches the tip, the emission becomes very strong. Figure 3.7 shows the measured photoemission current as a function of UV probe pulse energy taken using a rep rate of 5 MHz. Measurements performed by Yang et al. are included as a comparison [124]. Our results are in good agreement with the measurements reported by Yang et al., and no repetition rate dependence is observed, as expected. For the range of pulse energies shown, the number of electrons generated per pulse is linear with the pulse energy, indicating that the photoelectrons

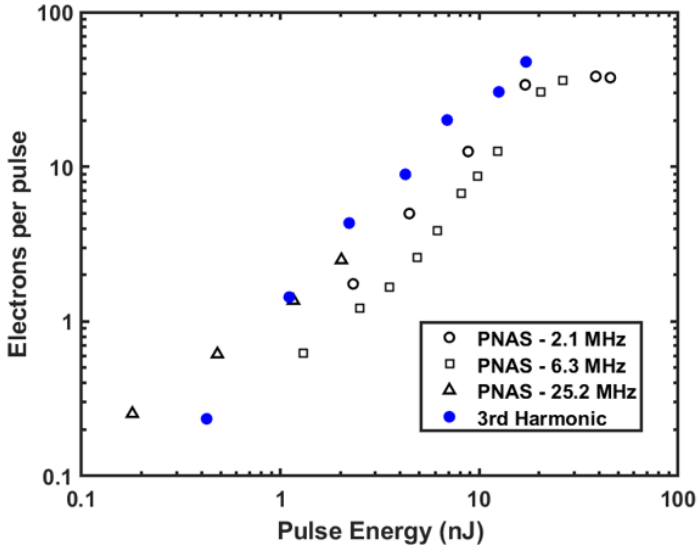

Figure 3.7: This figure shows the number of electrons per pulse generated when using the third harmonic beam as a function of the UV pulse energy. The results are compared with the current reported by Yang et al [124].

are generated by single-photon absorption.

It should be noted that it would be more appropriate to compare the number of electrons per pulse as a function of fluence rather than pulse energy, but the beam waist in the Yang et al. study is not known. However, it is still impossible to know how much of the UV probe beam is incident on the tip and how much passes through to the back of the column, making it difficult to very precisely compare photoemission across different configurations.

Figure 3.8 compares the number of photoelectrons per pulse generated as a function of fluence when using either the third of fourth harmonic as the generation beam. Figure A.1 in Appendix A shows a comparison with the data presented in [124]. At comparable fluences, the fourth harmonic generates more electrons per pulse. This increase in photoelectron generation efficiency at shorter wavelengths was also observed by Yang et al. [124]. At higher fluences (only achieved using the fourth harmonic), the linear

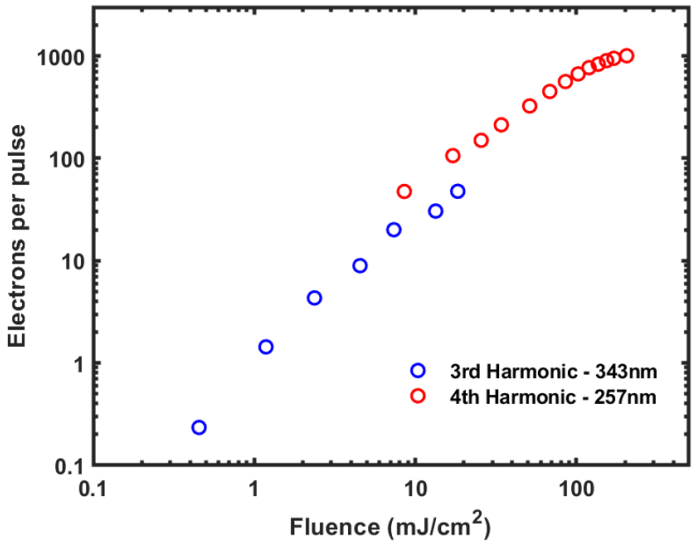

Figure 3.8: The number of electrons generated per pulse as a function of fluence is shown for both the third and fourth harmonic. The fourth harmonic generates more electrons per pulse at comparable fluences, perhaps due to the higher photon energy. At high fluences, the number of photoelectrons generated saturates.

trend breaks down as the number of electrons produced per pulse saturates, perhaps due to simultaneous two-photon absorption [164] or decreased collection efficiency into the column due to strong electron-electron interactions near the emitter [165].

3.3.1 Manipulating SEM Crossover

The pulsed electron beam is significantly dimmer than the conventional beam. The standard values for V_{ext} and the C1 lens voltage are set to ensure that a high quality electron beam is incident on the sample. If V_{ext} is adjusted in the process of aligning the photoelectron beam, the C1 voltage will require a commensurate adjustment in order to maintain beam quality. However, in order to maximize source brightness in pulsed mode, the C1 voltage required further adjustment in order to ensure that as many of the photogenerated electrons enter the SEM column as possible. The optimal value

V_{ext} (V)	C1 (V)	Current (pA)
4060	1415	460
3900	1388	150
3800	1370	70
3700	1353	32
3600	1332	14
3500	1292	1
3400	1275	
3300	1260	
3200	1243	
3100	1226	
3000	1210	

Table 3.2: The table shows the residual thermal emission at different values of V_{ext} and the optimal C1. Below a V_{ext} of 3500, very little residual thermal emission is observed, and the optimal C1 is found via optimizing the photoemission current. This was measured using an open strip aperture. The current standard operating procedure is to use a V_{ext} less than 3000 V.

for C1 will depend on both the value of V_{ext} used and the strip aperture size, with examples for a specific column configuration shown in Table 3.2. However, the total photocurrent measured has generally been observed to be consistent across different V_{ext} and C1 combinations.

In order to maximize the current into the column, the C1 voltage can be adjusted while monitoring the current and viewing the beam crossover. The crossover refers to an image of the minimum cross-section of the beam after being converged by the C1 lens in the SEM. In order to maximize the measured current, the C1 voltage should be adjusted until the beam crossover is as small and bright as possible. The SEM gun tilt and shift can then be adjusted as necessary. Images of the beam crossover are shown in Fig. 3.9 for two different values of C1. The image on the left results in a higher beam current on the sample.

Given the sensitivity of the measured current to the C1 lens voltage and alignment,

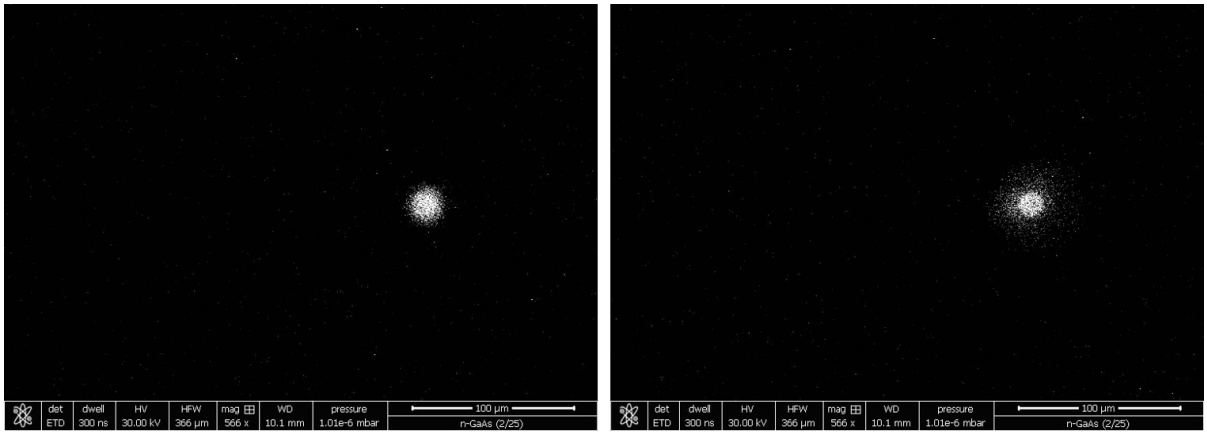

Figure 3.9: **Images of the photoelectron beam in SEM crossover.** The left shows an image of the electron beam in crossover when using V_{ext} = 2600 V and C1 = 1130 V. The image on the right was taken using the same settings but using C1 = 1110 V. The configuration on the right produces a higher photoelectron current. Both images were taken with an open strip aperture.

it is important to ensure that this alignment is adequately set before finding photoelectrons. It is possible to align the probe beam onto the tip but not observe the generated photoelectrons. In order to mitigate this, the V_{ext} should be set to its desired values, and the filament heating current should be reduced until only a faint image is seen. Then, the C1 voltage and gun tilt can be optimized to maximize the residual thermal emission. Then, the heating current can be reduced to its intended value and the photoemission alignment process can begin. Once an adequate C1 voltage has been identified for a given V_{ext}, this procedure can be used simply to ensure that the gun tilt and shift are properly aligned.

It should also be noted that the photoelectron beam has shown a tendency to drift over long measurements. Occasionally, the image of the beam in crossover will drift off axis, resulting in a drastic reduction in current. This simply requires a simple adjustment to the gun tilt, but could make future automation of image acquisition challenging. This phenomena has been observed to occur more frequently when initially using the pulsed

electron beam, and the alignment becomes more stable after a few corrections. Right now, this drift is attributed to the strong electric field produced at the tip by the probe generation beam, but the precise origin is not yet understood.

3.3.2 Effect of the Strip Aperture

SEMs contain a strip aperture within the electron column that is used to eliminate high-angle electrons from the beam. Using a smaller diameter strip aperture produces a more uniform electron beam and produces higher quality images, at the cost of current. The strip aperture performs a similar function when using a pulsed electron beam, though the interplay between the current and the image quality becomes more important given the inherent dimness of the photo-illuminated source.

Aperture Diameter (μm)	Current (pA)
1000	270
100	135
50	110
40	80
30	75
20	40

Table 3.3: This table shows the measured photoemission for different strip aperture diameters. The current was generated with 12 mW of probe power using the fourth harmonic. A value of V_{ext} = 2600 V was used for all measurements. The optimal C1 varied based on the strip aperture. For the 1 mm aperture, C1 = 1130 V was used. For small apertures, C1 = 1108 - 1112 V was used.

Table 3.3 shows the measured photocurrent for different strip aperture diameters. The photoelectrons were generated using 12 mW of probe power and a V_{ext} of 2600 V. The value of C1 was varied to maximize the measured current. When using the completely open strip aperture, the most current is recovered, and a C1 value of 1130 V

is necessary to maximize current. At smaller strip apertures, different values of C1 are necessary to maximize current.

3.4 Photoemission Characterization

While the SEM is designed for continuous, stable operation while using the standard 2.4 A filament heating current, the reduced heating current results in degraded performance over time. This is due in part to radiative cooling of the cathode which results in an increase in the effective work function. In addition to aiding in producing sustained thermionic emission in standard operation, the filament heating current also aids in maintaining the ZrO_x coating on the tip of the emitter. When the emitter is cooled, the ZrO_x coating recedes to the bulb on the shaft, further increasing the work function of the tip. Given that SUEM experiments can take several hours to complete, it is imperative to characterize the performance and stability of the photoelectron beam to allow for consistent image acquisition. Figure 3.10 shows a schematic of a lock-in detection scheme used to characterize photoemission. A mechanical chopper is used to modulate the intensity of the UV probe beam. This imparts the same modulation onto the photoelectron beam, which can be measured by monitoring the SE signal produced by the ETD.

Figure 3.11 shows the measured LIA signal corresponding to the photoelectron beam strength generate with the third harmonic beam for pulse energies ranging from 4-15 nJ, corresponding to fluences ranging from 8-30 mJ/cm^2. After finding photoemission, the SEM image acquisition system is left to scan repeatedly over an area for two hours while the signal decay is measured. Given that SE emission is material dependent, the same sample is used for each measurement. At low pulse energies, the measured

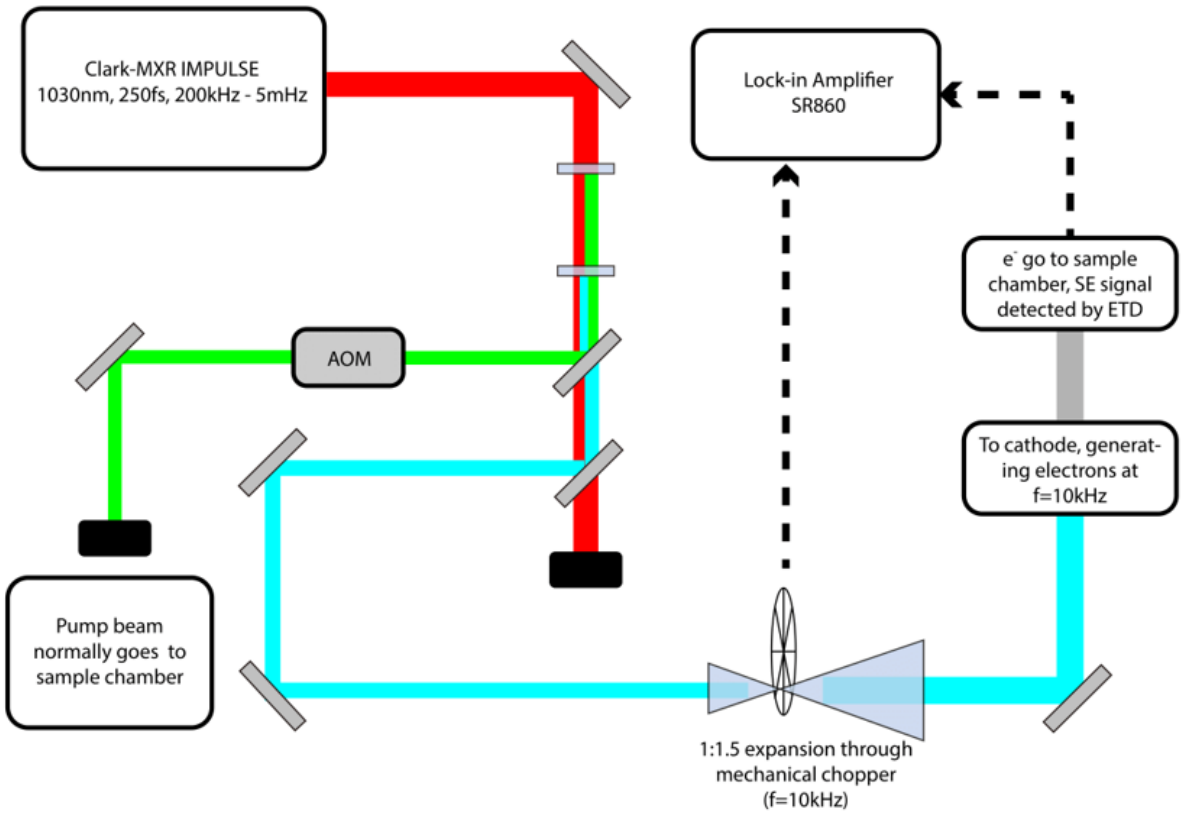

Figure 3.10: A schematic of the lock-in detection scheme used to characterize photoemission. The UV probe beam is modulated using a mechanical chopper. This imparts the same modulation frequency on the photoelectrons. The SE signal from the ETD contains information on the photoelectron signal and can then be sent to a LIA.

signal begins to decay immediately. This is due to the radiative cooling of the tip and the recession of the ZrO_x coating from the tip back to the bulb. Both phenomena serve to increase the work function of the tip, decreasing emission over time. At higher pulse energies, the initial measured signal saturates, as can be seen for the 10 and 15 nJ measurements. This indicates that the photoemission has exited the single photon generation regime. The signal remains stable at that level for several minutes before decaying. The decay begins earlier when using a 10 nJ pulse energy compared to 15 nJ. This may be because at high pulse energies, the number of photons per pulse is high

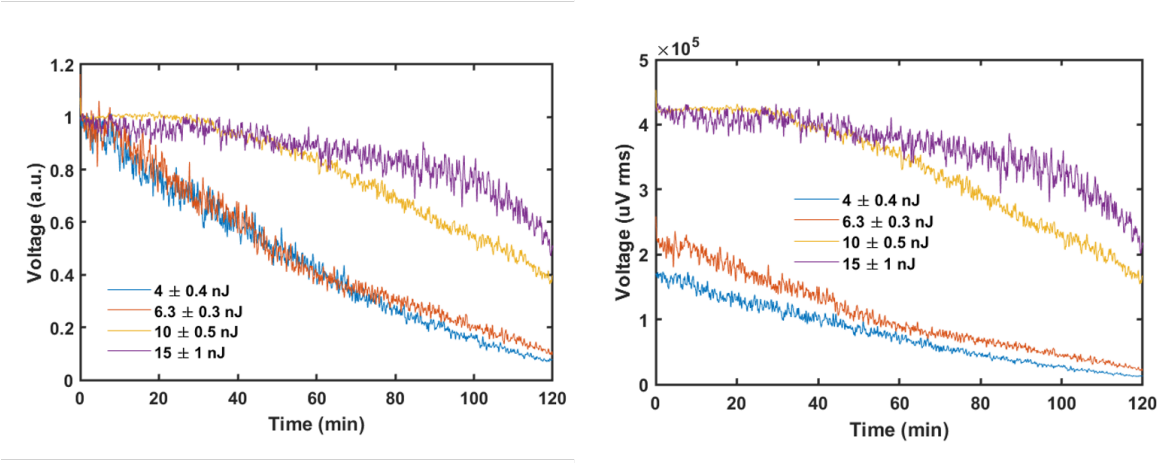

Figure 3.11: This figure shows the photoemission stability using the third harmonic beam for several different pulse energies. The left figure shows normalized signal values, while the right shows absolute values. At higher pulse energies, the maximum initial signal saturates.

enough to produce two-photon absorption rates that can sufficiently compensate for the decreasing work function.

Figure 3.12 shows the measured decay using the fourth harmonic. The powers shown correspond to fluences of 2 and 6 mJ/cm^2 respectively. These fluences are much lower than those used to perform this test with the fourth harmonic due to changes in the optical beam configuration. As a result, the fluences used for the stability tests are not high enough to enter the saturation regime. In both cases, the decay in photoemission begins immediately, and the normalized figure shows that the rate of decay is identical. Curiously, the signal noise is much lower when using the fourth harmonic rather than the third. This may be due to improved stability in the harmonic generation process, as the LIA settings used in all measurements was identical. Figure A.4 in Appendix A plots the measured decay observed using both the third and fourth harmonic beams.

Due to this observed decay in photoemission over several hours, it becomes necessary to pause SUEM measurements in order to regenerate the emitter tip and recover

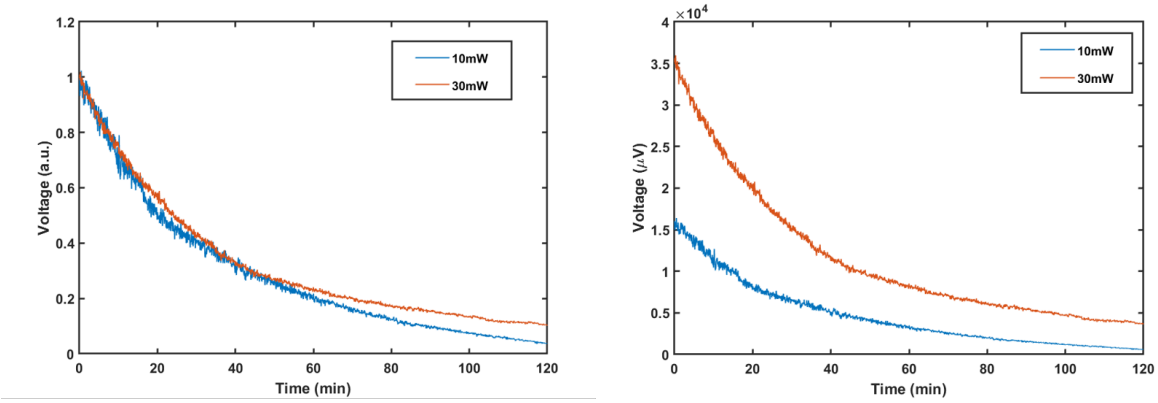

Figure 3.12: This figure shows the photoemission stability using the fourth harmonic beam for two different pulse energies. The left figure shows normalized signal values, while the right shows absolute values. The signal is more stable than the one generated using the third harmonic, likely due to the improved stability of fourth harmonic generation. It should be noted that at higher fluences, the fourth harmonic is also able to produce stable emission over long periods of time, but this has not been recorded.

optimal performance. The general procedure involves pausing the measurement and increasing the filament heating current back to its nominal value. Leaving the tip heated for 30-60 minutes reforms the ZrO_x tip, and allows subsequent measurements to achieve expected levels of photoemission. Another strategy to ensure stable emission involves performing measurements using a submaximal power. Then, the power can be increased to compensate for decreases in the observed photocurrent.

3.4.1 Polarization Dependence

Figure 3.13 shows the measure photoemission signal as a function of polarization as measured with the LIA detection setup previously described. An angle of 0 corresponds to a polarization parallel to the tip axis, while 90 degrees is perpendicular. The parallel polarization results in the highest measured probe current, while the perpendicular polarization produces very little current. This is consistent with previous

reports [124, 164, 166, 167]. Potential explanations for the polarization effect include an increase in absorption of photons by surface electrons [168] or a field enhancement effect near the emitter tip [169, 170] when the polarization is parallel to the emitter axis.

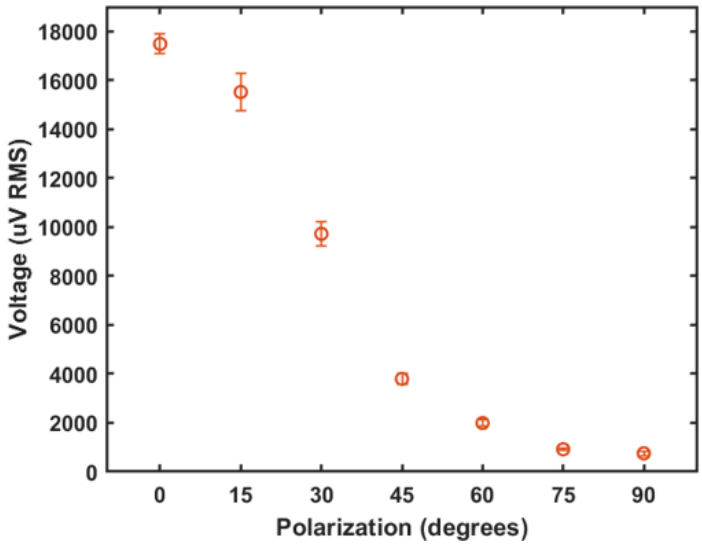

Figure 3.13: This figure shows the photoemission magnitude as a function of UV probe polarization. Maximum photoemission occurs when the polarization is oriented parallel to the tip, denoted as zero degrees.

3.5 Pump Beam Alignment

While not as challenging as the probe alignment, the pump alignment still requires some precision due to the geometry of the SEM chamber relative to the optical table. When samples are placed at the eucentric height 10 mm below the SEM pole piece (from which electrons are emitted) the maximum horizontal field of view is approximately 2 mm. Therefore, the initial alignment of the pump onto the sample must be precise within that tolerance. Figure 3.14 shows the scheme that was used to align the pump beam early in SUEM development. The image on the left shows an early iteration of the optics used. The final focusing lens was placed on a translation stage on a breadboard attached to the

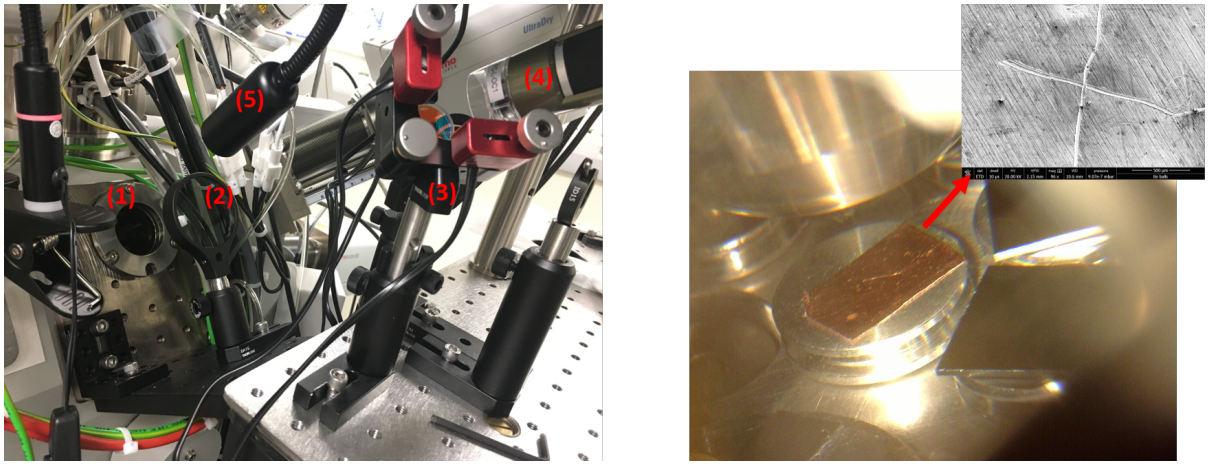

Figure 3.14: The picture on the left shows the optics used to align the pump beam onto the sample. 1) The optical access window into the SEM chamber, 2) the final focusing lens, 3) the motorized mirror mount controlling alignment, 4) CCD camera used to image the sample, 5) lamp used to illuminate the sample chamber. On the right is an optical and SEM image of a piece of copper tape with a cross inscribed into it.

angled SEM chamber wall. A dichroic mirror on a motorized mirror mount directed the pump through the focusing lens and optical access window into the chamber. A CCD camera behind the dichroic mirror was used to image the sample, while a lamp was used to provide illumination.

In order to roughly align the pump, a sample with a feature identifiable through the CCD camera was used. The identifiable feature was imaged using the SEM, thus defining the optimal position for the pump beam to be focused. The sample shown in Fig. 3.14 is a piece of copper tape with a cross inscribed into it. An identifiable corner of a piece of semiconductor substrate can also be used. The pump can then be aligned with the feature using the motorized mirror mount. This procedure is usually sufficient to place the beam within one to two mm of its desired point.

Once the beam is estimated to be in the SEM field of view, its precise location can be determined by exposing a sample to a high laser fluence. After observing the

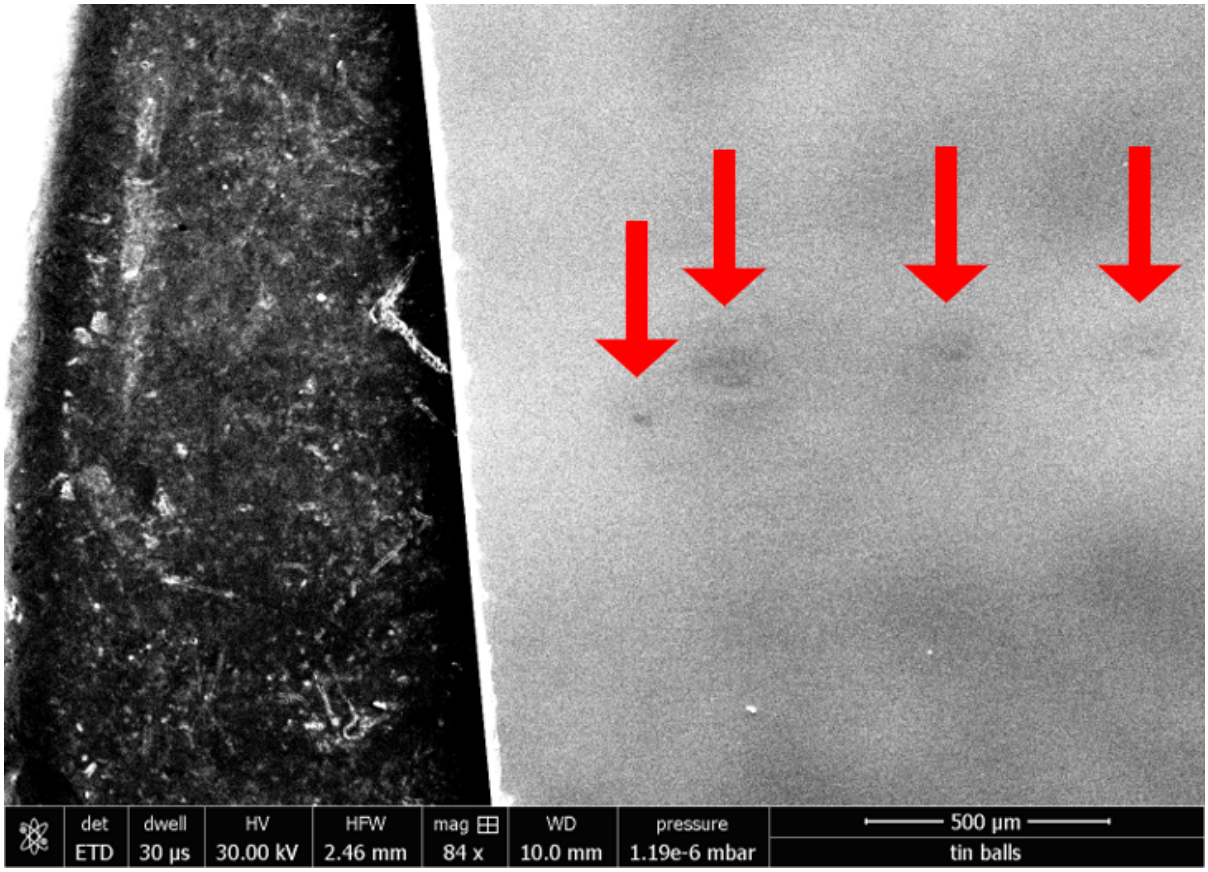

Figure 3.15: The above image shows a series of laser-induced burns on a Si substrate. The burns were made in succession from right to left while aligning the pump beam in the center of the SEM field of view.

location of the laser-induced burn, the alignment of the beam can be adjusted using the motorized mirror mount. A series of these adjustments is shown in Fig. 3.15. By making incremental adjustments, the beam can eventually be placed into a very small field of view. In cases where the magnitude of the adjustment is large, the alignment of the final lens may also be adjusted in order to maintain a normal angle of incidence.

Because the exact distance between the lens and the sample in the SEM chamber is difficult to measure, it is challenging to exactly place the focusing lens at the appropriate position. The lens can be focused by using a similar procedure as the general pump alignment, as shown in Fig. 3.16. The image on the left shows a relatively unfocused

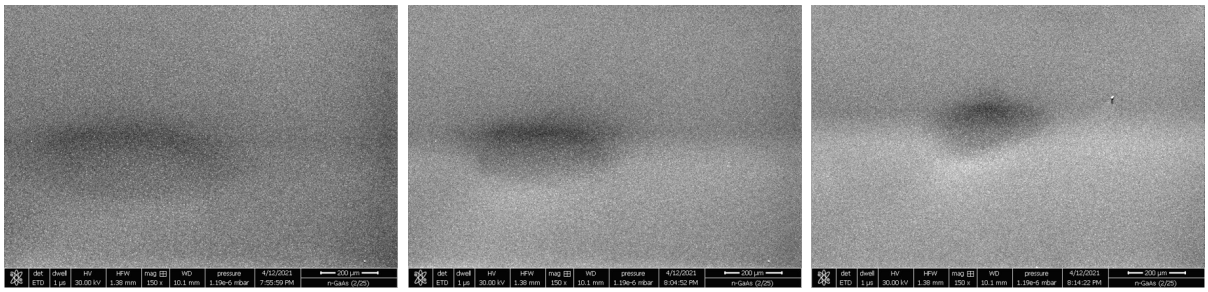

Figure 3.16: The above image shows a series of images taken after making small adjustments to the position of the final focusing lens. The left shows the pump spot on a GaAs sample when the beam is relatively unfocused. The next two images show the pump beam as it becomes more tightly focused.

beam, while the next two images show a slightly more focused pump. This procedure can be repeated until a minima is found.

3.5.1 In-chamber Lens Holder

When focusing a Gaussian beam using a lens with focal length f, the beam waist w at the focal point is given by:

$$w = \frac{\lambda f}{\pi w_0} \tag{3.3}$$

where λ is the wavelength and w_0 is the beam waist before the lens. Therefore, in order to produce a smaller pump spot size when using a given pump wavelength, the beam should be expanded before the focusing lens and/or a shorter focal length lens should be used.

The focusing lens used in the initial iteration of the SUEM setup had a focal length of 25 cm and was placed right outside of the optical window on the SEM chamber, as seen in Fig. 3.14. Therefore, in order to use a smaller focal length lens for pump focusing, it must be placed inside of the SEM chamber. Alex Ackerman, a Masters student in the Liao group, designed an in-chamber lens holder for this purpose. The lens holder is

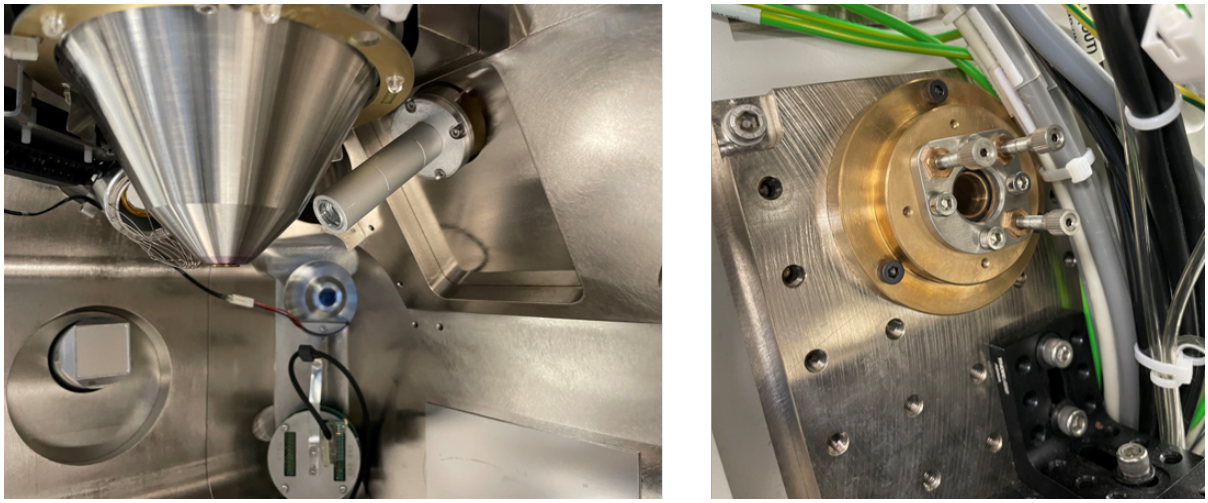

Figure 3.17: The image on the left shows the lens holder and attached lens tube from inside the SEM chamber. The SEM sample stage is out of view below the image. The right shows the lens holder from outside of the chamber. The three actuators can be used to manipulate the position of the lens. The full lens holder and schematic can be seen in Fig. A.8.

shown installed in the SEM in Fig. 3.17, while the uninstalled holder and a schematic are shown in Fig. A.8 in Appendix A.

The custom machined brass flange is placed into the SEM port, as shown in Fig. 3.17, where it replaces the stock optical access window and is able to hold vacuum at a comparable level. The lens holder has an integrated kinematic mount affixed on the vacuum side. The focusing lens is placed in a standard 1/2 inch diameter lens tubes which is threaded into the kinematic mount. Actuators located on the outside of the chamber are designed with dynamic seals, allowing them to manipulate the kinematic mount while the chamber is under vacuum. The actuators are used to adjust the placement of the beam on the sample, and can be manipulated in series in order to translate the lens along the axis of the beam in order to better focus it. An example of this process as well as an image of the pump spot on a GaAs sample are shown in Fig. A.9 in Appendix A.

Currently, a 5 cm lens is being used, but the modular nature of the lens tubes

allows for some flexibility. However, we were not able to use lenses below $f = 3$ cm due to clearance issues with the SEM pole piece.

Additional engineering is required in order to use shorter focal length lenses or a large objective lens, as the SEM geometry is not conducive to placing hardware close to the SEM sample stage on the axis normal to the SEM chamber wall due to the aforementioned clearance issues with the pole piece. Garming et al. integrated an inverted optical microscope below the sample stage in order to introduce a high NA objective and reported sub-micron pump pulses [122]. However, this limits their system to the study of thin samples as the excitation is provided from beneath the sample.

3.6 Finding Time Zero

Time-zero in pump-probe spectroscopies refers to the instance where the pump and probe pulses are incident on the sample instantaneously. Time-zero should occur within the range of delay times accessible to the experiment through movement of the delay stage. In optical spectroscopies, this is done by ensuring that the beam path lengths of the pump beam and probe beam are roughly the same. This same principle is applicable in when finding time-zero in SUEM, except that the reduced velocity of the probing electrons must be considered. Due to large accelerating voltages used, the velocity of the electrons reaches an appreciable fraction of the speed of light c, and relativistic effects must be considered. The relativistic velocity is given as:

$$v_{rel} = c\sqrt{1 - \frac{1}{\left(1 + \frac{V_a e}{m_e c^2}\right)}} \tag{3.4}$$

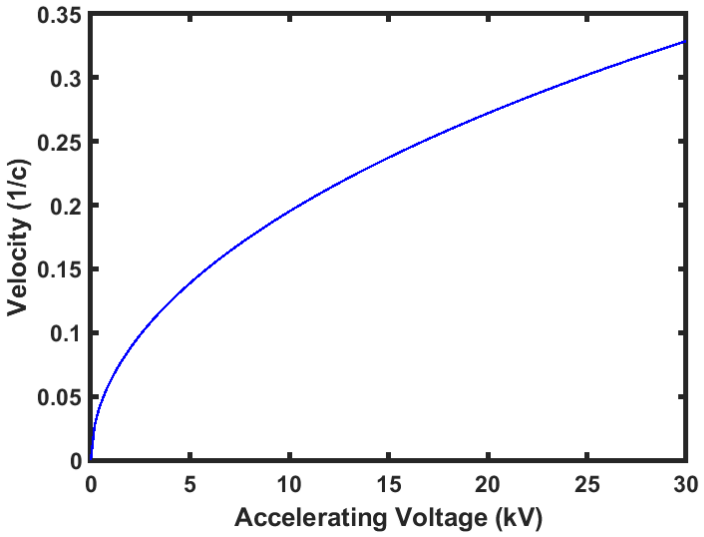

Figure 3.18: The velocity of electrons as a function of accelerating voltage, calculated using Eq. 3.4.

where V_a is the accelerating voltage and thus, the energy of the electrons, e is the electron charge, and m_e is the free electron mass. Figure 3.18 shows the velocity of primary electrons as a fraction of c as a function of accelerating voltage. The accelerating voltages shown are commonly found in commercial SEMs.

When accelerating using a 30 kV field, which has been the most commonly used field in SUEM experiments thus far, the primary electrons travel with a velocity of approximately $0.328c$. Therefore, when calculating time-zero, the path length of the electrons should be normalized by this value when defining the pump path.

When using lower accelerating voltages, an increase in the pump path length is required to maintain the same time zero as at 30 kV. Table 3.4 shows the additional path length required for a few commonly used accelerating voltages.

Once the pump and probe path lengths have been defined, the precise location of time-zero can be determined by performing SUEM measurements. In optical pump-probe

Accelerating Voltage (kV)	Additional Path Length (m)
20	0.32
10	1.06
5	2.11
2	4.21
1	6.58
0.5	9.94

Table 3.4: The additional path length relative to 30 kV required to maintain the same time zero is shown for various accelerating voltages. A travel distance of ≈ 0.6 m was used for all calculations.

experiments, no change in the relevant material property is observed at negative times, and time-zero is determined by the onset and subsequent decay of a material response. Similarly, in SUEM, no image contrast is observed at negative times. However, unlike in optical methods, the slow experimental process makes scanning the full available time domain laborious.

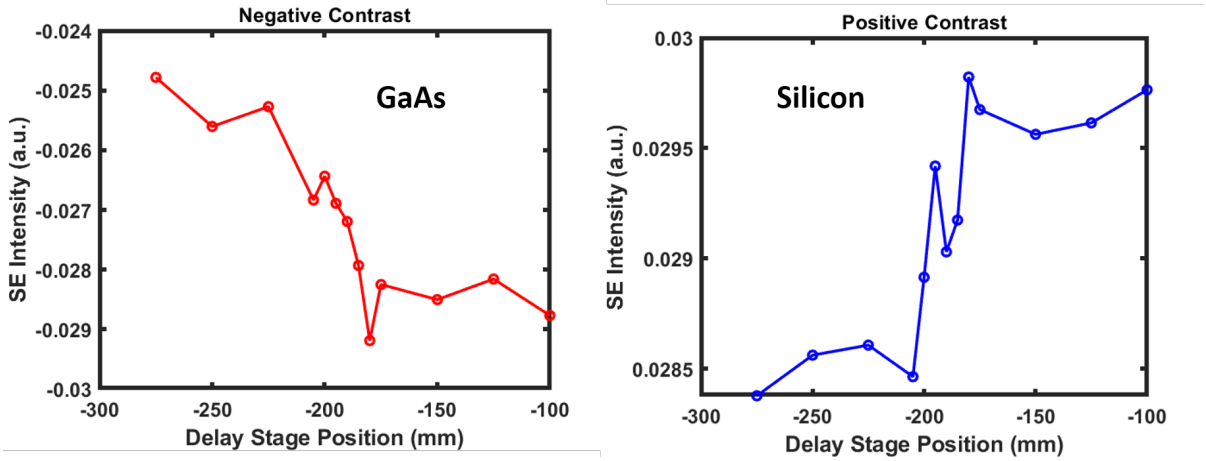

Figure 3.19: The above image shows the measured change in secondary electron emission on GaAs and Si. These measurements were taken to determine the rough position of time-zero after making alterations to the beam path.

When time-zero is unknown, rough measurements can be performed across the expected region. These images can then be analyzed for a change in SE contrast. Figure 3.19 shows two curves showing the change in SE emission as a function of delay stage

position on GaAs and Si samples. The figure is generated by calculating the average pixel intensity in the pump-illuminated region for each image. In this case, the sharp change in contrast from two separate samples suggests that time-zero occurs at the indicated delay stage position. This procedure can be repeated with finer temporal sampling in order to determine the precise time zero.

3.7 Image Formation

Currently the acquisition system from the standard SEM is used to collect the data used to produce SUEM images. To generate images, the SEM scans the electron beam pixel by pixel over the image area and collects the emitted SEs at each location. The number of collected SEs corresponds to the intensity of the pixel. The beam spends a certain amount of time, known as the dwell time, at each pixel.

When performing an SUEM experiment, one image is taken per delay time, with the acquisition time of the image being roughly one minute. Once an image is taken, the delay stage is moved to the next point another image is acquired. This procedure is repeated for each delay time of interest before acquiring the second set of images. Generally, several images are collected and averaged together per time point.

Due to instabilities in the probe current, the overall intensity of images at different time points can vary. In order to correct for this, each set of images for a certain experiment are normalized by the overall background intensity. This is done using the average background intensity in each image outside of the pump illuminated area. The pump illuminated area is excluded so as to exclude the dynamical contrast there, and also because the pump pulse produces DC changes in contrast that would effect the overall

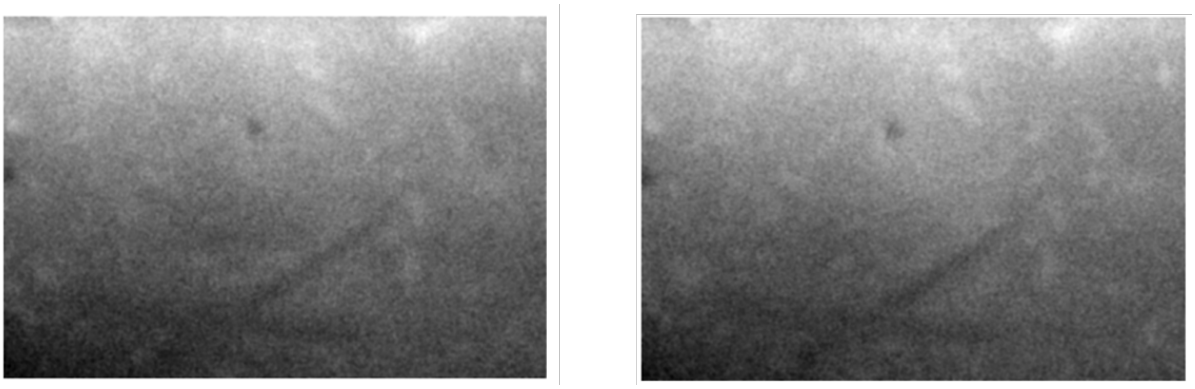

Figure 3.20: Raw SUEM images produced with the pulsed electron beam. The left image is the reference image while the right image is taken at a positive delay time. The changes in contrast in the raw images is extremely subtle.

distribution of the intensity of background pixels.

The normalized, averaged images contain static and low frequency information, such as defects on the sample and the aforementioned DC laser contrast. In order to correct for this, a differencing procedure is performed. An image from negative time, when the probe pulse impacts the sample before the pump pulse, is used as a reference image and subtracted from each subsequent image. Therefore, any contrast visible in subsequent images represents the change in contrast from that time t to the reference time t_{ref}. If the experiment is being performed in proper stroboscopic conditions, where no laser damage is induced and the sample relaxes completely between pumping events, contrast only becomes visible at positive times. This procedure significantly improves the signal to noise ratio of the SUEM images, as the change in contrast induced by the pump beam is quite small relative to the overall SE signal level.

Given that the background intensities have been normalized, the background pixels outside of the pump region have an average intensity value of zero. Any positive or negative deviation in intensity value in the pump region corresponds to a laser induced enhancement or suppression of SE emission, or, bright or dark contrast. Analysis of

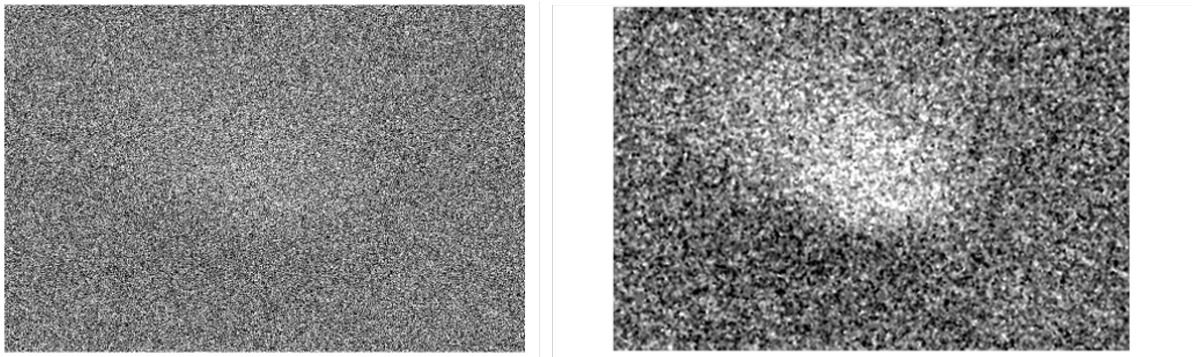

Figure 3.21: The left image shows the raw SUEM calculated difference image. The right shows the difference image after the contrast has been stretched.

SUEM datasets is performed on these images.

When plotting images for display, the mean background intensity is shifted to 0.5. Then, the images can be plotted in greyscale where pixel values below 0.5 correspond to dark contrast and values above 0.5 correspond to bright contrast. The pixel intensities can then be linearly stretched to accentuate image contrast by pinning the single brightest pixel to a value of 1 and the darkest value to zero. Typically, some image filtering is also performed in order to reduce noise.

Figure 3.20 shows two raw SUEM images, with the left image being the reference image and the right image being taken at some positive time. The observable difference between the two images is very small due to the low signal level of SUEM experiments. Figure 3.21 shows two difference images calculated using the images shown in Fig. 3.20. The image on the right has had its contrast stretched.

3.8 Pump Light Leakage

Secondary electrons can be detected in a variety of ways, including through in-chamber, in-lens, and in-column detection [171]. Among in-chamber detectors, microchannel plate (MCP) detectors have shown some usefulness in specialized applications [120,172,173], but by far the most common detector present in commercial SEMs is the Everhart-Thornley detector (ETD) [174]. The ETD was first described by Everhart and Thornley in 1960 and offered significant improvements over contemporary secondary emission electron multipliers, They concluded that their design offered essentially noise-free operation limited only by shot noise inherently present in the primary electron beam. The ETD, as shown in Fig. 3.22, contains a positively biased cage located in the chamber that attracts low energy SEs towards the detector. The SEs are accelerated towards an aluminum coated scintillator that is typically biased to around +10 kV. The main improvement of the ETD compared to previous state of the art detectors is the integration of a waveguide that directs light emitted by the phosphor out of the vacuum of the chamber towards a photomultiplier tube (PMT), after which it is converted back into an electrical signal which is processed and formed into images.

The aluminum coating on the scintillator is typically on the order of 10s of nm thick so that it is mostly transparent to the SEs that are accelerated into it and mostly reflective optically. However, the high fluences present in the SEM chamber during SUEM experiments means that if the Al film is even slightly transparent, pump light leakage through the film can easily overwhelm emission from the phosphor and saturate the detector. The transmissivity of a thin slab of material can be calculated straitforwardly,

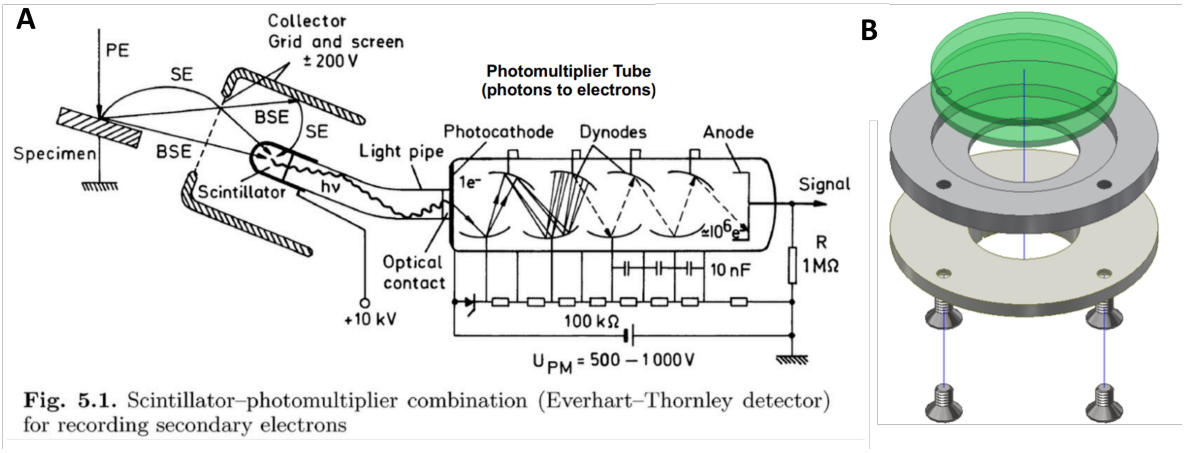

Fig. 5.1. Scintillator–photomultiplier combination (Everhart–Thornley detector) for recording secondary electrons

Figure 3.22: **Schematic of Everhart-Thornley Detector** (a) Schematic of an ETD, adapted from [175]. (b) Drawing of filter holder used to hold filters inserted into ETD to block pump light. The filters are placed after the light pipe, before the PMT.

and is given by Stratton [176] for normal incidence in air as:

$$T = \frac{(1-R)^2 + 4Rsin^2\delta}{(e^{\beta d} - Re^{-\beta d}) + 4Rsin^2(\delta + \alpha d)} \tag{3.5}$$

where $\alpha = (\omega/c)n_m = n_m k_0$, $\beta = (\omega/c)k_m = k_m k_0$, $n_m + ik_m$ is the refractive index, d is the thickness of the slab, and k_0 is the wavevector of the light. Also,

$$R = \frac{(1-n_m)^2 + k_m^2}{(1+n_m)^2 + k_m^2} \tag{3.6}$$

and

$$\tan\,\delta = \frac{2k_0\beta}{\alpha^2 + \beta^2 - k_0^2} \tag{3.7}$$

are needed. Equations 3.5-3.7 can be used to calculate the transmissivity of an Al film to different photon energies, as shown below in Fig. 3.23, and serves as a reasonable approximation of the transmission through the Al coated scintillator in the vacuum of the SEM. For a film thickness of 100 nm the value of T is approximately 5e-4 for 515

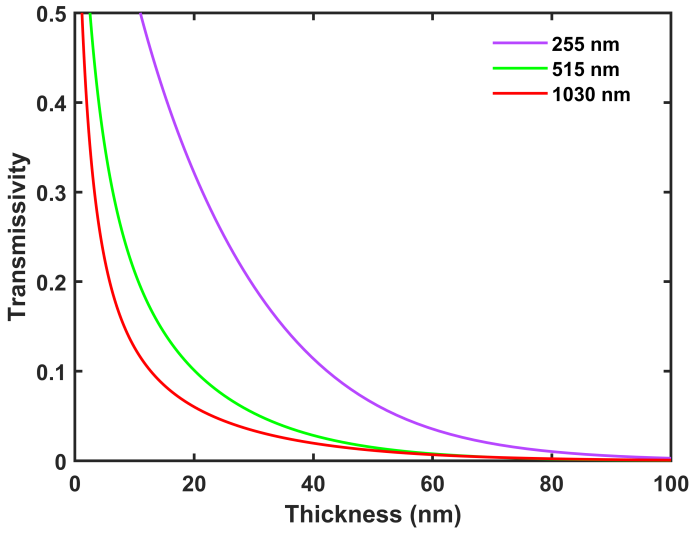

Figure 3.23: **Transmissivity of aluminum thin films.** The calculated transmissivity as a function of film thickness for the fundamental, 2nd, and 4th harmonics used in the SUEM setup. Refractive index data for aluminum was used from [177].

nm photons, equivalent to an OD 3.5 filter. Approximately 2% of incident photons are transmitted through a 50 nm film. In both cases, this level of leakage is sufficient to either significantly degrade image quality or outright saturate the detector. As such, it is necessary to add additional filtration of pump light to the ETD before the PMT.

The most common phosphor used in SEM detectors is Y_2SiO_5:Ce, also known as P47 [178–180]. P47 has an emission peak around 400 nm, with a tail that diminishes around 500 nm [181]. This makes it quite convenient to filter out pump light at 515 nm without attenuating any signal from the scintillator itself. Due to the geometry of the detector in the UCSB system, some small modifications to the ETD are necessary. In order to safely place filters within the ETD, a filter holder was designed by Alex Ackerman, a Masters student in the Liao group. This holder, shown in Fig. 3.22, was designed to be firmly affixed to the light pipe. There is no mechanical connection between the light pipe and the PMT, photons that travel through the light pipe are

Filters	Voltage (μV)
AVR	530
Asahi (2 filters)	330
Asahi (3 filters)	157
Asahi + Beam Dump	50

Table 3.5: **Pump Light Leakage into ETD.** Measurement of pump light leakage into the ETD using a LIA for different filtration schemes. Measurements were made with 10 mW of pump light directed into the SEM chamber.

simply transmitted through an optical window into the PMT. In order to retain efficient transport of photons into the PMT, the holder was designed to be sufficiently thin and wide so as to block ambient light from entering and to ensure that the filters are held flush to the PMT window, ensuring a normal incidence between the photons transmitted through the light pipe and the filters in the holder.

Quantifying the level of pump light leakage into the ETD is fairly straightforward. When the electron beam is off, there are no generated SEs capable of striking the scintillator and thus the only photons that can enter the detector are pump photons. By analyzing the detector output with the optical pump on and the electron beam off, the level of light leakage and the efficacy of different filtration configurations can be determined. The light leakage is measured by modulating the intensity of the pump with an AOM and then sending the ETD signal to a lock-in amplifier. The magnitude of the demodulated signal provided by the LIA is proportional to the leakage into the ETD, and is shown in Table 3.5 for several different schemes. Due to their 1 mm thickness, multiple low-pass filters from Asahi Spectra were placed in the filter holder, while only one from AVR Optics could be used. Note that using two or three OD 4.0 filters did not result in OD 8.0 or OD 12.0 attenuation due to the presence of multiple reflections from each of the coated surfaces on the filters [182]. The best performance was obtained by using multiple filters and by placing a beam dump made of blackout foil in the SEM

chamber in the path of the first specular reflection off of a sample placed at eucentric under the pole piece.

Chapter 4

Hot Carrier Diffusion in Boron Arsenide Single Crystals

4.1 History

4.1.1 Early Synthesis Attempts

The III-V family of semiconductors includes a wide variety of materials, from the wurtzite nitrides that have important applications in power electronics and as emitters [183–186], to the narrow gap InAs and InSb which have established uses in infrared detection as well as terahertz emission [187–190]. The boron family, outside of boron nitride (BN), has been less intensely studied. Cubic boron arsenide (BAs) is a semiconductor with a lattice constant of 4.778 Å and an indirect band gap of 1.82 eV [191] and has not been a particularly popular topic of research until recent predictions of ultrahigh thermal conductivity in excess of 1,000 W/mK [192]. In light of this prediction, interest in the material has skyrocketed, though the synthesis of BAs remains challenging and

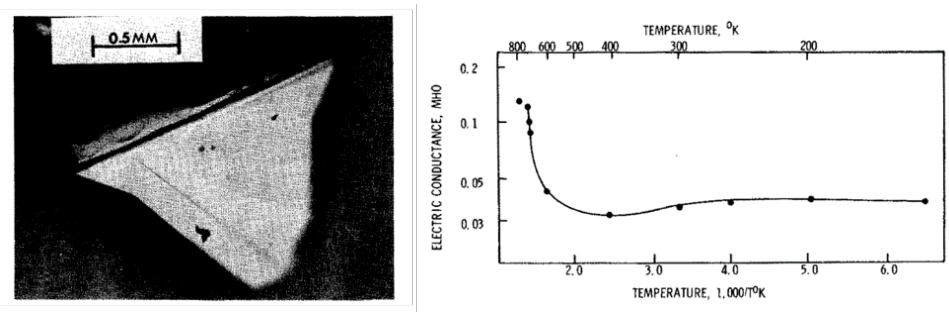

Figure 4.1: **Initial BAs Growth and Characterization.** Left: Optical image of BAs crystal grown via CVT. A twinned domain is clearly visible Right: conductance of BAs crystal as a function of temperature. The conductance shows no dependence on temperature below 400K. Image adapted from [199].

limited to small single crystal growth. Despite increased interest and study in the thermal properties of BAs, its electrical properties remain poorly characterized, with the process being largely inhibited by poor sample quality. Growth of quality thin films of BAs has been elusive, but would be necessary to enable further characterization of BAs, as well as for integration into useful devices.

The BAs crystal structure was first predicted by Welker & Weiss in 1956 [193], and first synthesized in 1958 by Perri et al [194]. They synthesized BAs and boron phosphide (BP), which was previously prepared in 1957 [195], by placing the constituent elements in silica tubes at elevated temperatures for 12 hours. Powder x-ray diffraction (XRD) measurements yielded lattice constants of 4.777 Å and 4.538 Å for BAs and BP respectively. They also found that in the presence of an arsenic vapor, BAs is stable up to 920°C, after which it decomposes into an orthorhombic phase. In 1960, Williams et al. reported the synthesis of BAs using similar methodologies and suggested a composition of B_6As for the orthorhombic phase [196]. In the 1960s, high pressure synthesis of BAs was reported [196, 197], as well as growth via chemical vapor transport (CVT) using iodine as a transporting reagent [198].

In 1972, Chu and Hyslop reported growth of BAs, also via CVT [199]. They produced polycrystalline BAs by combining boron, arsenic, and iodine in a closed tube. The tube was placed in a two-temperature furnace, with the boron end held at 900°C and the arsenic end held at 620°C. The reaction product formed in the center of the tube. For the CVT growth, the polycrystalline BAs, arsenic, and iodine were sealed in a tube, with the source end held at 900°C. The temperature difference between the source and growth ends was initially held at 10-15 °C, before being increased to 50°C. Pyramid shaped crystals 1-3 mm in size were obtained after two months of reaction time. An optical image of a representative crystal is shown in Fig. 4.1, with a twinned domain clearly visible. Chu and Hyslop determined their crystals to be intrinsically p-type, and were also able to perform electrical conductance as well as Hall effect measurements. They found that the electrical conductance is essentially independent of temperature between 77-500 K, indicating the presence of many shallow impurities. They also measured a Hall mobility of 100-400 cm^2/Vs between 77-300 K, though the measurement can not be considered fully quantitative due to the lack of a uniform cross-section in their samples. The lack of temperature variation indicates that impurity scattering dominates transport in their crystals.

In 1974, Chu and Hyslop published the first report on the growth of BAs films [200]. They used a gas flow system to thermally decompose a diborane-arsine mixture in a hydrogen atmosphere. The experimental apparatus is shown in Fig. 4.2. In order to suppress gas-phase nucleation due to thermal decomposition of the reagents, the researchers used low partial pressures of the reagents, a water-cooled reaction tube, and a high gas velocity over their substrates. They attempted to deposit films on three different substrates: the basal plane of hexagonal silicon carbide (SiC), (111) sodium fluoride (NaF), and (111) silicon. The deposition on NaF was not successful, as the films cracked

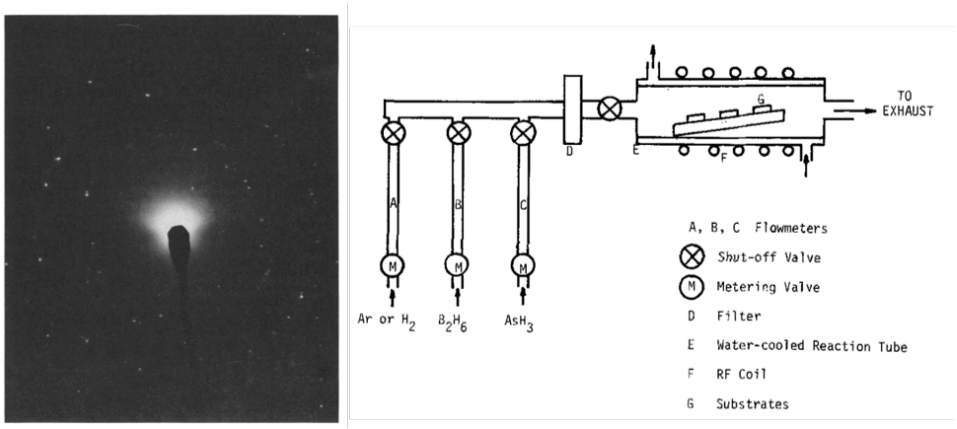

Figure 4.2: **Initial attempts at BAs thin film growth.** The image on the left shows a RHEED pattern of a BAs film grown on SiC. BAs domains show a random orientation. The right shows a schematic of apparatus used to decompose diborane-arsine mixture for BAs thin film growth. This remains the only reported attempt at growing thin films of BAs. Image adapted from [200].

off of the substrate during the cooling process, likely due to differences in the thermal expansion coefficients of the two materials. They were able to deposit adherent films onto SiC under a wide range of conditions. They determined that the films grown between 800-850°C were all BAs, but with random orientations. A representative RHEED pattern is shown in Fig. 4.2. The lack of single crystallinity is attributed to the large disparity in lattice parameter and the low growth temperatures. BAs grown on Si were adherent, but found to be amorphous. Sufficiently thick films were found to become convex upon cooling, indicating that BAs has a lower thermal expansion coefficient than Si. Chu and Hyslop removed the substrates from some of their samples in order to better characterize their films. They were not able to produce any high quality transport measurements from their films, and optical absorption data suggested that their films had a direct band gap of 1.45 eV, which has not been supported by later literature [191].

The BAs literature in the ensuing 35 years is scant. Prasad and Sahay perform a first principles electronic band structure calculation of BAs and BP, predicting an

indirect band gap of 1.27 eV [201]. There was some research into the properties of boron subarsenide [202–205], but very little work was published on BAs until the early 2010s, when theoretical predictions from the thermal transport community rekindled research interest in the material.

4.1.2 Predictions of Ultrahigh Thermal Conductivity

Improved theoretical understanding of phonon transport in crystals has enabled researchers to calculate the thermal conductivity of crystals with a high degree of accuracy. The lattice thermal conductivity of a crystal can be given as:

$$\kappa = \frac{1}{V} \sum_{\lambda} c_{\lambda} v_{g\lambda}^2 \tau_{\lambda} \tag{4.1}$$

where c_λ is the phonon mode specific heat, $v_{g\lambda}$ is the phonon group velocity, and τ_λ is the scattering time.

The mode specific heat can be evaluated directly based on the mode frequency, while the group velocity can be calculated from the phonon dispersion. However, calculating phonon-phonon scattering rates has been a limiting factor until recently. In 2007, Broido et al. developed an ab initio approach that iteratively solved the Boltzmann transport equation (BTE) using force constants calculated from density functional theory [206]. This method produced values for the lattice thermal conductivity that were within 5% of accepted experimental values in materials such as silicon, germanium, and diamond, among others without the use of any fitting parameters [207, 208]. After the initial successes of this framework, researchers sought to evaluate its predictive power by using it to identify previously unknown high thermal conductivity materials.

In 2013, Lindsay et al. used the BTE formalism to calculate the thermal conductivity of BAs [209]. Traditionally, potentially high thermal conductivity materials were evaluated based on four rules of thumb: 1) possessing a simple crystal structure, 2) having low average atomic mass, 3) strong interatomic bonding, and 4) low anharmonicity. Point 2) led to the prediction that BAs would have a thermal conductivity of around 200 W/mK, lower than that of BP or BN. As shown in Fig. 4.3, Lindsay's calculation predicted that BAs would have an ultra-high room temperature thermal conductivity in excess of 2,000 W/mK, approaching that of diamond. The high thermal conductivity has been attributed to the unique properties of the BAs phonon dispersion. Namely, the large acoustic-optical phonon band gap along with the bunching of the acoustic phonon modes, greatly inhibits scattering events between two acoustic phonons and one optical phonon by making energy conservation in these events very difficult. The suppression of this scattering event in particular greatly increases the thermal conductivity since acoustic phonons are the main heat carriers in semiconducting and insulating crystals.

This prediction rekindled interest in synthesizing BAs out of a desire to validate the predictive power of the BTE based thermal conductivity calculations. In 2015, Lv et al. synthesized BAs crystals and performed time domain thermo-reflectance (TDTR) measurements, shown in Fig. 4.4, in order to measure the thermal properties of their BAs samples [210]. They synthesized their crystals using a two-step process where first, a BAs powder was produced via a solid-state reaction. This powder was then used to grow single crystal BAs via CVT. The BAs powder was produced by sealing arsenic and boron with a B:As ratio of 1:1.8 in quartz tubes that were sealed under vacuum. The tubes were placed in a furnace that was heated up to 500°C for 10 hours, and then reacted at 800°C for three days. After one reaction, excess arsenic chunks were observed in addition to the BAs powder. These chunks were reground and dispersed within the powder, and

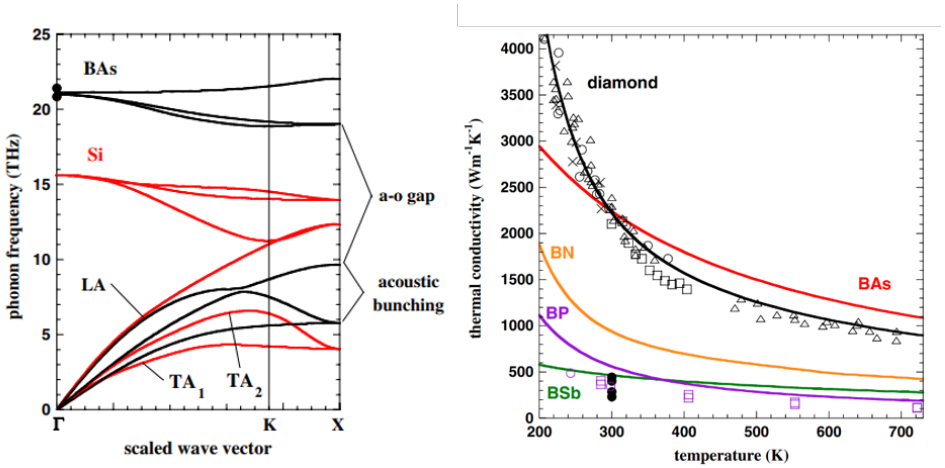

Figure 4.3: **BAs phonon dispersion and thermal conductivity.** On the left are the calculated phonon dispersions of BAs and Si. The bunching of acoustic modes and acoustic-optical bandgap in BAs restricts phonon scattering rates and increases the thermal conductivity. The Si phonon dispersion is included as a comparison. On the right are calculated thermal conductivities for the boron group III-V semiconductors as well as diamond. Experimental measurements are shown to demonstrate strong agreement with the calculations. Image adapted from [209].

the procedure was repeated several times until a homogenous, stoichiometric powder was obtained. This powder, along with extra arsenic and iodine as a transport reagent, were placed in a silica tube, which itself was placed into a two-temperature zone furnace for 2-3 weeks. The arsenic and iodine end of the tube was held at 900°C, while the BAs crystals grow in the cold end which was held at 650°C, and are shown in Fig. 4.4.

They extracted a thermal conductivity of ∼200 W/mK from their TDTR measurments, relatively high for semiconductor, but roughly an order of magnitude less than the predicted value. This discrepancy was largely attributed to the poorly tuned growth process, which produced defect laden crystals with observable twinned domains and an arsenic vacancy rate of ∼2.8%, which has been predicted to have significant effects on BAs thermal conductivity [211].

In 2017, refinements were made to the BTE formalism previously used to calcu-

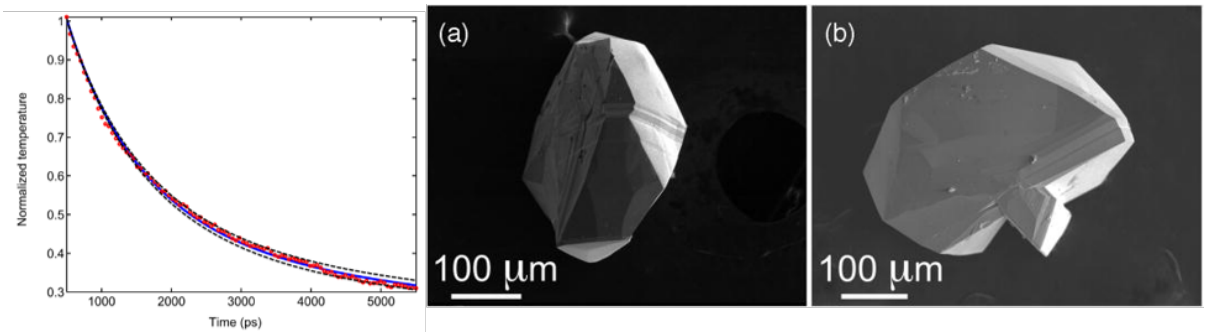

Figure 4.4: **TDTR measurements of BAs crystals.** On the left is a TDTR measurement taken from a BAs crystal. The extracted thermal conductivity was around 200 W/mK, significantly lower than predicted. On the right are the crystals that were measured. They represent the first attempt at BAs growth since the 1970s. Image adapted from [210].

lated the thermal conductivity in BAs that resulted in a decrease in the predicted thermal conductivity from 2,200 W/mK to 1,400 W/mK at room temperature [192]. Previous calculations solved the BTE in order to determine phonon scattering rates but limited the calculation to three phonon events and neglected higher order terms. At room temperature in most crystals, scattering events with four phonons or more occur at rates orders of magnitude below three phonon events, as shown in Fig. 4.5 for Si and diamond. However, in BAs, the large acoustic-optical phonon gap suppresses three phonon scattering events to such a large degree that the four phonon events become relevant. The inclusion of these events introduces new pathways for heat carrying acoustic phonons to scatter into optical phonons, greatly reducing the thermal conductivity.

Ultrahigh thermal conductivity was finally realized in 2018, when Li et al., Kang et al., and Tian et al. each reported measured thermal conductivities in excess of 1,000 W/mK at room temperature [212–214]. Single crystal samples in each of the papers were again grown via CVT, with minor variations present in each process. Kang et al., who measured a thermal conductivity of ∼1,300 W/mK, grew samples on BP substrates that were placed in their quartz growth tube. Tian et al. use a two-step growth process

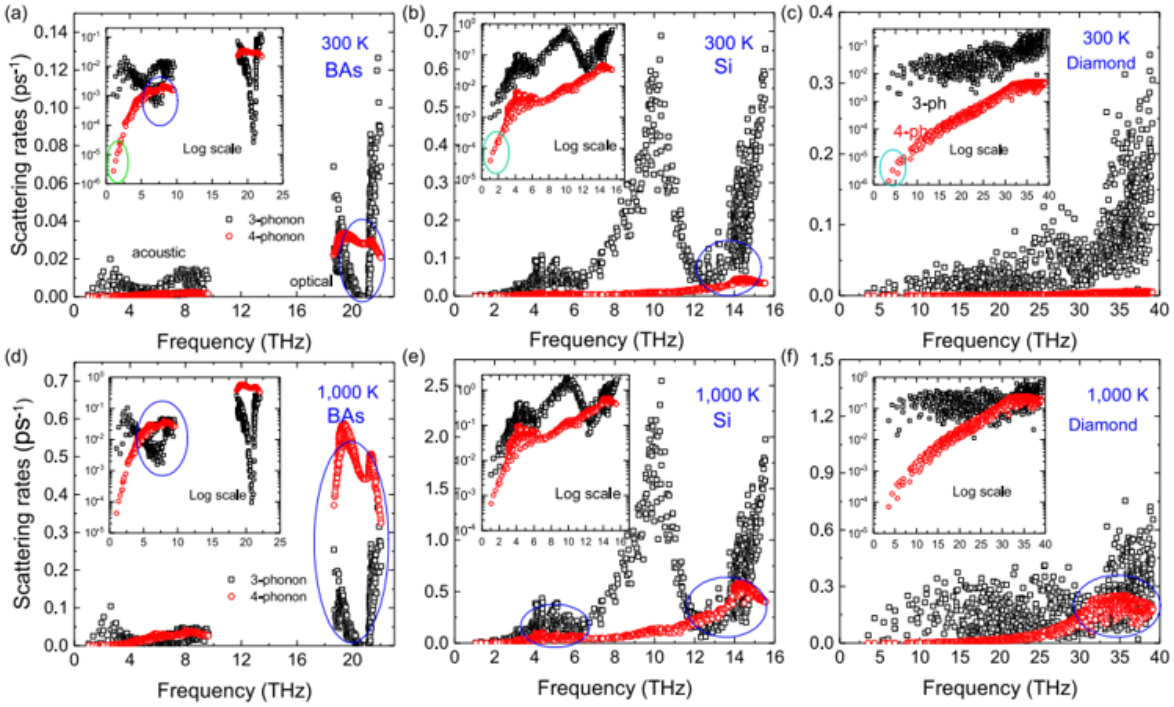

Figure 4.5: **Three and four phonon scattering rates for BAs, Si, and diamond.** Three and four phonon scattering rates are shown at 300K and 1000K. At 300K, four phonon scattering rates (red) of acoustic phonons are orders of magnitude lower than three phonon rates (black) for Si (b) and diamond (c). At 1000K, four phonon rates increase and become comparable to three phonon rates for Si (e) and diamond (f). In BAs, four phonon scattering rates are comparable to or greater than three phonon rates at 300K (a), and in some cases are significantly higher than three phonon rates at 1000K (d). Image adapted from [192].

where seed crystals are grown via CVT, which are then used as nucleation centers in a subsequent growth.

4.2 SUEM Experiments

In addition to its ultrahigh thermal conductivity, BAs has a thermal expansion coefficient that matches that of silicon and other III-V semiconductors, making it a suitable substrate material for device thermal management [215]. Besides the excel-

lent thermal transport properties, BAs is a semiconductor with a moderate band gap of 1.8 eV [216, 217]. First-principles simulation [218] has suggested a very high intrinsic charge mobility limited by electron-phonon interaction in BAs (electrons: 1,400 cm^2/Vs; holes: 2,110 cm^2/Vs). This is attributed to suppressed polar optical phonon scattering of charge carriers [218]. Optical spectroscopy studies have confirmed a particularly weak electron-phonon coupling strength in BAs [219]. Recent time-resolved optical measurements have also verified the predictions of high carrier mobilities [220, 221]. In addition, slow cooling of photoexcited hot carriers has been predicted in BAs using first-principles simulation, thanks to the large acoustic-optical phonon band gap that limits the thermalization process within the phonon system [222]. If experimentally verified, the combination of high thermal conductivity, high charge mobility, and prolonged hot carrier dynamics will make BAs an extraordinary candidate material for future optoelectronic, photovoltaic [223], and photocatalytic applications [224]. However, measuring charge transport properties in BAs has been challenging due to the lack of high-quality single crystals with a sufficient size for conventional bulk measurements, such as Hall effect and field effect studies. A large part of the recent research on BAs has centered on improving the quality of crystals and better characterizing the thermal and mechanical properties of BAs [191, 225–228]. While there have been some computation studies on the electronic properties of BAs [229–231], outside of the recent studies confirming high ambipolar mobility, previous electrical transport experiments have been limited to isolated studies that have suggested a hole mobility below 400 cm^2/Vs [199, 232], most likely due to the high concentration of impurities [227]. Moreover, there is currently no experimental report of the hot photocarrier dynamics in BAs.

This work reports the time-resolved imaging of photoexcited charge transport in high-quality BAs single crystals using SUEM. As perviously discussed, SUEM is a photon-

pump-electron-probe technique that uses short electron pulses with picosecond duration to image the response of a sample surface after the impact of a photon pulse [26, 124]. The change of local SE yield as a result of the optical excitation is measured and used to form contrast images [132]. Given the shallow escape length of SEs (a few nanometers), SUEM is highly sensitive to surface charge dynamics. A schematic of the experiment is shown in Fig. 4.6A. Briefly, the output from a femtosecond pulsed laser is split into a pump beam and a photoelectron-generation beam. The pump beam is converted to 515 nm, passed through a mechanical delay stage, and focused onto the sample to excite photocarriers. The photoelectron-generation beam is converted to 257 nm and focused onto the Schottky electron gun to generate electron pulses as the probe (the "primary electrons", PEs). The relative delay between the optical pump pulses and the PE probe pulses is controlled by the delay stage. The PE probe pulses are accelerated to 30 keV, focused and scanned over the sample surface by electron optics inside the SEM column. SEs emitted from each location on the sample surface as a result of the PE impact are collected by an ETD. The change of local SE yield after optical excitation, which is sensitive to the presence of photoexcited electrons and holes near the sample surface [26], is used to form SUEM contrast images. These images directly visualize the surface distribution of photocarriers at various delay times after optical excitation. The spatial resolution of these images is determined by the size of the PE beam (a few nanometers) and the time resolution is limited by the duration of the PE pulses (a few picoseconds with less than 100 electrons per pulse) [135, 150].

The BAs samples studied were prepared using a chemical vapor transport method, as reported by Gamage et al [233], additional details can be found in Appendix B. The SEM image of a representative sample is shown in Fig. 4.6B. The x-ray diffraction (XRD) pattern shown in Fig. 4.6C verifies the high quality of the single crystal samples measured

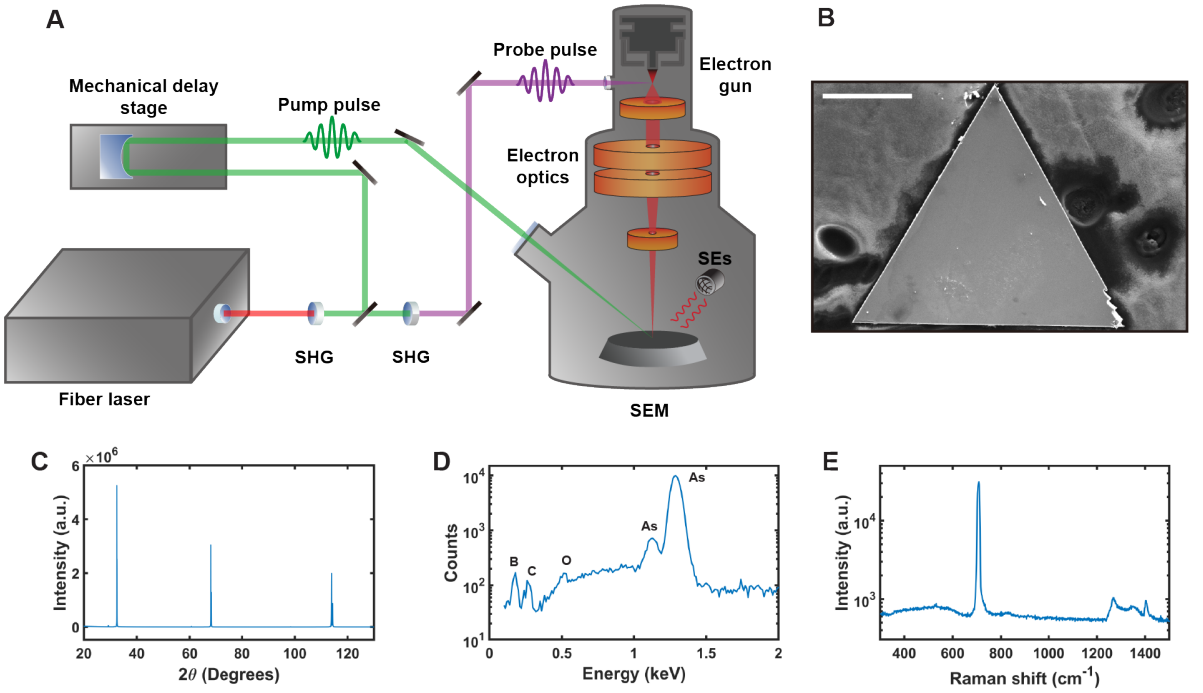

Figure 4.6: **BAs sample and characterization.** (a) A schematic of the SUEM setup combining a femtosecond ultrafast laser with a scanning electron microscope (SEM). (b) BAs single crystal sample from Ren group at the University of Houston. (c)-(e) XRD, EDS and Raman characterization of BAs sample.

in this study. SEM-based energy dispersive spectroscopy (EDS) (Fig. 4.6D) suggests that carbon and oxygen are the major impurities. X-ray photoelectron spectroscopy (XPS) measurements also find the same impurities on the sample surface and are shown in Appendix B in Fig. B.1, Fig. B.2, and Table B.1. A Raman spectrum is shown in Fig. 4.6E, where the narrow linewidth suggests a low impurity concentration. Additional detailed structural and defect characterization of the BAs samples used in this study have been reported elsewhere [220, 221, 227, 233].

4.2.1 Low-Fluence Experiments

Fig. 4.7A displays representative SUEM contrast images obtained on a BAs single crystal. For this dataset, an optical pump fluence of 100 μJ/cm^2 was used. More

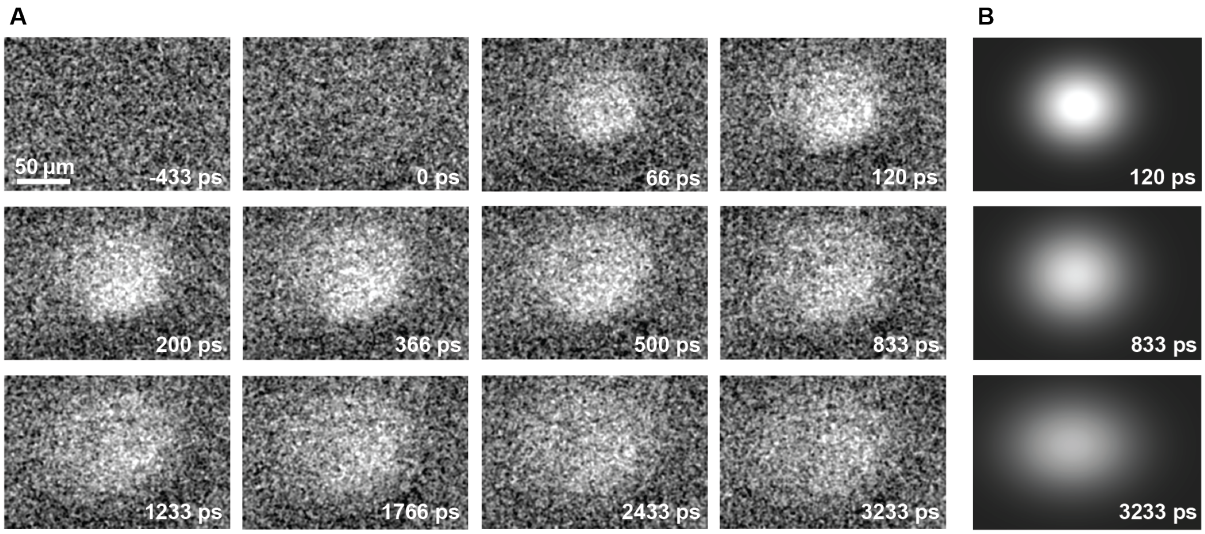

Figure 4.7: **Timelapse of Carrier Dynamics in BAs.** (a) SUEM difference images from selected time points throughout the experiment. No contrast is visible at negative time, before the arrival of the pump pulse (at 0 ps). After the arrival of the pump pulse, a small area of bright contrast emerges. This region rapidly expands for a few hundred picoseconds, before continuing to slowly expand and decrease in intensity over the next few nanoseconds. (b) Representative two-dimensional Gaussian fits of the experimental contrast images

datasets taken from different samples with different optical pump fluences are included in Appendix B (Table B.2, and Figs. B.5-B.8). Each contrast image was obtained by subtracting a reference SE image taken at -700 ps delay time from the SE image taken at a later delay time. Thus, the SUEM contrast images reflect the change in SE emission from the sample surface as a result of the pulsed photoexcitation that arrives at time zero. As shown in Fig. 4.7A, no obvious contrast was observed before time zero, indicating that the time interval between pump pulses (200 ns at 5 MHz repetition rate) is sufficiently long for the excited sample to return to the equilibrium state.

After time zero, a bright contrast within the pump-illuminated region emerges and its size grows in time. The bright contrast signals a higher SE yield from the region, which is caused by the presence of photoexcited charge carriers. Photocarriers modify the average energy of the electrons locally that can affect the SE yield [26]. In addition,

photocarriers can modulate the surface electrostatic potential (i.e., the surface photovoltage effect [132]), providing another mechanism for the SE yield contrast. Accordingly, the bright contrast in the SUEM images is interpreted as an indicator for the distribution of the photocarriers near the sample surface. Therefore, the growth in the spatial size of the bright contrast as a function of the delay time between the optical pump and the electron probe corresponds to the lateral diffusion of photocarriers. In this manner, the dynamics of photocarriers near the sample surface can be directly visualized in the SUEM contrast images. When the optical pump fluence is low, photogenerated electrons and holes diffuse together with an intermediate diffusivity due to their Coulombic interaction. This is called the "ambipolar diffusion" regime. From Fig. 4.7A, an initial fast expansion of the bright contrast is observed up to a few hundred picoseconds, after which the expansion starts to slow down.

4.2.2 Hot Carrier Diffusion Model

Because the optical pump beam has a Gaussian spatial profile with a $1/e^2$ radius of 30 μm, the initial distribution of the photocarrier concentration should also follow a Gaussian profile in the radial direction. Along the sample thickness direction, the optical pump is absorbed with a penetration depth on the order of a few microns [216]. Since the lateral diffusion process preserves the Gaussian spatial profile, a least-square fitting algorithm is used to fit the spatial distribution of the bright contrast at each delay time to a two-dimensional Gaussian function:

$$I(x,y,t) = A(t)\exp\left[-\left(\frac{(I(x,t)-x_0)^2}{r_x(t)^2}+\frac{(I(y,t)-y_0)^2}{r_y(t)^2}\right)\right] \tag{4.2}$$

where $A(t)$ is the amplitude of the distribution, and $r_x(t)$ and $r_y(t)$ are the $x-$ and $y-$ radii respectively. Some representative fits of the SUEM images are shown in Fig. 4.7B. The fitted squared radius of the photocarrier distribution as a function of delay time is shown in Fig. 4.8A. The error bars represent 95% confidence intervals. Early data points (<40 ps) are noisy due to the initial weak contrast, and thus, are not shown here for clarity (but are included in some datasets in Appendix B). Consistent with the SUEM contrast images shown in Fig. 4.7A, the fitted squared radius shows an initial fast diffusion regime that slows down after a few hundred picoseconds. The initial fast diffusion was also observed in crystalline silicon [127] and amorphous silicon [128] and is a result of the transport of photoexcited hot carriers. Since the photon energy of the optical pump ($h\nu = 2.4$ eV) is higher than the band gap in BAs ($E_G \approx 1.8$ eV) [216], the initial temperature of the photocarriers after excitation can be estimated to be $T_i = (h\nu - E_G)/k_B = 4,700$ K. In addition, the hot photocarriers occupy higher energy states from the band edges and can possess higher band velocities and experience reduced electron-phonon scattering [234]. Therefore, the effective diffusivity of the hot photocarriers can be orders of magnitude higher than the equilibrium value.

The hot carrier lifetime and diffusivity can be extracted from the low fluence experimental data using a simple diffusion model. Given the axial symmetry of the experimental geometry, the diffusion process of photocarriers is governed by the following equation:

$$\frac{\partial n}{\partial t} = D(t)\left[\frac{1}{r}\frac{\partial}{\partial r}\left(r\frac{\partial n}{\partial r}\right) + \frac{\partial^2 n}{\partial x^2}\right] \tag{4.3}$$

where n is the density of electrons or holes, $D(t)$ is a time-dependent effective diffusivity, r is the radial distance from the center of the optically excited area, z is the depth into the sample from the surface. The time-dependent diffusivity is proposed due to the observation of an initial fast expansion and a following slow expansion of the SUEM

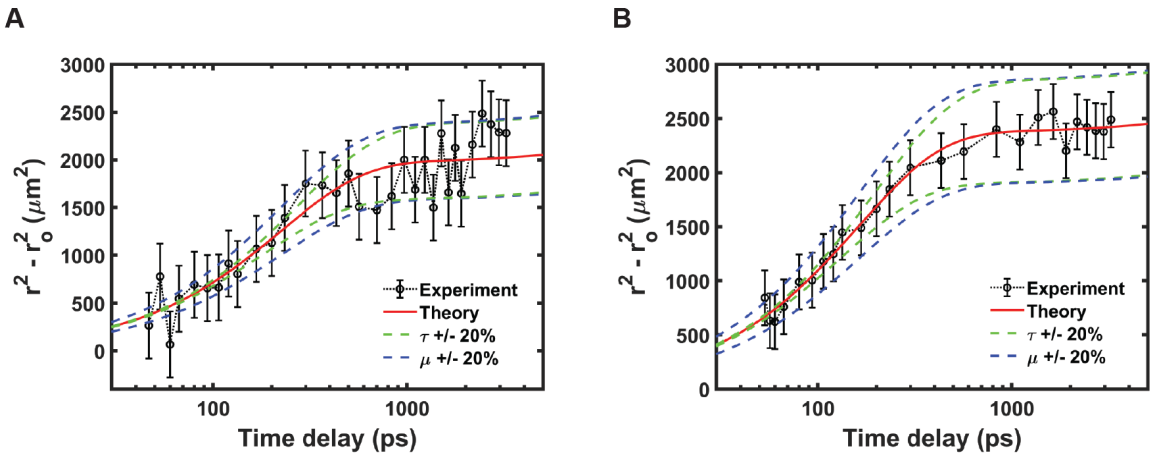

Figure 4.8: **BAs experiment vs. model.** (a) Squared radius (r^2) of the bright contrast as a function of the time delay with an optical fluence of 100 μJ/cm^2. (b) Squared radius of the bright contrast as a function of the time delay with an optical fluence of 130 μJ/cm^2. r_0 is the radius of the optical pump beam that defines the radius of the initial photocarrier concentration distribution. The black circles label the experimental data. The error bars represent 95% confidence levels in fitting the data to the 2D Gaussian model. The dotted black line serves as a guide to the eye. The red solid line denotes the theoretical model. The green and blue dashed lines label the theoretical model when the time constant τ and the equilibrium ambipolar mobility μ are changed by 20%.

image contrast. Due to electron-phonon scattering, however, the hot photocarriers will cool down to the band edges and the diffusivity will approach the equilibrium value. To quantitatively model this process, we assume the effective diffusivity of the photocarriers decays exponentially with a time constant τ and has the form:

$$D(t) = (D_i - D_0) \exp\left(\frac{-t}{\tau}\right) + D_0 \tag{4.4}$$

where D_i is the effective diffusivity immediately after photoexcitation, and D_0 is the equilibrium diffusivity at 300 K.

The recombination term is excluded from Eqn. 4.3 because it is assumed that the electron-hole recombination timescale is much longer than the diffusion timescale. A

recent optical study of BAs suggested a recombination time beyond 20 ns [219]. This long electron-phonon recombination time could be due to the indirect band gap, and justifies the approach to not including a recombination term in Eqn. 4.3. The effective diffusivity is assumed to decay exponentially in time as the hot carriers cool down. Immediately after the photoexcitation, the distribution of the photocarrier density has the following form:

$$n(r, t = 0) = n_0 \exp\left(\frac{-2r^2}{R_0^2}\right) \exp\left(\frac{-z}{d}\right) \tag{4.5}$$

where n_0 is the photocarrier density at the center of the illuminated area on the surface, R_0 is the $1/e^2$ radius of the optical pump beam, and d is the optical absorption depth. There is large uncertainty in the optical absorption depth in BAs as determined by different methods, and the reported optical absorption depth in BAs varies from 1 μm to tens of microns [216]. Using the initial condition provided in Eqn. 4.5, Eqn. 4.3 can be solved numerically using a finite differencing method. Doing so reveals that the diffusion along the thickness (z) direction changes the magnitude of the surface photocarrier density appreciably but has a small impact on the temporal evolution of the radius of the surface photocarrier density distribution within the range of possible optical absorption depth, as shown in Fig. 4.9. Therefore, to understand the dynamics of the surface photocarriers as observed in the SUEM experiments, a two-dimensional radial diffusion equation can be solved analytically by omitting the z-direction diffusion term.

Because the initial surface photocarrier density distribution follows a Gaussian distribution with a time-dependent radius, a solution of a similar form can be assumed:

$$n(r, t) = n_0(t) \exp\left(\frac{-2r^2}{R^2(t)}\right) \tag{4.6}$$

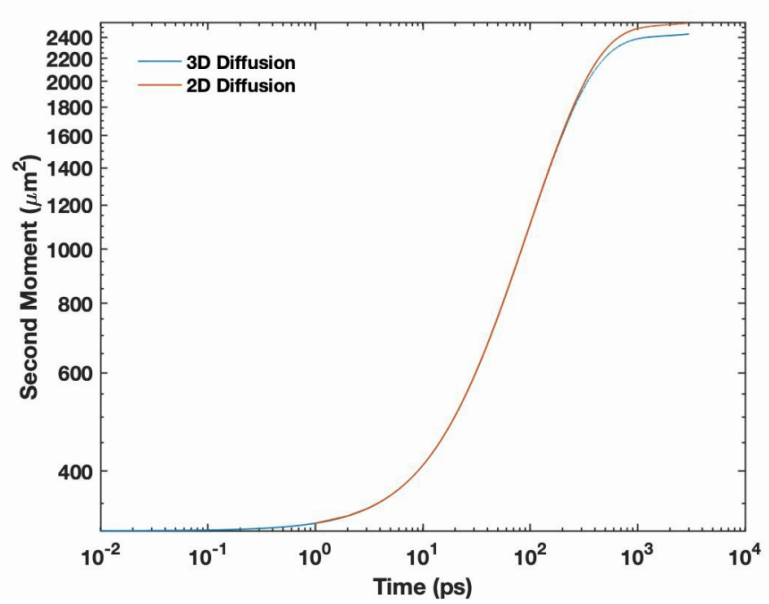

Figure 4.9: **Comparison of the 2D analytical diffusion model with 3D numerical model.** For the 3D numerical diffusion mode, an optical absorption depth of 1 μm was used. The other parameters used here were realistic ones extracted from the SUEM measurements of BAs. The y-axis represents the second moment of the spatial distribution of the charge carriers, equivalent to the radius squared extracted from SUEM images. The two models agree with each other very well at earlier delay times and slightly deviates after 1 ns, with the maximum difference below 5%.

Substitution of this solution into the radial diffusion equation leads to the following equation governing the time dependence of $R(t)$:

$$\frac{dR}{dt} = \frac{2D(t)}{R} = \frac{2}{R}\left[(D_i - D_0)\exp\left(\frac{-t}{\tau}\right) + D_0\right] \tag{4.7}$$

This equation can be analytically solved to give the following time dependence of $R(t)$:

$$R(t)^2 - R_0^2 = 4(D_i - D_0)\tau(1 - \exp\left(\frac{-t}{\tau}\right) + 4D_0 t \tag{4.8}$$

Given the large uncertainty in the optical absorption depth d and the weak dependence of $R(t)$ on the z-direction diffusion, Eqn. 4.8 can be used to fit the experimental results and quantitatively analyze the diffusion process visualized in the SUEM contrast images,

as shown in Fig. 4.8A. The initial diffusivity of the hot photocarriers extracted from the BAs measurements ranges from 15,000 cm^2/s to 45,000 cm^2/s, which is on the same order with the values extracted from other SUEM measurements of silicon [127] and CdTe [156]. The effective equilibrium diffusivity $D_0 \approx 45$ cm^2/s was used for the fitting, corresponding to an equilibrium ambipolar mobility $\mu \approx 1{,}700$ cm^2/Vs, based on the mobility calculated from first principles [218] and the Einstein relation, and kept the time constant τ as a fitting parameter. For the dataset shown in Fig. 4.7 and Fig. 4.8A, the fitted time constant τ is 220 ps. To show the model sensitivity to these parameters, bounds corresponding to varying μ and τ by 20% are also plotted in Fig. 4.8A. More datasets are presented in Appendix B. Within these datasets, the time constant τ ranges from 145 ps to 250 ps and seems to decrease with increasing optical fluence, suggesting the onset of Auger recombination. A dataset with higher optical fluence (130 $\mu J/cm^2$) and a fitted time constant τ of 160 ps is shown in Fig. 4.8B.

4.2.3 Hot Phonon Bottleneck

The hot carrier transport time constant τ (up to 250 ps) extracted from our SUEM measurements of BAs is significantly longer than that in Si (~100 ps on average) [127], as shown in Fig. 4.10. The slow hot carrier cooling process is likely due to the same feature in the phonon dispersion that leads to the high thermal conductivity in BAs: the large acoustic-optical phonon band gap caused by the large mass ratio between boron and arsenic atoms [222]. Owing to the strong polar optical phonon scattering of electrons in BAs, the hot carrier energy is first transferred to the polar optical phonons, and the large acoustic-optical phonon frequency gap prevents effective scattering between optical and acoustic phonons, creating a bottleneck in the hot carrier cooling pathway.

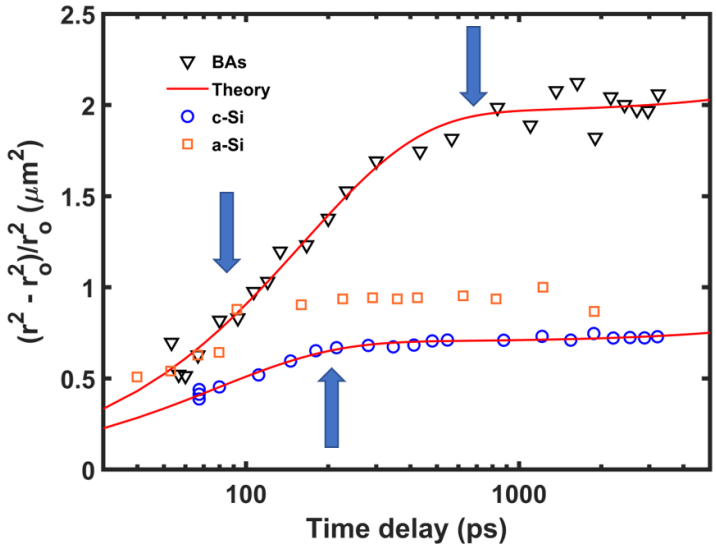

Figure 4.10: The above figure shows a comparison of SUEM measurements of BAs, amorphous silicon (a-Si), and crystalline silicon (c-Si). The arrows represent the time delay after which hot carrier transport contributions to observed diffusion transitions into near-equilibrium. Data for a-Si and c-Si are adapted from [128] and [127] respectively.

Next, a simple heuristic analysis of the phonon bottleneck effect is provided. Consider one electron with initial momentum k that absorbs a phonon with momentum q. After the absorption process, the electron transits to a new state with momentum $k' = k + q$. Based on Fermi's golden rule, the probability for this process to happen is given by [235]:

$$P_{k\to k',q} = \frac{2\pi}{\hbar}|g_{k,k'}|^2 f_k(1 - f_{k'})n_q\delta(E_k - E_{k'} + \hbar\omega) \tag{4.9}$$

where $g_{k,k'}$ is the electron-phonon coupling matrix element, f_k and n_q are the distribution functions for electrons and phonons, respectively, and $\hbar\omega$ is the energy of the absorbed phonon. Similarly, the inverse process, where an electron with initial momentum k' emits a phonon with momentum q and transits back to k, should happen with the following probability:

$$P_{k'\to k,q} = \frac{2\pi}{\hbar}|g_{k,k'}|^2 f_{k'}(1 - f_k)(n_q + 1)\delta(E_k - E_{k'} + \hbar\omega) \tag{4.10}$$

These two equations indicate that both the phonon absorption rate and emission rate increase with the phonon population n_q. Now assuming the electrons and the phonons are, at first, at thermal equilibrium with the same temperature. In this case, the detailed balance principle requires that the phonon absorption and emission rate must balance each other [236]:

$$f_{k,0}(1 - f_{k',0})n_{q,0} = f_{k',0}(1 - f_{k,0})(n_{q,0} + 1) \tag{4.11}$$

This equation can also be explicitly verified when $f_{k,0}$ and $n_{q,0}$, are the Fermi-Dirac distribution and Bose-Einstein distribution, respectively, with the same temperature, taking into account the energy conservation condition $E'_k = E_k + \hbar\omega$. Then, assuming a non-equilibrium condition has been created, as in the case of hot photocarrier cooling, where the electrons are at a much higher temperature than the phonons. For simplicity, assume the phonon population deviates from its equilibrium value by Δn_q:

$$n_q = n_{q,0} + \Delta n_q \tag{4.12}$$

Under this condition, the net rate of phonon population change can be calculated as the difference between the absorption rate and the emission rate (incorporating Eqn. 4.11 to Eqns. 4.10 and 4.9):

$$\begin{aligned} P_{k\to k',q} - P_{k'\to k,q} &= \frac{2\pi}{\hbar}|g_{k,k'}|^2\,\delta(E_k - E_{k'} + \hbar\omega)(f_{k,0} - f_{k',0})\Delta n_q \\ &\approx -\frac{2\pi}{\hbar}|g_{k,k'}|^2\,\delta(E_k - E_{k'} + \hbar\omega)(f_{k,0} - f_{k',0})\frac{\partial f_{k,0}}{\partial E}\hbar\omega\Delta n_q \end{aligned} \tag{4.13}$$

This result indicates that an increased phonon population will lead to a net phonon absorption rate, while a decreased phonon population will lead to a net phonon emission rate. A more general analysis involving all electron-phonon scattering channels is given by Chen [236], in Eqns. (8.18) to (8.33). The main conclusion is that the net energy

exchange between the electron population and the phonon population is proportional to their temperature difference, such that a higher optical phonon temperature (equivalent to a higher optical phonon population) will lead to a decreased net rate of phonon emission and, thus, cause the phonon bottleneck effect.

It should be noted that there are other possible factors that can contribute to the long hot carrier transport in BAs. For example, a recent time-resolved optical spectroscopy study reveals an ultraweak electron-phonon coupling strength in BAs [219], which can lead to slow cooling of the hot photocarriers. However, the contribution from higher energy valleys can be ruled out because the next excitable valley (at Γ) has a direct band gap of 4.12 eV [216], which is much higher than the photon energy used in the optical pump. In addition, a time-resolved optical reflectivity measurement of BAs was performed, shown in Fig. B.3, where a similar timescale for hot carrier transport was observed.

4.2.4 High-Fluence Experiments

SUEM measurements were conducted using a range of different optical pump fluences. When the optical fluence stayed below 130 μJ/cm^2, there is no observable qualitative change in the photocarrier dynamics (additional image sets are shown in Appendix B), suggesting that the observed dynamics were within the linear regime. At higher fluences above 180 μJ/cm^2, however, the observed features in the SUEM contrast images become qualitatively distinct, namely: the formation of an outer dark region and an inner bright region, both regions expanding with time, as shown in Fig. 4.11A. The optical fluence for this dataset is 235 μJ/cm^2. Another dataset with 185 μJ/cm^2 fluence is shown in Fig. B.10. This observation can be explained by the separate diffusion

of faster holes and slower electrons [218] beyond the ambipolar diffusion regime (Fig. 4.11B). This phenomenon is reminiscent of the photo-Dember effect [237] and similar to the charge separation observed in silicon, where electrons diffuse faster than holes, under higher optical pump fluences [238].

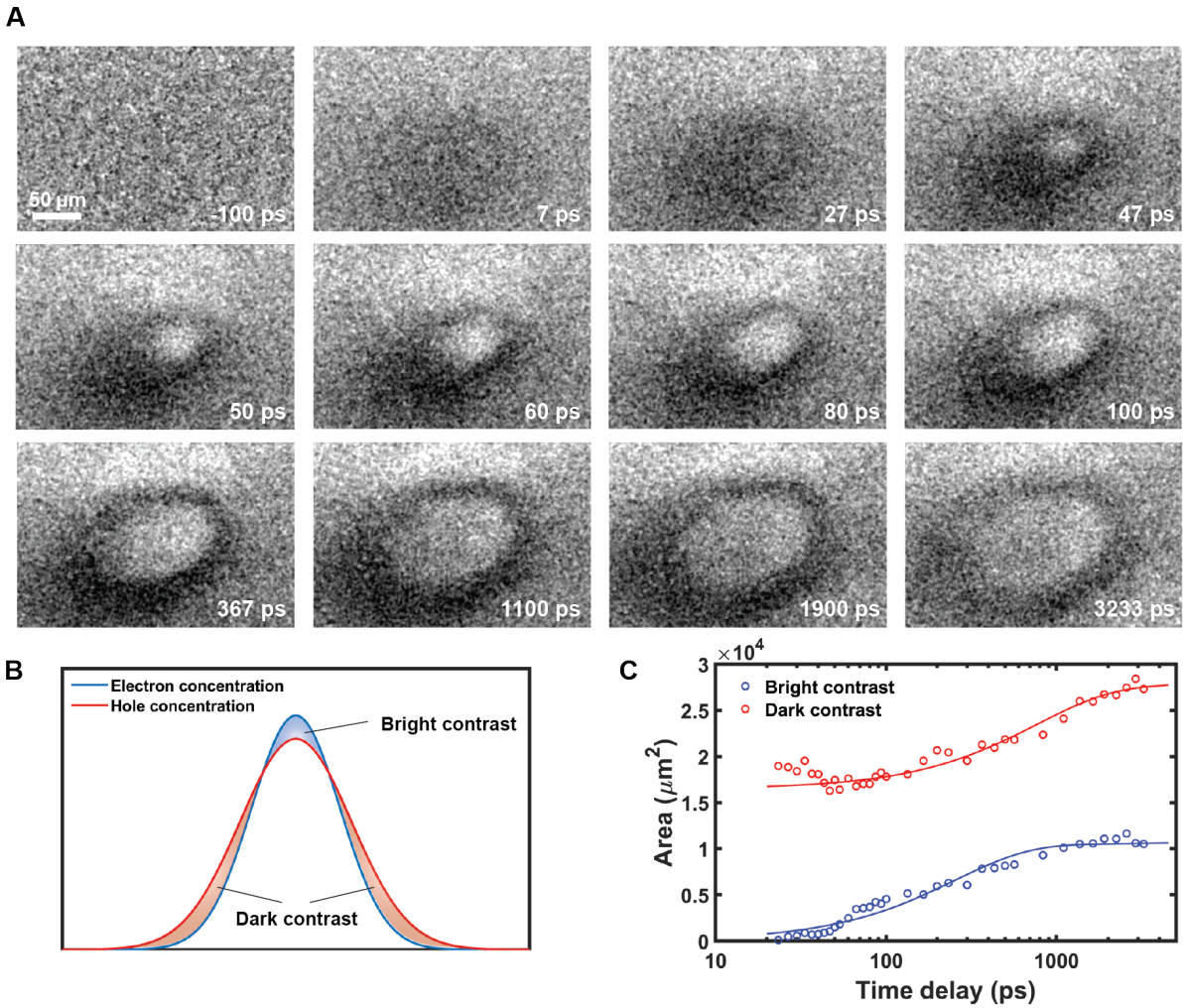

Figure 4.11: **SUEM images at high optical fluence showing separation of electrons and holes.** (a) The SUEM contrast images taken with an optical fluence of 235 μJ/cm^2. (b) A schematic showing the separation of electrons and holes and the corresponding SUEM contrasts. (c) The evolution of the areas of the bright and the dark contrast regions as a function of delay time. The solid lines represent fits using Eqn. 4.8 with parameters given in the main text.

Assuming the electron and hole populations are diffusing separately, an approach similar to the used for the low fluence measurements can be used. Assuming the carriers continue to diffuse with a Gaussian distribution, the images can be fit to two Gaussian distributions:

$$\begin{aligned} I(x,y,t) = A_e(t)\exp\left[-\left(\frac{(I(x,t)-x_0)^2}{r_{x,e}(t)^2}+\frac{(I(y,t)-y_0)^2}{r_{y,e}(t)^2}\right)\right] \\ +A_h(t)\exp\left[-\left(\frac{(I(x,t)-x_0)^2}{r_{x,h}(t)^2}+\frac{(I(y,t)-y_0)^2}{r_{y,h}(t)^2}\right)\right] \end{aligned} \tag{4.14}$$

where the first term corresponds to the spatial evolution of the electron distribution, the second term corresponds to the hole distribution, and x_0 and y_0 are the coordinates of the centers of both of the distributions. Extracted values for the amplitude and radii of the electron and hole distributions using this method are shown in Fig. B.11. While this procedure produces reasonable fits at early times, it is not as effective at later times. This is evident in the extracted radii and amplitude values, which converge and diverge in magnitude after ≈1 ns. The inability of the fitting procedure to capture the observed dynamics is likely due to the addition of several added fitting parameters, which results in a very insensitive process.

In order to approximate the dynamics visible in the SUEM images shown in Fig. 4.11, a more qualitative approach was tried. The approximate area of the dark and bright contrast regions can be approximated by counting the number of pixels within the pump illuminated region that have either a positive or negative value at each time delay. The area of each pixel can then be estimated using the image resolution and the horizontal field width of the images. By counting the change in the number of bright and dark pixels as a function of delay time, the approximate area of the electron and hole concentrations can be estimated.

Figure 4.11C shows the evolution of the areas of the dark and the bright regions as a function of the delay time, where the initial separation and the convergence towards ambipolar diffusion can be observed. Equation 4.8 can be used along with the calculated equilibrium electron and hole mobilities to fit the experimental data and doing so extracts time constants of 256 ps for electrons and 767 ps for holes, as shown in Fig. 4.11C. However, this approach treats the electron and hole concentrations as non-interacting, and a detailed coupled electron-hole transport model incorporating their Coulombic interactions is needed for a rigorous analysis. A recent SUEM study suggests that vertical photocarrier transport driven by a surface field can also lead to fast lateral expansion of the SUEM contrast [120]. In contrast, the lack of contrast saturation at high optical fluences in this study suggests that the vertical transport does not play a significant role here. In addition, the vertical transport picture cannot explain the complex contrast features we observed at higher fluences.

4.3 Conclusions

This study reveals that BAs has excellent photocarrier transport properties, in addition to its high thermal conductivity. SUEM was used to determine that the hot carrier lifetime in BAs is significantly longer than that observed in other semiconductors like silicon. The prolonged hot carrier transport can be an attractive feature for photovoltaic [223] and photocatalytic applications [224]. These unusual properties are attributed to its unique electron and phonon band structures, especially the large acoustic-optical phonon frequency gap. The combination of desirable optoelectronic and thermal properties of BAs renders it an exciting semiconducting material. The potential of SUEM as an emerging tool to directly visualize photocarrier dynamics in samples that are oth-

erwise difficult to characterize with conventional methods is also demonstrated.

Chapter 5

Excited Carrier Transport in Mott Insulator α-$RuCl_3$

5.1 Background

For an electron in a one-dimensional periodic potential, an energy band $\varepsilon(k) = -2tcos(ka)$ can be derived using a tight-binding model, where a is the interatomic distance, k is the wavevector, and t is a hopping term representing the overlap of adjacent orbitals. In this framework, no interaction between electrons is taken into account, and the electrons are approximated as nearly free save for their modulation by the periodic potential of the crystal. This band theory dictates that a half-filled valence band leads to conductive behavior, while a fully filled band results in an insulator. Conventional band insulators are adequately described by this framework in which only single-particle physics are considered.

In 1937, de Boer and Verwey reported that many transition metal oxides, such as

NiO, exhibit insulating behavior despite having partially filled $3d$ and $4d$ orbitals, which should result in a conductive material [239]. Nevill Mott and Rudolf Peierls posited that this behavior could be explained by including Coulombic interactions between electrons [240]. Mott later proposed a model for the insulating behavior of NiO [241]. When neglecting electron-electron interactions, the only relevant length scale to consider is the lattice spacing a. However, introducing electron-electron interactions also introduces a corresponding length scale. Mott then argued that $a \ll l_{e-e}$ results in conductive behavior, while $a \gg l_{e-e}$ produces an insulator, as in NiO. This class of materials are known as Mott insulators.

In a tight-binding framework, the formation of the energy gap can be generalized as a competition between the Coulombic potential U between electrons and hopping between electrons at adjacent sites

$$E_g = U - 2zt \tag{5.1}$$

where z is the number of nearest-neighbor atoms. In a Mott insulator, the Coulomb potential U is large and thus the strong repulsion between carriers creates an energy gap by impeding their flow. In the transition metal oxides highlighted by de Boer and Verwey (which are, specifically, compounds where the number of d electrons per transition metal is an integer), the d bands are half-filled and thus, should produce metallic behavior. However, the strong Coulombic repulsion U splits this band into two sub-bands known as the upper and lower Hubbard bands, which have a gap equal to $E_g = U - 2zt$. Thus, in a Mott insulator, the valence electrons are localized on the transition metal ions.

Given that the insulating systems arise as a result of the competition between the kinetic energy and Coulombic repulsion, transitions between the insulating state and a

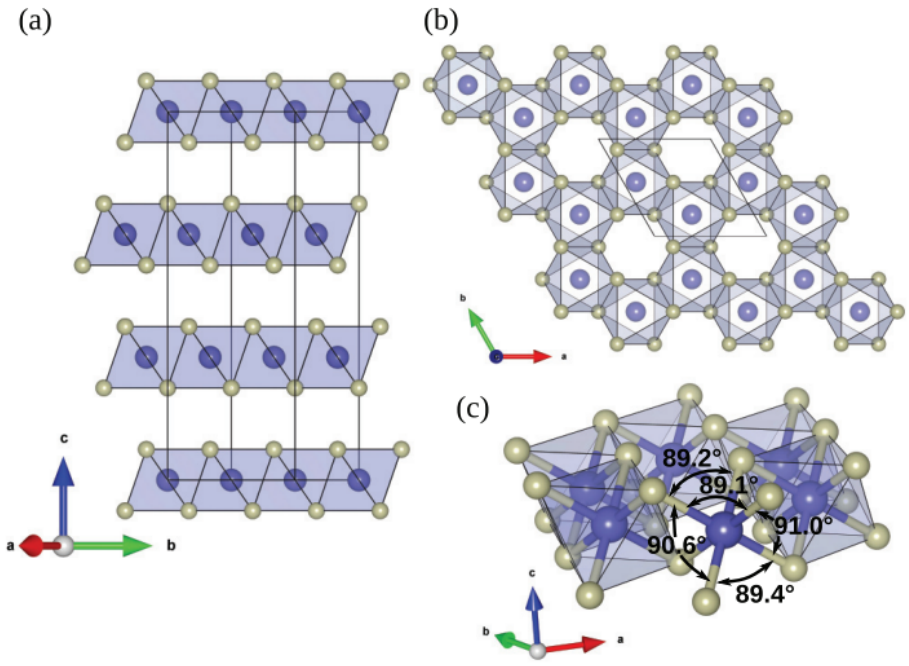

Figure 5.1: The crystal structure of α-$RuCl_3$ flake. a) shows the layered nature of the material. b) shows the honeycomb structure within a single layer. c) shows the octahedra bond angles. Image adapted from [251].

metallic state can be provoked via a satisfactory perturbation [242, 243]. For example, external pressure increases the orbital overlap t [244] and thus the bandwidth $W = 2zt$, and doping to change the number of electrons per transition metal ion per unit cell [245] can both trigger insulator-to-metal transitions in Mott insulating systems.

Additionally, optical excitations have been widely used to trigger and study insulator-to-metal transitions in Mott insulating systems [246–250], making them an interesting platform for imaging using SUEM.

α-$RuCl_3$ is a $4d$ transition-metal halide composed of honeycomb layers made of adjoining $RuCl_6$ octahedra, as shown in Fig. 5.1. Early transport measurements by Binotto et al. of the paramagnetic phase of α-$RuCl_3$ implied that it was an ordinary

semiconductor [252], while later transport measurements suggested that it was a Mott insulator [253]. Pollini performed angle resolved photoemission spectroscopy (ARPES) measurements of α-$RuCl_3$ samples and found that the Ru $4d$ bands were nearly dispersionless through the Brillouin zone, serving as strong evidence of localized electrons.

Plumb et al. later proposed that the insulating state in α-$RuCl_3$ results from a combination of strong correlations and spin-orbit coupling (SOC) [251]. They found that simply incorporating the effect of strong correlations could not sufficiently reproduce the observed insulating state. However, incorporating the strong SOC in the $4d$ electronic system, which they observed with x-ray absorption spectroscopy measurements, reproduces the observed energy gap.

The combination of an insulating state and a honeycomb lattice of strong spin-orbit coupled transition metal ions have been identified as potential candidates for actualizing Kitaev quantum spin liquids (KQSLs) [254, 255]. KQSLs have been the target of energetic research as the Kitaev model predicts that they host non-Abelian anyons which have significant implications for realizing fault-tolerant quantum computing [256, 257]. As a result, α-$RuCl_3$ has been studied extensively in pursuit of this KQSL state [255, 258–261].

These rich physics, including predictions of optically driven magnetic [262] and insulator-to-metal transitions [263], make α-$RuCl_3$ a particularly interesting material to probe with SUEM.

5.2 SUEM Experiments

The α-$RuCl_3$ samples used in this experiment were provided by the Burch group at Boston College. The samples were made via exfoliating off of bulk crystals using Nitto tape and then deposited onto either Si/SiO_2 or Au coated Si substrates. Fig. 5.2 shows two of the representative samples used in this study. The samples were annealed at 180°C for 8 hours under a N_2 purge, using a method similar to what was reported in [264]. SUEM experiments that were attempted before performing the annealing procedure produced images that did not contain any obvious contrast.

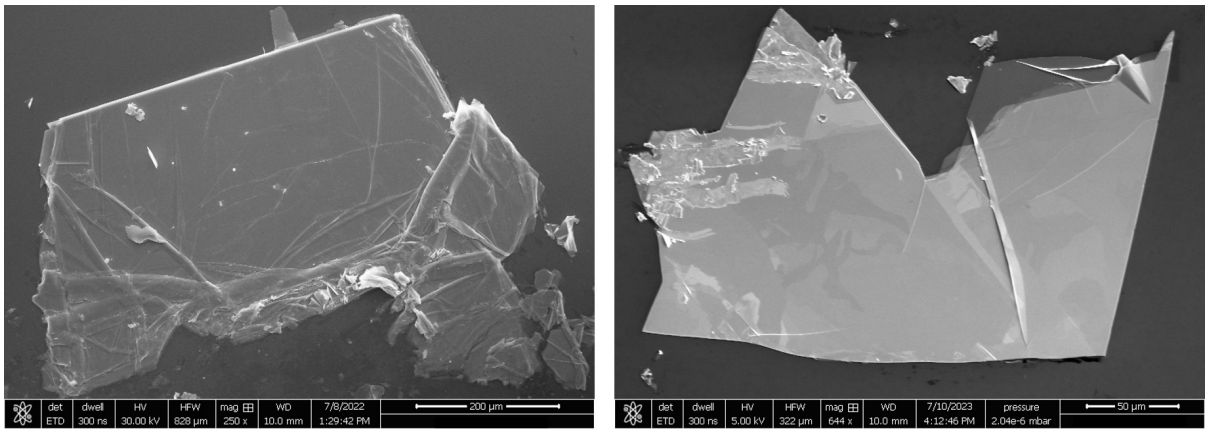

Figure 5.2: **SEM Images of Representative α-$RuCl_3$ Samples.** SEM images of representative α-$RuCl_3$ samples used in SUEM measurements. The left flake was exfoliated onto Au coated Si substrates, while the right flake is on an Si/SiO_2 substrate. Samples were provided by the Burch group at Boston College.

Fig. 5.3 shows representative SUEM images taken on a α-$RuCl_3$ flake on an Si/SiO_2 substrate using a pump fluence of 30 $\mu J/cm^2$. Each image is a contrast image that is obtained by subtracting a reference image that is taken at a far negative time, and thus, the contrast in the images is representative of the change in SE emission from the sample surface as a result of photoexcitation. The lack of contrast at -60 ps indicates that the 200 ns interval between pump pulses is sufficiently long to allow the sample to equilibrate between pumping events. After time zero, bright contrast emerges from the

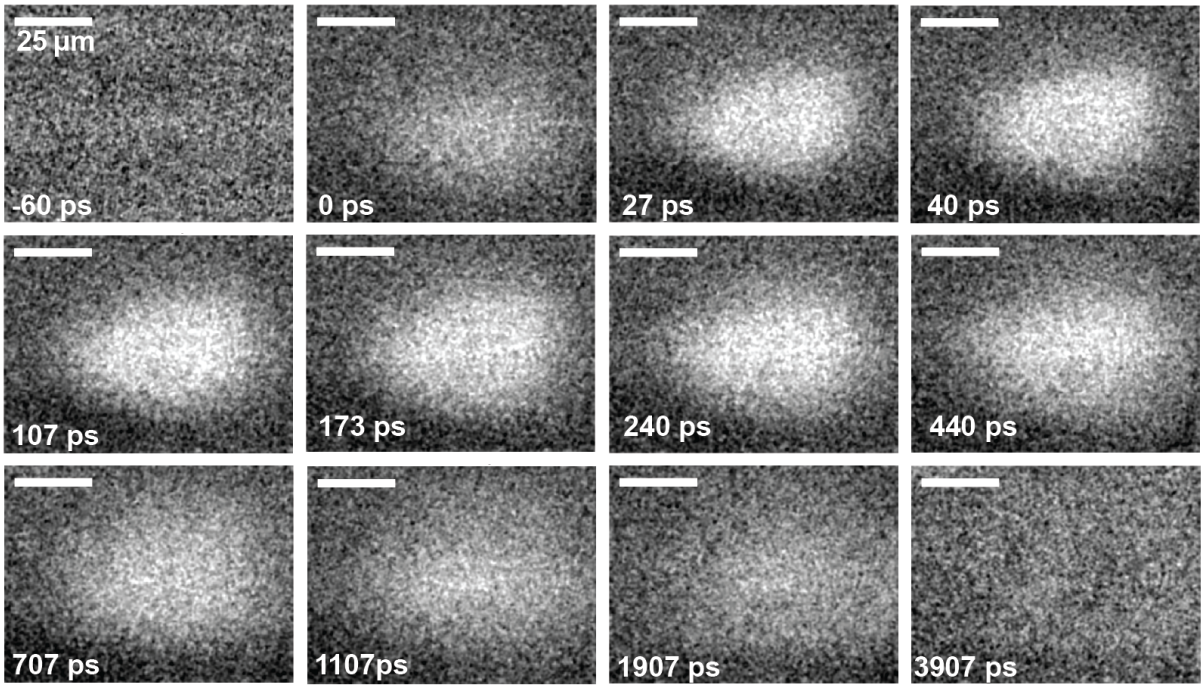

Figure 5.3: **Low Fluence Measurements of α-$RuCl_3$.** SUEM difference images taken on α-$RuCl_3$ flake. A pump fluence of 30 μJ/cm^2 was used for this measurement.

pump-illuminated region indicating that SE emission from the area has increased. This is due to the presence of excited photocarriers, which both increase the average energy of electrons [26] and modulate the surface electrostatic potential [132], providing two channels for generating SE contrast. As such, the contrast present in the SUEM images is assumed to correlate with the distribution of carriers near the sample surface.

In the low fluence SUEM images shown in Fig. 5.3, contrast emerges after time zero and stabilizes after 27 ps. For the next few hundred picoseconds a minimal amount of diffusion can be observed. After around 1 nanosecond, the contrast level has decreased significantly, and after 4 nanoseconds, the system has completely relaxed.

Selected images from a separate experiment using a fluence of 400 μJ/cm^2 are shown in Fig. 5.4. The sample response is clearly qualitatively different from the low

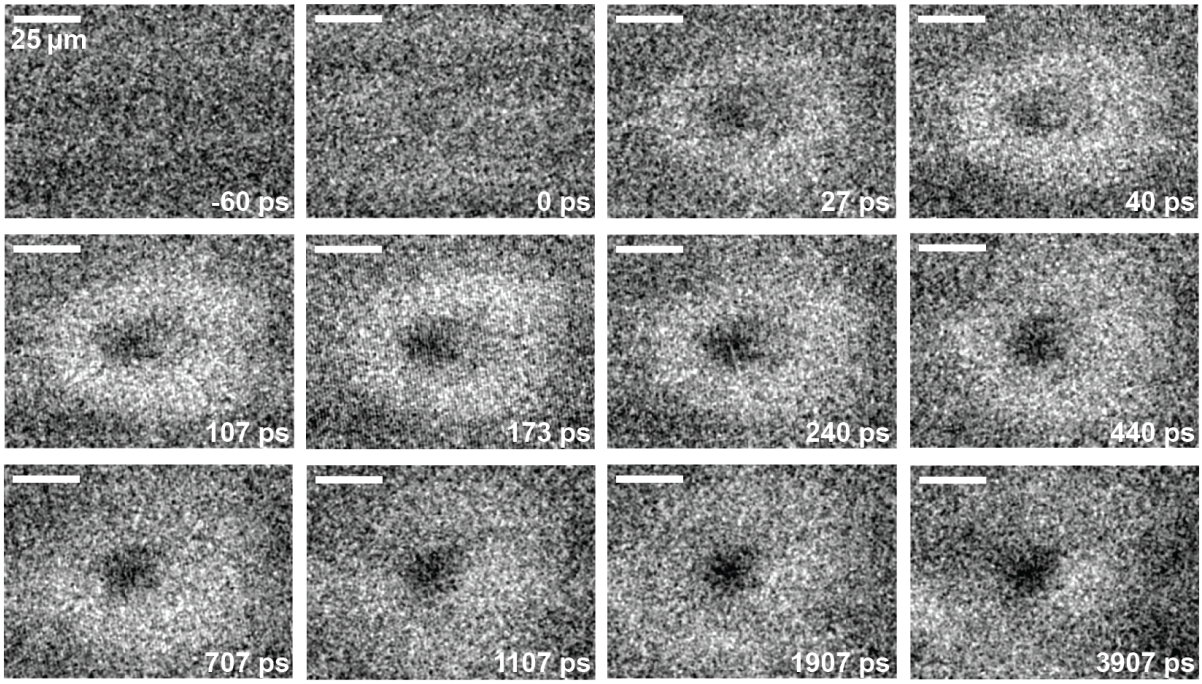

Figure 5.4: **High Fluence Measurements of α-$RuCl_3$.** SUEM difference images taken on α-$RuCl_3$ flake. A pump fluence of 400 $\mu J/cm^2$ was used for this measurement. The presence of non-Gaussian contrast indicates that the sample's response to photoexcitation is nonlinear.

fluence measurements shown in Fig. 5.3. No contrast is visible at negative times, once again indicating that the sample is adequately relaxing between pump-probe events. After a few ps, instead of observing a Gaussian region of bright contrast, a ring of bright contrast is present with a central area of dark contrast. The area of bright contrast expands slightly over a few hundred picoseconds before relaxing on a timescale roughly similar to the low fluence measurements. However, the region of dark contrast persists for the full 4 nanoseconds that are accessible to the experiment.

Additional SUEM image series are shown in Appendix C for intermediate fluences between 30 and 400 $\mu J/cm^2$. This corresponds to excited carrier concentrations on the order of 10^{18} to 10^{18} cm^{-3} or up to $\approx$0.012 electrons per unit cell, as shown in Appendix C in Fig. C.1 and Fig. C.2. While there is some deviation in the observed image contrast

due to some variation in absorption between different locations on the different samples, two general observations can be made from the image series: 1) in general the overall signal level is observed to decrease with increasing fluence, and 2) the magnitude of the dip in the center of the pump-illuminated region also increases with fluence. Therefore, at intermediate fluences between 30 and 400μJ/cm^2 this feature begins to manifest first as a small decrease in contrast, while remaining positive in magnitude. At higher fluences, the center region becomes dark, indicating that SE emission is becoming suppressed in the region of the sample experiencing the greatest instantaneous fluence.

In order to capture the emergence of this non-linear response, a series of SUEM experiments was performed at several different fluences with selected time points being shown in Fig. 5.5. For fluences below 30 μJ/cm^2, the observed contrast is universally bright. For the first few 10s of ps, fast diffusion is observed, after which the spatial expansion of the bright contrast is much slower. Starting with a fluence of 40 μJ/cm^2, a decrease in contrast is observed in the center of the region of bright contrast. This dip is not visible at 7 ps, but becomes quite distinct after a few 10s of ps. As the fluence is increased, the magnitude of the decrease in contrast becomes more apparent, and at 80 μJ/cm^2, the decrease in contrast is visible 20 ps after time zero.

This series of measurements was performed on the same location on one α-$RuCl_3$ sample in order to minimize the effects of any variation in absorption. The different fluences were also measured in random order. The difference images shown are treated with a lowpass filter, and then plotted in grayscale such that the average value of a background pixel (outside of the pump-illuminated region) is 0.5. The image contrast is then stretched to set the value of the brightest pixel across all of the datasets to 1, and the darkest pixel to 0. This facilitates the easy comparison of the signal level across different datasets.

One potentially trivial explanation for the observed contrast is photo-bleaching or some laser induced damage of the α-$RuCl_3$ samples. In order to exclude this possibility, a series of measurements were performed at alternating low and high fluences, shown in Fig. 5.6. and Fig. 5.7. The measurements were performed in the order they are shown in the figures and the same processing procedure that was used in the construction of Fig. 5.5 is used here, meaning the contrast level in the different fluence measurements can be directly compared.

The first series shown in Fig. 5.6 is from a measurement using a pump fluence of 10 $\mu J/cm^2$. Uniform bright contrast is observed, along with minimal diffusion. The second series shows images from a measurement using a fluence of 100 $\mu J/cm^2$. It should be noted that in contrast to the image series shown in Fig. 5.5, no decrease in contrast in the center of the bright region is observed at this fluence, while previously the feature emerged at a fluence between 30 and 40 $\mu J/cm^2$. This is potentially due to differences in absorption between the two regions of the sample. The final two series in Fig. 5.6 are from measurements using 10 and 200 $\mu J/cm^2$. The third series shows uniform bright contrast, as expected for the low fluence, while the fourth set shows an obvious decrease in contrast at the center of the pump-illuminated region.

The first series shown in Fig. 5.7 is performed at 10 $\mu J/cm^2$, and the expected low fluence behavior is retrieved after the sample had previously been excited into the non-linear response regime. This procedure is repeated again, with the next two series showing images from measurements taken at 300 and 10 $\mu J/cm^2$, respectively. The 300 $\mu J/cm^2$ data set once again shows a decrease in contrast in the center of pump-illuminated region. The signal level in this series is clearly lower than in the previous 10 $\mu J/cm^2$ measurement. In comparison with the 200 $\mu J/cm^2$ series shown in Fig. 5.6, the signal level in the 300 $\mu J/cm^2$ is clearly lower overall, and the contrast in the center

of the image is darker relative to the rest of the image. The subsequent 10 $\mu J/cm^2$ measurement once again recovers the expected low fluence response. The final two series were taken at 150 and 100 $\mu J/cm^2$ respectively. The 150 $\mu J/cm^2$ measurement shows a decrease in contrast at the center, while the 100 $\mu J/cm^2$ series looks very similar to the one shown in Fig. 5.6 taken at the same fluence.

5.3 Crossover Fluence and Sample Damage

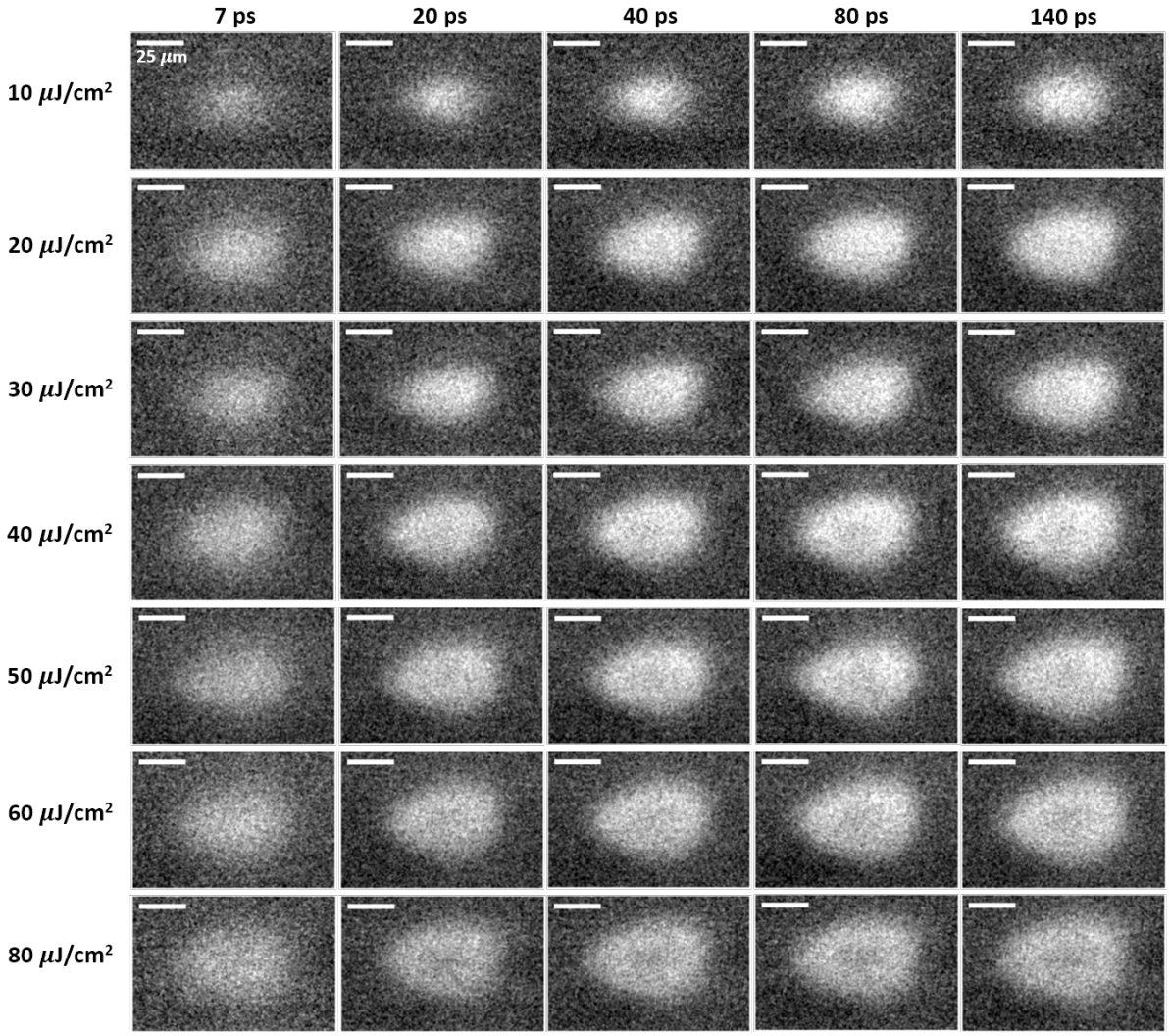

Figure 5.5: **Observing crossover fluence on α-$RuCl_3$.** SUEM difference images taken on α-$RuCl_3$ flake at several different fluences for a few selected time points. The non-linear response at the center of the pump-illuminated area emerges at fluences greater than 40 $\mu J/cm^2$. The presence of non-Gaussian contrast indicates that the sample's response to photoexcitation is nonlinear.

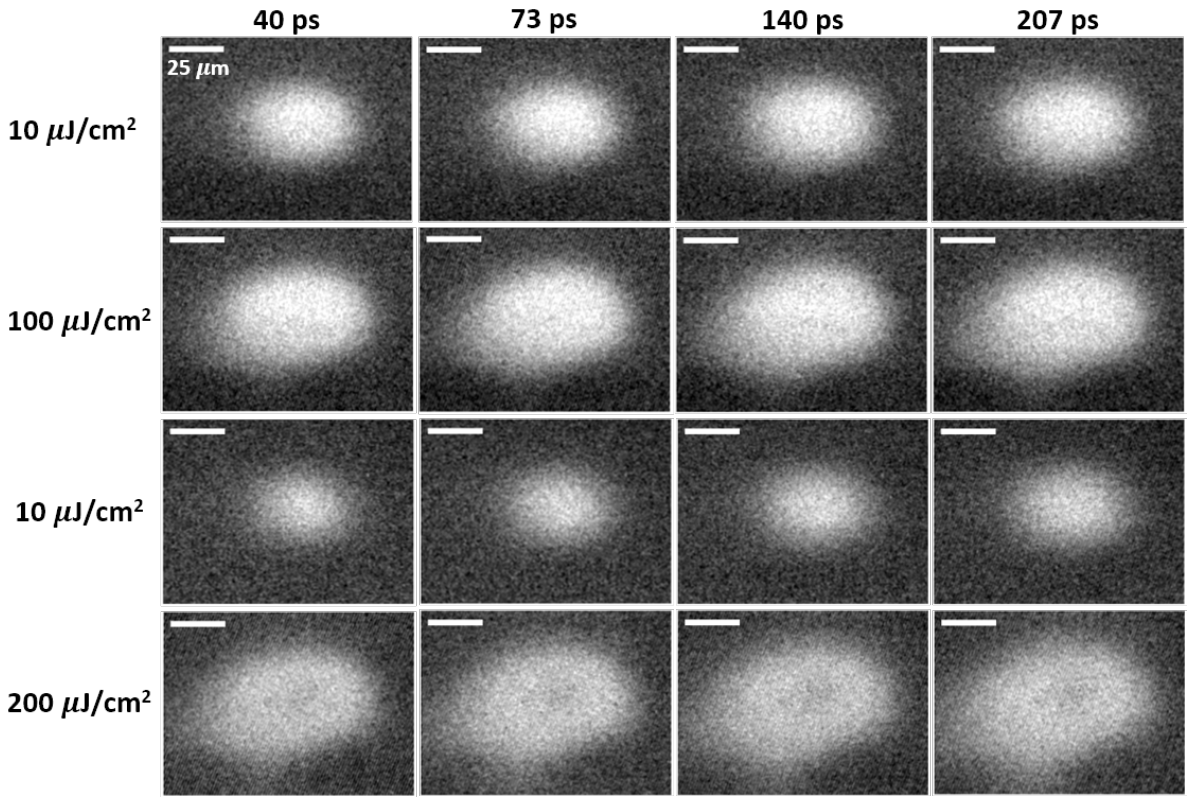

Figure 5.6: **Sample damage test on α-$RuCl_3$.** SUEM difference images taken on α-$RuCl_3$ flake at several different fluences for a few selected time points. The measurements were performed in the order they are shown, and on the same spot on the sample. The linear response is recovered after each subsequent high fluence measurement, showing that the sample is not being damaged. For this location on the sample, the critical fluence at which the non-linear response emerges is between 100 and 150 μJ/cm^2. The other measurements in this dataset are shown in 5.7.

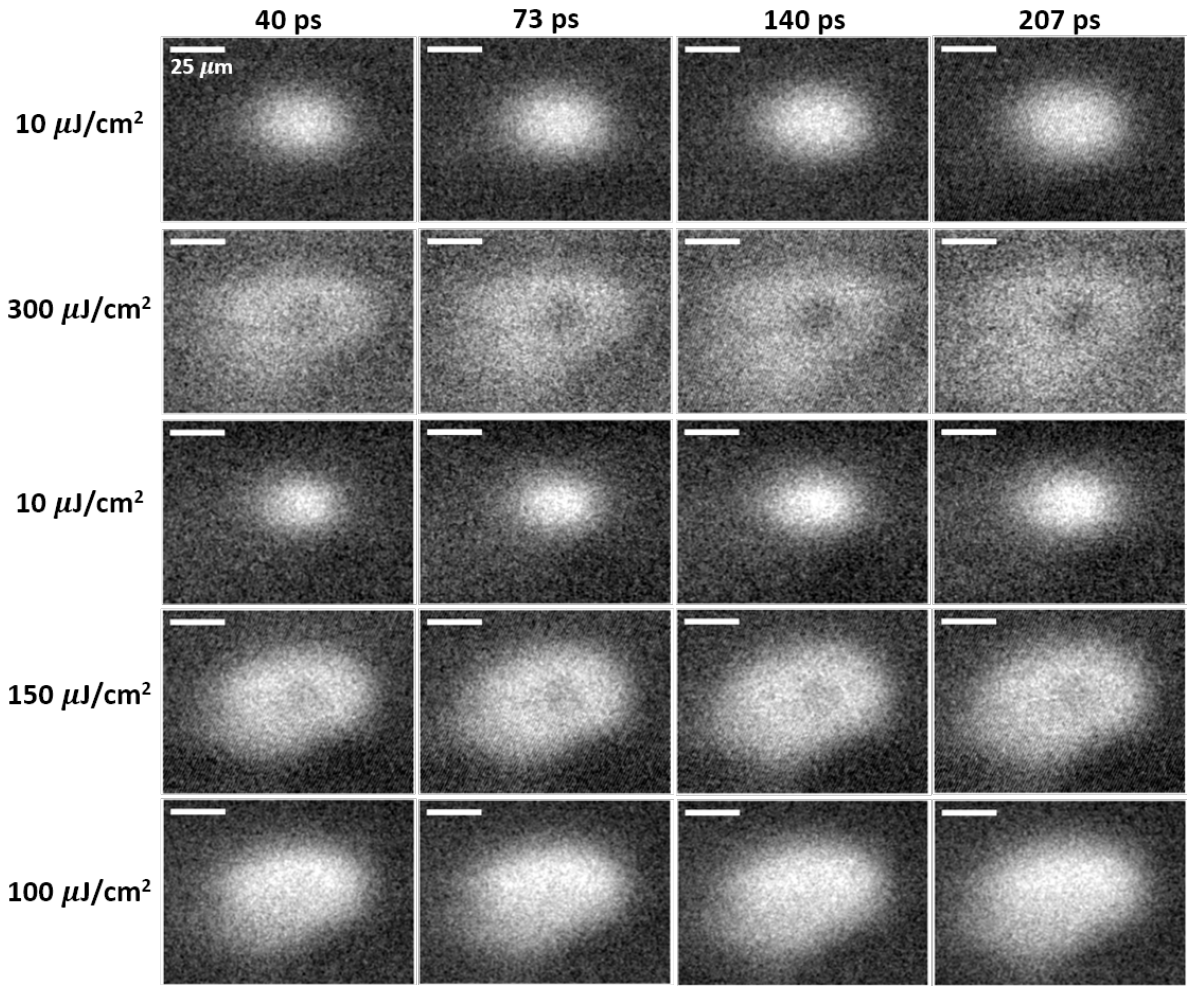

Figure 5.7: **Sample damage test on α-$RuCl_3$.** SUEM difference images taken on α-$RuCl_3$ flake at several different fluences for a few selected time points. The measurements were performed in the order they are shown, and on the same spot on the sample. The linear response is recovered after each subsequent high fluence measurement, showing that the sample is not being damaged. For this location on the sample, the critical fluence at which the non-linear response emerges is between 100 and 150 μJ/cm^2. The other measurements in this dataset are shown in 5.6.

5.4 Analysis and Discussion

At low fluences, the datasets producing uniform bright contrast can be treated using the procedure described in Chapter 4. To briefly summarize, the diffusion process

of generated photocarriers is governed by:

$$\frac{\partial n}{\partial t} = D(t)\left[\frac{1}{r}\frac{\partial}{\partial r}\left(r\frac{\partial n}{\partial r}\right) + \frac{\partial^2 n}{\partial x^2}\right] \tag{5.2}$$

where n is the density of photocarriers, r is the radial distance from the center of the excited region, z is the depth into the sample surface, and $D(t)$ is a time-dependent effective diffusivity which is used to capture the cooling process of the high energy photocarriers. Assuming the initial photocarrier contribution is Gaussian and by omitting the z- direction term, the above equation can be solved analytically to yield:

$$R(t)^2 - R_0^2 = 4(D_i - D_0)\tau(1 - \exp\left(\frac{-t}{\tau}\right) + 4D_0 t \tag{5.3}$$

where $R(t)$ is the observed radius of the carrier distribution, D_i is the initial diffusivity, D_0 is the equilibrium diffusivity, and τ is the hot carrier lifetime. Figure 5.8 shows the expansion of the radius in 30 and 40 μJ/cm^2 measurements as well as the corresponding model fits. We extract values of τ of ~900 and ~2,200 ps for the 30 and 40 μJ/cm^2 measurements. This value is markedly greater than what has been observed in BAs and other semiconductors as been reported previously [127, 156, 265]. On the other hand, the extracted values for the initial diffusivity D_i are on the order of ~2,000 cm^2/s, roughly an order of magnitude lower than what has been measured.

Once the decrease in contrast emerges, characterizing the spatial dynamics of the observable contrast becomes challenging. Similar to the case described in Chapter 4, if we assume that the complex feature results from contributions from separate populations of carriers, then the spatio-temporal evolution of the image contrast can be described by Eqn. 4.14, where one term describes the evolution of carriers producing bright contrast while the other describes the dark contrast. However, as in the previously described case,

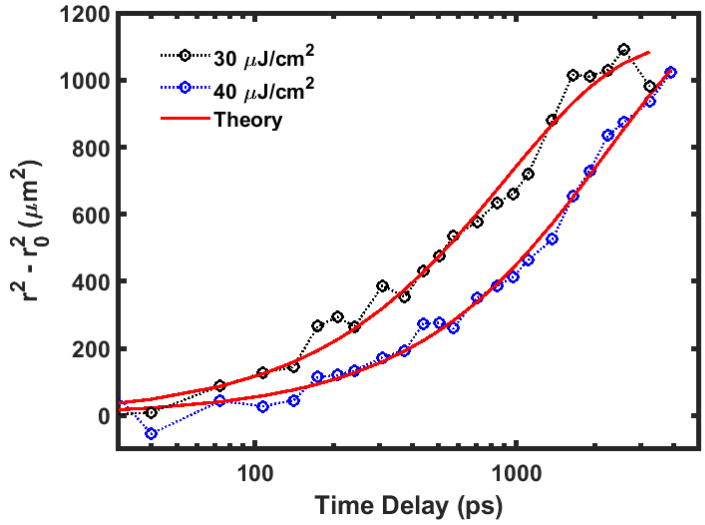

Figure 5.8: This figure shows the rate of expansion of the radius of the carrier distributions in α-$RuCl_3$ when excited using low fluences. The red curves correspond to fits using Eqn. 5.3.

the complex nature of the images produces an insensitive fitting procedure. An example of this is provided in Figs. C.14 and C.15.

Another approach involves monitoring the change in intensity in the SUEM images in different regions of interest. Figure 5.9A,B shows the evolution of the contrast shown in Fig. 5.4 as well as several other data sets shown in Appendix C. The measurements span fluences ranging from 50-400 μJ/cm^2. The left figure shows the change in contrast for the center region, while the right tracks the brightest region on the shoulder of the pump spot. Qualitatively, two trends are clear. As observed, the signal level in the center of the pump spot is lower than on the edge, and the overall signal level decreases as the pumping fluence increases.

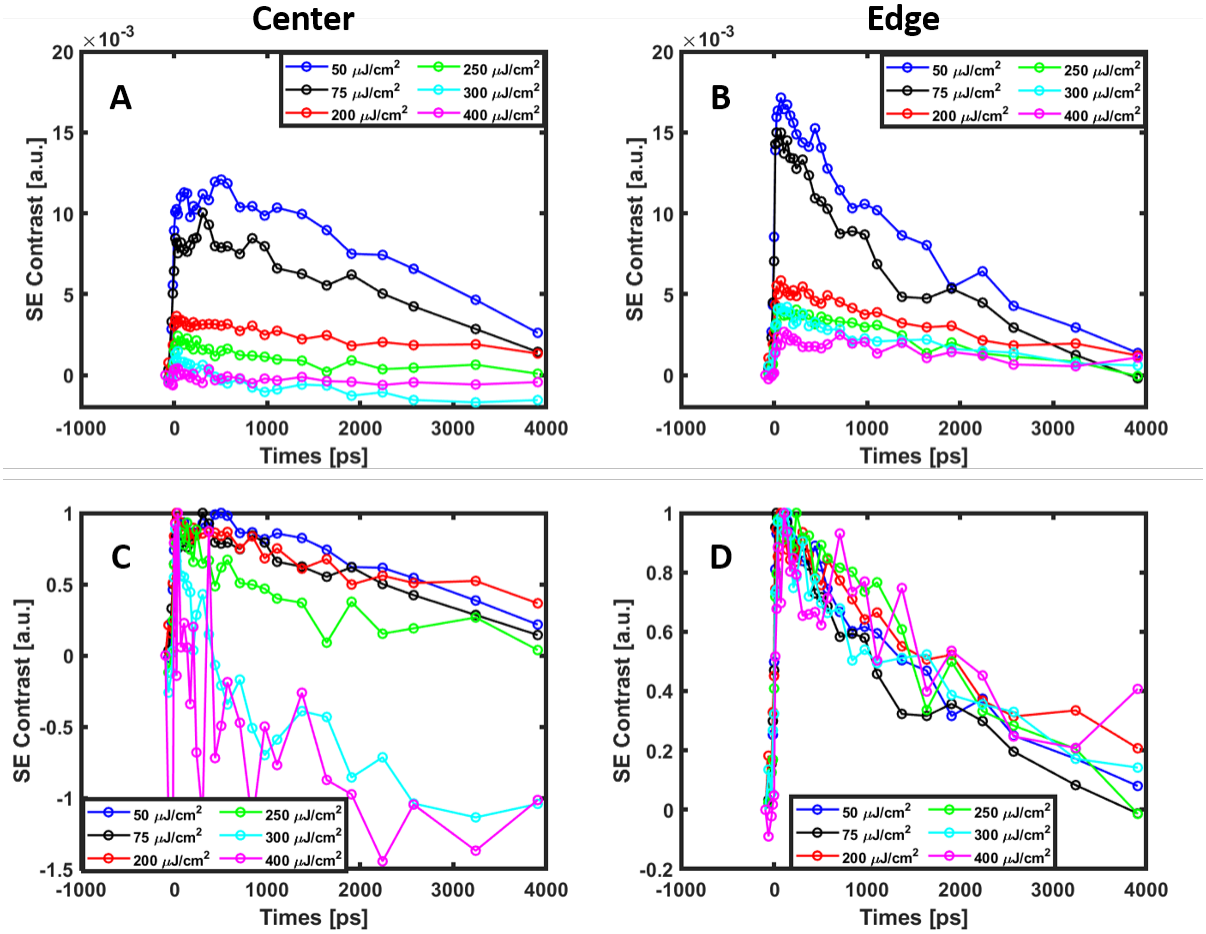

Figure 5.9: a) shows the average change in intensity per pixel over time in the center region for a range of fluences. The signal level clearly decreases as the pumping fluence increases. b) shows the change in intensity in the edge region. The overall signal level in this region is greater than in the center of the pump spot. c) and d) present normalized versions of a) and b).

Panels C and D show the normalized change in contrast for the considered fluences in order to better compare changes in relaxation at different fluences. Panel C indicates that there is no obvious change in relaxation dynamics at low fluences, but at high fluences, the behavior is obviously different. At 250 μJ/cm^2, the contrast in the center decays quicker than at lower fluences, while at 300 and 400 μJ/cm^2, the contrast becomes persistently negative. Curiously, the contrast on the edge of the pump spot does not show

any change in relaxation dynamics as a function of fluence.

Figure 5.10 shows the results of applying this methodology to the datasets shown in Fig. 5.5. Similar to the previous case, and as can be observed, the contrast in the center of the pump region is lower than on the edge, and once again the overall signal level decreases as the fluence is increased. However, there is no obvious change in relaxation dynamics when traversing across the crossover fluence, as can be seen in Fig. C.4.

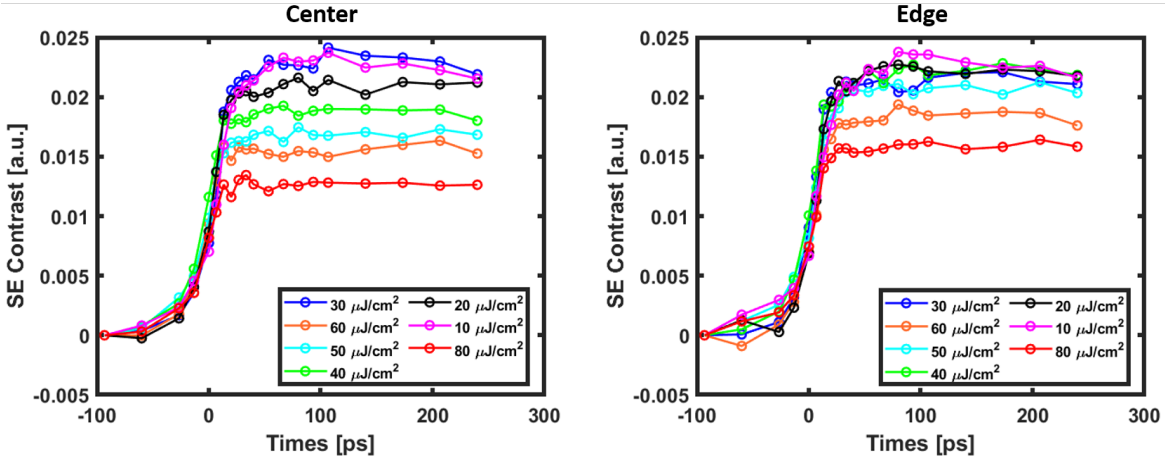

Figure 5.10: The left figure shows the change in contrast per pixel over time in the center region of the pump spot, while the right shows the change in contrast in the brightest region on the edge. Once again, the contrast is brightest on the edge, and the overall signal level decreases with increasing fluence. The normalized figures are shown in Appendix C in Fig. C.4 and do not indicate any change in relaxation dynamics at these fluences.

In Mott insulators, excited carriers can be described as negative doublons, corresponding to doubly occupied sites, and positive holons, corresponding to unoccupied sites. There are theoretical predictions that the relaxation timescales for doublons in Mott insulators increases rapidly when $U \gg W$ due to a thermalization bottleneck [266–268]. We can estimate the observed relaxation time in our measurements by fitting the decay in bright contrast to $\propto exp(-t/\tau_{rel})$. Sample fits for measurements conducted using fluences of 30 and 100 μJ/cm^2 are shown in Fig. C.6. The extracted relaxation times for

these two measurements are τ_{rel}=2.27 $\pm$ 0.26 ns and τ_{rel}=2.03 $\pm$ 0.15 ns respectively. As shown in Fig. 5.9, the relaxation time does not vary much with increasing fluence. Given the large U in α-$RuCl_3$, the long lifetime observed in the low fluence measurements seems reasonable.

These doublons and holons can also form Mott-Hubbard excitons (MHEs), which are analogous to excitons in conventional semiconductors [269]. Nevola et al. performed time-resolved two-photon photoemission spectroscopy and transient reflection spectroscopy measurements on α-$RuCl_3$ [270]. They observed an initial fast relaxation of carriers on the order of 200 fs. They then observe a very long lived state, whose lifetime they are unable to resolve, but is approximated as <500 ps. They describe the initial fast relaxation to a thermalization of doublons in the upper Hubbard band to lower energy states. They then posit that these carriers form MHEs which experience another rapid relaxation, perhaps with phonon or magnon populations, after which the MHE population persists for the observed long lifetimes. The MHE lifetimes are also in general agreement with some theoretical predictions for MHEs [271,272]. Similar MHE lifetimes have been observed in $LaVO_3$ [273].

The observed contrast in the high fluence images has some qualitative analogues in the existing SUEM literature. The presence of bright and dark contrast in BAs described in Chapter 4 is attributed to the breakdown in ambipolar diffusion, with higher mobility holes diffusing more rapidly than low mobility electrons. Electron-hole separation is observed by Liao et al. in amorphous silicon and is explained by relaxation semiconductor behavior [128]. Neither of these cases satisfactorily explain the observed contrast in α-$RuCl_3$.

Recently, Zhang et al. have reported ab initio simulation results on the laser driven

dynamics in α-$RuCl_3$ [263]. Simulating wavelengths from $\hbar\omega$=0.5×E_{gap} to 1.25×E_{gap} and electric field strengths on the order of 1×10^{12} W/cm^2, they find that ultrashort light pulses generate a significant number of electron-hole pairs, which in turn triggers a collapse in the Hubbard U and produces a transient, ultrafast insulator-to-metal transition. While the photon energy (2.4 eV) and applied electric field ($\sim1\times10^{10}$) used in our system are different than those used in the simulation, the transition offers a promising explanation for the observed results.

The picture we propose is as follows: at low fluences, the number of generated carriers is insufficient to trigger the transition observed by Zhang et al., and the observed contrast and relaxation dynamics are broadly consistent with theoretical and experimental observations of doublons and MHEs in strongly correlated materials [270–272]. At fluences slightly above the observed transition fluence, the local carrier density at the center of the pump is large enough to perturb the Hubbard U and induce some band renormalization. As the fluence increases, a greater proportion of the illuminated area contains a sufficient carrier concentration to trigger renormalization, resulting in the slow accentuation of the dip in contrast visible in Fig 5.5. At very high fluences, such as those shown in Fig. 5.4, the observed response has entered a new regime, perhaps due to a complete collapse in the band gap.

The photodoped insulator-to-metal transition proposed has been observed in other Mott insulating systems such as 1T-TaS_2 [274] and VO_2 [85]. Meanwhile, optically modulated band renormalization has also been proposed as a mechanism for the insulator-to-metal transition in VO_2 [275] and NiO [276, 277], and has also been observed in La_2CuO4 [278]. However, it should be noted that no metallic transition was observed in UO_2 [279], which has a comparable Hubbard U to α-$RuCl_3$.

In conclusion, we use SUEM to image the spatio-temporal response of α-$RuCl_3$ to photoexcitation. At low fluences, we observe slow, relatively monotonic diffusion of excited carriers that exhibit a very long lifetime, consistent with predictions of slow MHE thermalization in systems with strong U [271, 272], as well as with other optical probing of α-$RuCl_3$ [270]. Above a threshold fluence, we observe the emergence of a decrease in contrast in the most intense region of the pump-excitation. As the fluence increases, the magnitude of the dip in contrast increases, as does its spatial extent. At very high fluences, we observe a contrast inversion and an overall decrease in the SUEM signal level. The fluence dependent dip in contrast is attributed to a carrier concentration dependent modulation of the Hubbard U in α-$RuCl_3$, which causes significant band renormalization and at very high fluences, a collapse of the band gap. This study showcases SUEM's ability to characterize strongly correlated materials, and shows its ability to potentially characterize metastable phases and inhomogenous material responses.

Chapter 6

Conclusion

6.1 Summary

Ultrafast optical spectroscopies and electron microscopy techniques have allowed scientists to observe matter on fundamentally relevant time and length scales. The development of ultrafast pulsed electron probe techniques has served as the next evolution of spectroscopy and microscopy, resulting in techniques with simultaneously ultrafast and ultrashort resolution. SUEM is the latest iteration in this journey, and combines the femtosecond resolution of optical spectroscopies with an SEM platform, allowing for the surface sensitive study of photocarrier dynamics in materials and devices on a nanometer scale.

This thesis documents the construction and development process of SUEM at UCSB, which is currently the only operational system at a US university.

Chapter 3 discusses the operational principles of SUEM, describes the develop-

ment process, and elaborates on some technical challenges encountered. The process of achieving pulsed electron emission is described, and the response of the SEM photocathode to different illumination conditions is detailed.

In Chapter 4, SUEM is used to study photocarrier dynamics in an emerging semiconducting material, BAs. BAs has received a great deal of attention recently due to its ultrahigh thermal conductivity, but its electronic properties have not been well studied. SUEM was used to investigate charge carrier dynamics in BAs, and analysis of SUEM difference images revealed a two-stage diffusion process consisting of an initial fast diffusion lasting a few hundred picoseconds, followed by a slower diffusion regime. A model incorporating a time-dependent carrier diffusivity was developed in order to model the spatial evolution of carriers observed and explain the observed results. The extracted hot carrier lifetime for BAs, around 200 ps, was found to be significantly higher than what has been measured in Si [127]. High fluence SUEM measurements observed the separation of electrons and holes, as evidenced by the presence of bright and dark contrast, corresponding to separate populations of carriers.

In Chapter 5, SUEM is used to image a potential insulator-to-metal transition in α-$RuCl_3$. Once thought to be an ordinary semiconductor, α-$RuCl_3$ is a Mott insulator and host to a variety of exotic physics. SUEM images at low fluence showed uniform bright contrast and very slow carrier diffusion, as expected for a material with strong carrier-carrier interactions. At higher fluences, the material response becomes non-linear, and a decrease in contrast in the center of the pump-illuminated region becomes visible. As the fluence is increased, the magnitude of the change in contrast is observed to increase, and the overall signal level also decreases. First-principles simulations have predicted that α-$RuCl_3$ undergoes an insulator-to-metal phase transition when pumped with ultrashort laser pulses. The photoexcited carriers trigger a collapse in the bandgap and a change

in the mobilities of the excited carriers. The instantaneous electric field produced by the pumping laser pulse is strongest at the beam waist, resulting in a change in contrast originating in the center of the laser spot and increasing in size with fluence.

6.2 Outlook and Future Directions

While this thesis discussed many of the challenges encountered in the development of SUEM, there are many potential instrumentation that can still be pursued. The primary benefit of using the electron probe is the improved spatial resolution, which in theory should be limited by electromagnetic aberrations present in the SEM and space-charge repulsion in the electron pulses. However, the images presented in this thesis are in general probing areas on samples a few 10s of μm wide. This is in large part due to the challenges involved in focusing the pump laser beam into a tight spot on the sample, as a smaller beam waist on the sample requires having a large beam diameter incident on the final focusing lens and/or a short focal length lens. We have been able to move to higher magnifications due to the development of the in-chamber lens holder, but the power of SUEM could be better leveraged by continuing to push spatial resolutions further.

The added spatial dimension greatly increases the acquisition time of SUEM data sets relative to other spectroscopies. When coupled with the inherently low signal to noise ratio of SUEM, experiments of only a few dozen time points can take several hours. The SUEM is also currently quite an unstable system, which is largely understandable due to its novelty, and should continue to improve as general instrumentation advancements are made and institutional knowledge is gained. However, the combination of low signal to noise and system instability, manifesting as current decay and sample drift, make systematic study of sensitive samples extremely challenging. Improvements in signal

acquisition and image construction and processing, perhaps through the implementation of lock-in detection, will be a great boon to future SUEM studies.

While SUEM has great potential as a tool for physics and materials study, the ambiguous nature of the SE emission process makes prediction and quantification of SUEM datasets difficult. Monte Carlo studies of SE emission are generally limited to lower primary electron energies due to poor computational scaling, and while our group has made some advances on characterizing the effect of photoexcitation on the SE emission process [126], a great deal of progress remains to be made in this direction. Additionally, due to the shallow escape depth of SEs, SUEM is a very surface sensitive technique. However, the vacuum levels attained in commercial SEMs ($\sim 10^{-7}$ torr) are quite poor relative to those attained in other surface sensitive techniques like ARPES and MBE ($\sim 10^{-11}$ to 10^{-12} torr). This makes SUEM studies challenging as it becomes difficult to maintain consistent surface conditions from experiment to experiment. While it is impractical to improve upon the current vacuum level, a better understanding of the SE emission process coupled with the integration of surface sensitive characterization techniques like Kelvin probe force microscopy or x-ray photoelectron spectroscopy into the SUEM workflow could help to produce more quantitative SUEM studies.

Appendix A

SUEM Characterization

A.1 Photoemission Characterization

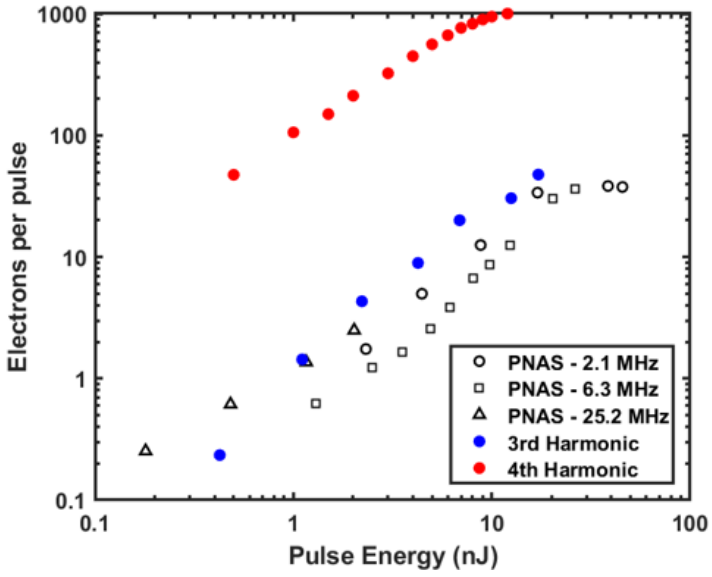

Figure A.1: The number of photoelectrons generated per pulse vs pulse energy are shown for both the third and fourth harmonic. Results from Yang et al. [124] are shown for comparison. The fourth harmonic produces far more electrons per pulse than the third harmonic, likely due to higher fluence.

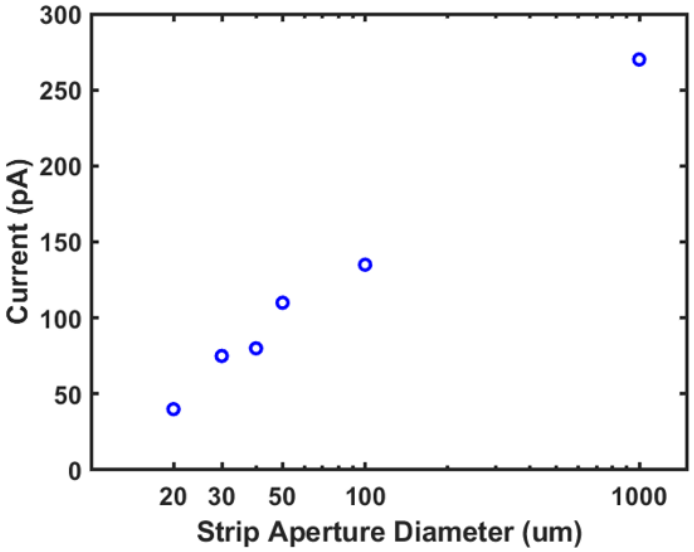

Figure A.2: The photoemission current vs. strip aperture diameter data from Table 3.3 is shown here.

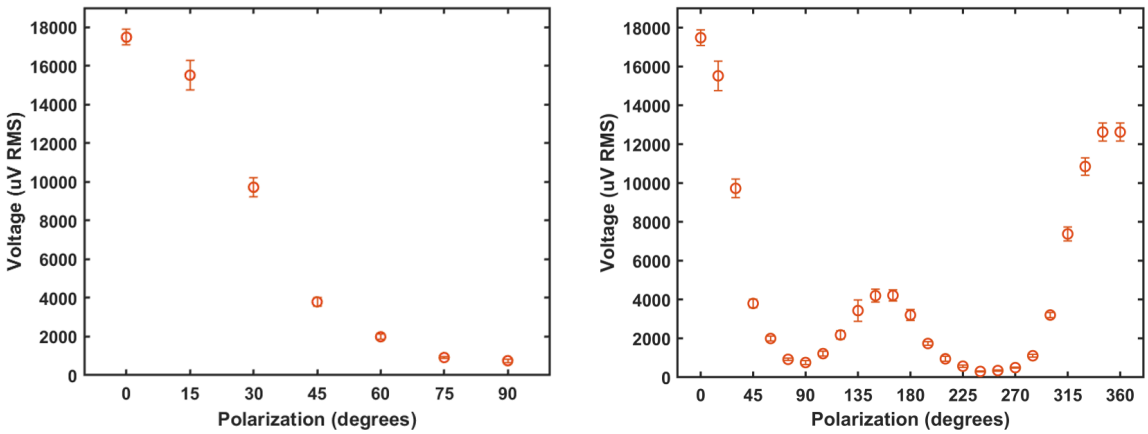

Figure A.3: This figure shows the photoemission magnitude as a function of UV probe polarization. Maximum photoemission occurs when the polarization is oriented parallel to the tip, denoted as zero degrees. The figure on the left is included in the main text. The figure on the right rotates the polarization over a full 360 degrees. The hysteresis observed is attributed to slight refraction by the Glan type polarizer resulting in a slight misalignment of the probe beam on the tip.

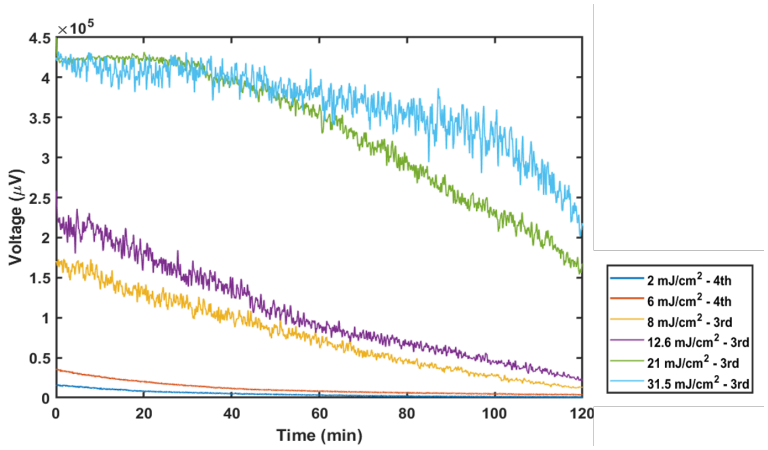

Figure A.4: This figure shows the photoemission stability using the third and fourth harmonic beams for various fluences. In these measurements, the fourth harmonic fluence is much lower than the third harmonic fluence due to differences in the optical paths at the time.

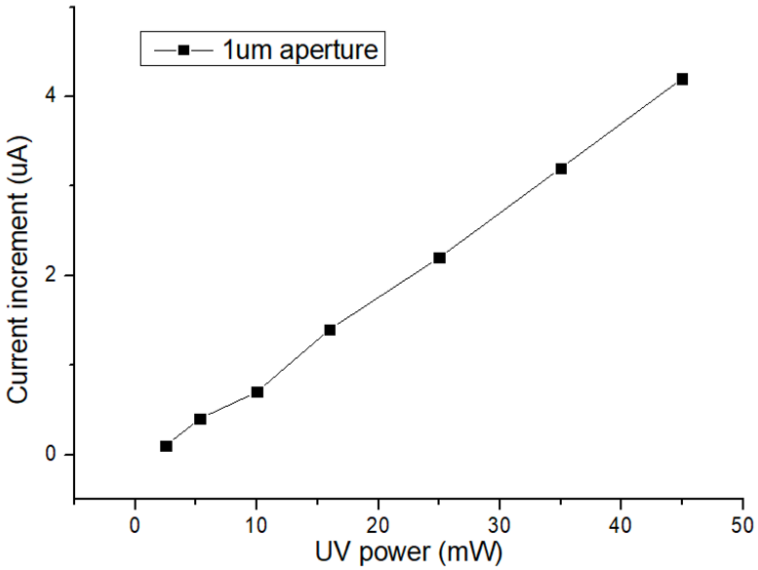

Figure A.5: **Thermal emission vs. UV power measured in the Wehnelt cylinder.** As the power increases, the thermal emission also increases linear. This current is measured by the SEM in the Wehnelt cylinder and thus considers electrons that do not enter the column.

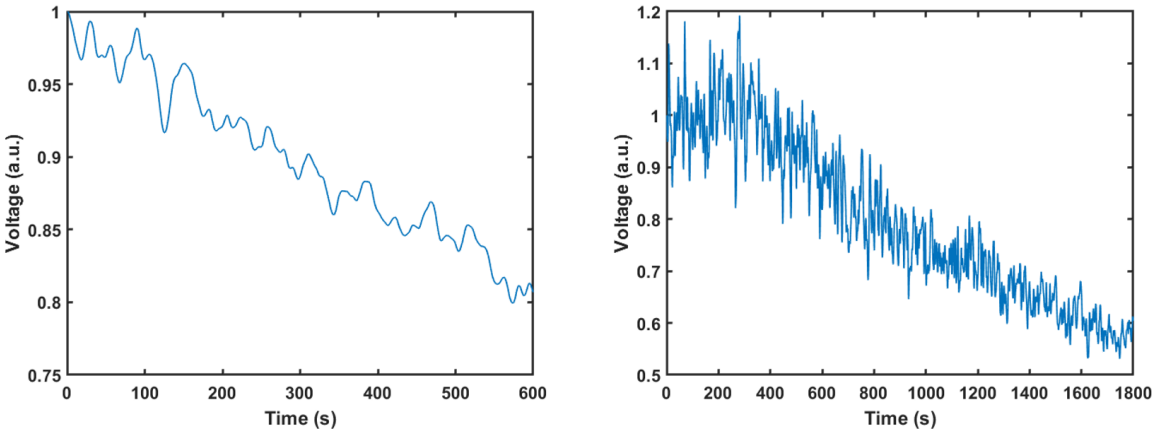

Figure A.6: **Photogenerated thermal emission decay over several hours.** The UV probe beam is modulated using an optical chopper, and the SE signal is recorded using a lock-in amplifier.

Figure A.6 shows the decay of photogenerated thermal emission as measured with a lock-in amplifier. Due to the reduce heating current, the ZrO_x coating recedes up the tip and overall emission is reduced over several hours hours.

A.2 Pump Characterization

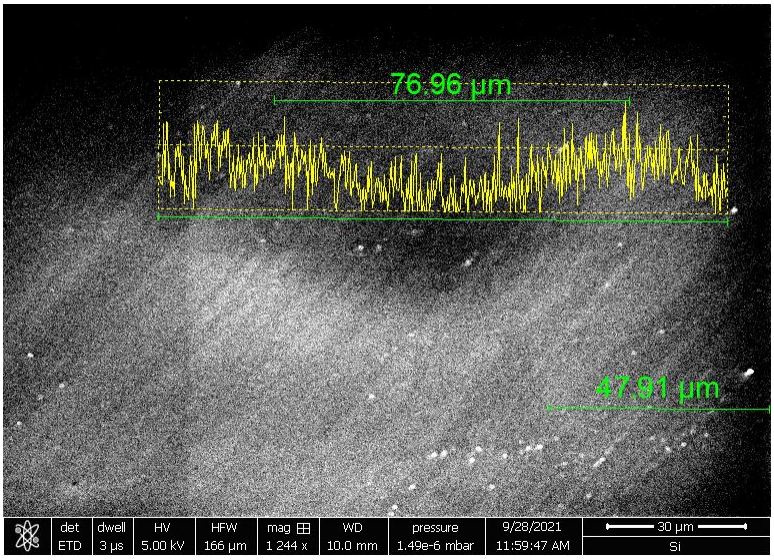

Figure A.7: An SEM image of the pump spot visible on a GaAs sample is shown. The pump here is focused using a lens outside of the chamber.

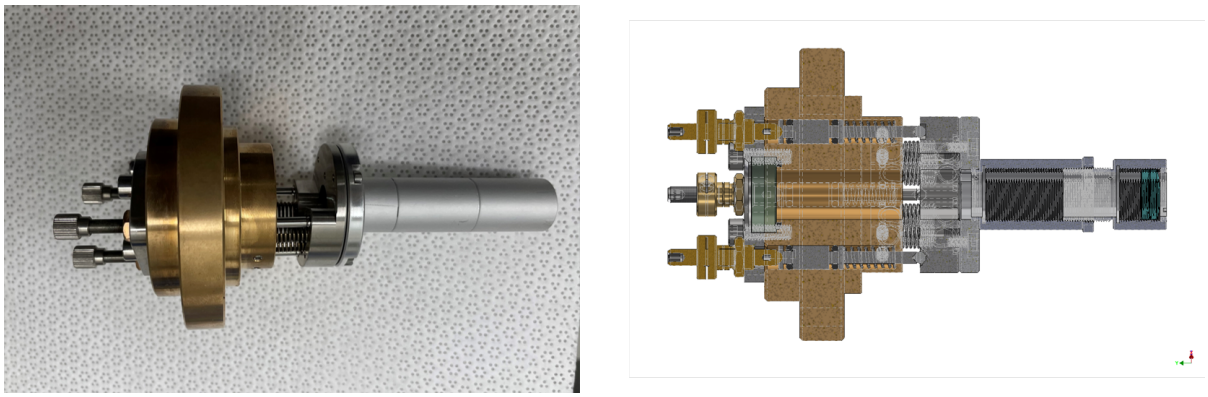

Figure A.8: The left image shows the uninstalled lens holder. The holder is inserted into the access port where the previous optical window was located and is affixed to the breadboard on the SEM. The actuators are located on the outside of the chamber and are able to manipulate the kinematic mount while vacuum is pulled. The holder incorporates standard 1/2 inch diameter lens tubes, allowing for use of different focal length lenses. The right image shows a schematic of the holder.

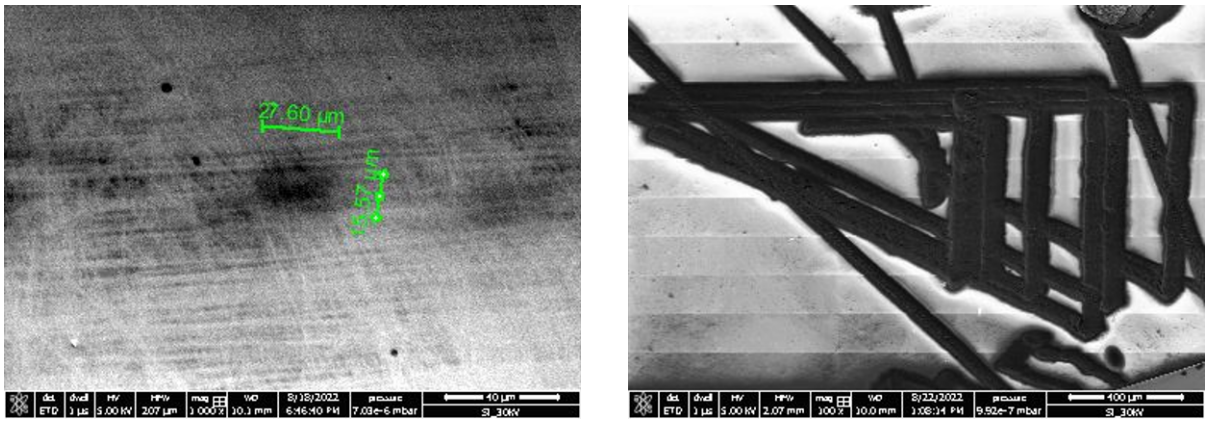

Figure A.9: Left shows the pump spot on GaAs when using a 5 cm focal length lens placed in the in-chamber lens holder, along with a rough approximation of its size. The right shows laser damage on a carbon tape sample. The triangular pattern on the carbon tape on the right is produced by adjusting each of the actuators on the lens holder kinematic mount in series. This translates the mount along the propagation direction of the beam and is used to properly focus the beam on the sample. Carbon tape samples have proven very convenient for pump beam alignment due to their instantaneous response.

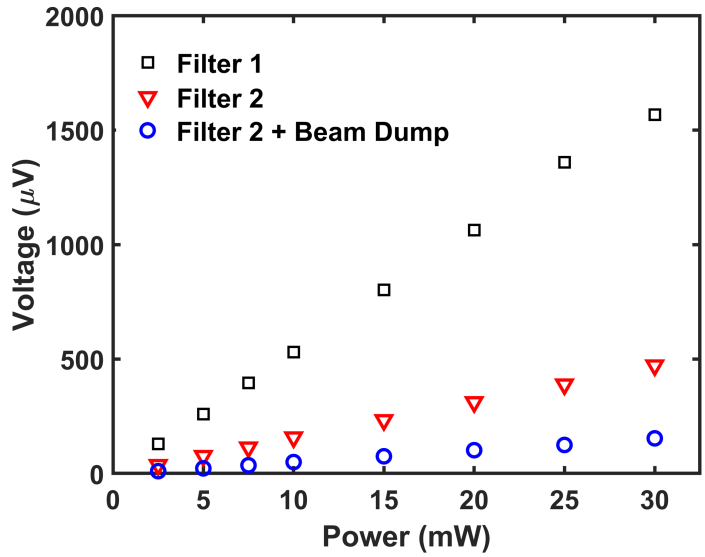

Figure A.10: **Measurement of Pump Light Leakage into ETD** Comparison of pump light leakage for three different filtration schemes.

Appendix B

Extra BAs Experiments

B.1 Sample Characterization

B.1.1 Sample Preparation

Cubic BAs single crystals were synthesized using a chemical vapor transport (CVT) method. First, natural boron (B) (19.9% ^{10}B and 80.1% ^{11}B, ≥99.9% purity, UMC), pure arsenic (As, ≥ 99.99999%, Alfa Aesar), together with appropriate amount of transport agent iodine (I_2, ≥99.9985%, Alfa Aesar), were sealed in a fused quartz tube under vacuum (10^{-4} torr). The sealed quartz tube was then put into a two-zone horizontal tube furnace. All materials were placed at the source end of the sealed quartz tube, which was positioned at the high-temperature zone of 890°C. The other end of the quartz tube was positioned at the low-temperature zone of 790°C. At the source end, I_2 reacted with B to form gaseous species BI and BI_3 and transported to the growth end, and finally reacted with As to form BAs. After three weeks, BAs crystal pieces were obtained from the quartz tube.

B.1.2 XRD Measurements

X-ray diffraction measurement was conducted by a Riguka SmartLab X-ray diffractometer with a Cu K α radiation source. High-quality BAs crystals are usually reddish flakes, with the two largest surfaces usually parallel to each other. For the measurement, the BAs sample was placed on a zero-background holder with one of the largest surfaces attached to the holder. Fig. 4.6C shows the XRD pattern of a BAs sample with 2θ ranging from 20° to 120°. Each peak in this pattern includes two peaks from Kα_1 and Kα_2. The XRD measurement showed that the BAs samples grown by the CVT method are high-quality single crystals, with the preferred orientation of (111).

B.1.3 Raman Measurements

Raman spectra were measured by SpectraPro HRS-300 (Princeton Instruments) using 1,200 g/mm grating. A 532 nm laser was used to excite the sample using a power of 6 mW. Fig. 4.6E shows the Raman spectra of a point on the BAs sample. As has been reported previously [280, 281] BAs has only one phonon that is active in the first-order Raman scattering, as the LO-TO splitting is very small. To improve the resolution of the Raman spectra, the slit was adjusted to a minimum to get the Raman spectra of the sharp LO peak at 705 cm^{-1}. The full width at half maximum (FWHM) of the LO peak has a small value of 5.3 cm^{-1}, which indicates low impurity concentrations.

B.1.4 X-ray Photoelectron Spectroscopy Measurements

The XPS spectra were recorded on a ThermoFisher Escalab Xi^+ XPS Microprobe with a monochromated Al Kα X-ray source. X-ray spot of 400 mm was used because of the crystals' small dimensions. Avantage Data System and CasaXPS software were used

to analyze the spectra. To remove the effect of charge compensation, all binding energies were calibrated to the adventitious C1s peak at 284.8 eV which is from the presence of adsorbed hydrocarbons.

Figure B.1 shows the XPS survey spectra for one of the BAs single crystals samples used in the SUEM measurements, while table B.1 summarizes the data. The high amount of adventitious carbon and oxygen is originating from the carbon tape surrounding the small crystal as the X-ray spot is 400 µm while the crystal dimensions are approximately 300 µm. Figure B.2 shows some high resolution XPS spectra. The sharp B1s peak at 188.84 eV shown in Fig. B.2A indicates the absence of boron oxides and carbides, while B.2B shows the presence of some arsenic oxides on the sample surface.

Element	Peak Binding Energy (eV)	FWHM (eV)	Area (CPS.eV)	Sensitivity Factor	Atomic %
B 1s	188.84	2.08	9,572	0.376	5.31
As 3d	42.48	2.42	45,631	1.674	5.38
C 1s	284.8	3.53	305,248	1.000	66.51
O 1s	532.32	2.82	265,597	2.881	22.81

Table B.1: **XPS Data for BAs Sample Used in SUEM Measurements.** The large C and O atomic ratios were likely due to the carbon tape that was used to mount the sample (the X-ray beam size is slightly larger than the BAs single crystal).

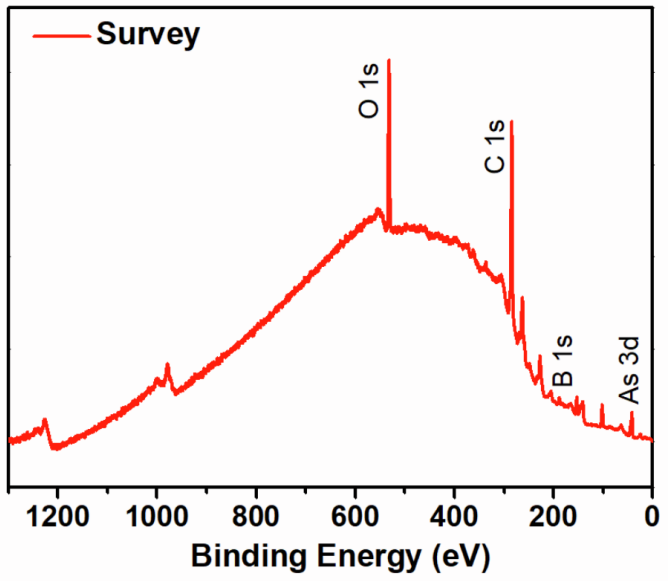

Figure B.1: XPS survey spectra for the same BAs single crystal used in SUEM measurements.

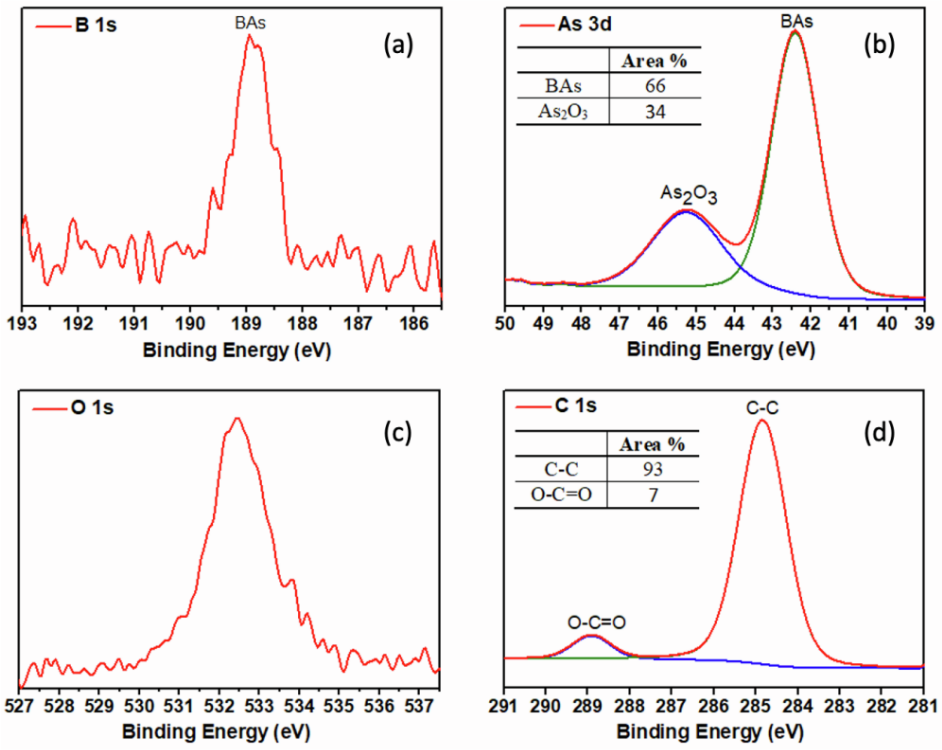

Figure B.2: (a) XPS high resolution scan of the boron 1s state. The dominant B-As bonds with a binding energy of 188.84 eV indicate the absence of boron carbides or oxides. (b) XPS high resolution scan of the arsenic 3d states, indicating coexistence of BAs and arsenic oxide (As_2O_3) on the sample surface. (c) and (d) show the XPS high resolution scan of oxygen and carbon.

B.1.5 Time-resolved Optical Reflectivity Measurements

Time-resolved optical pump–probe reflectivity measurements of BAs single crystals were conducted in ultrahigh vacuum with a base pressure on the order of 10^{-10} torr, to minimize surface oxidation over an extended time and potential effects on the photocarrier dynamics and lifetime. Details of the optical setup have been described previously [282]. Briefly, from a Yb:KGW regeneratively amplified laser system (Pharos-SP, Light Conversion, 170 fs), the fundamental output (1,030 nm, 1.20 eV) and the second harmonic generation (515 nm, 2.41 eV) were used for below-gap reflectivity probing

and above-gap photoexcitation, respectively. Consequently, transient reflectivity changes have free-carrier absorption as the most contribution at the photoinjection density used here, whose temporal evolution provides direct information about the average photocarrier density near the surface in the ensemble measurement. From the 200 μm lateral width of the laser footprint on the specimen, an average fluence of 130 μJ/cm^2 was estimated in the probed region. Ambipolar carrier diffusion into the bulk was then more prominent because of the comparably limited absorption depth of 6 mum at 515 nm and a much larger density gradient along the surface normal direction. With the reflectivity of 0.26, the initial photo-injection density was $4 \times 10^{17} cm^{-3}$. At a laser repetition rate of 1 kHz and a mechanical chopper at 500 Hz, the transient reflectivity from the s-polarized probe beam was measured by a silicon photodiode coupled to a lock-in amplifier.

Figure B.3 shows an experiment using this methodology. The blue curve represents a model in which the photoexcited carriers diffuse with an equilibrium diffusivity, while the red fit includes contributions from photoexcited hot carriers.

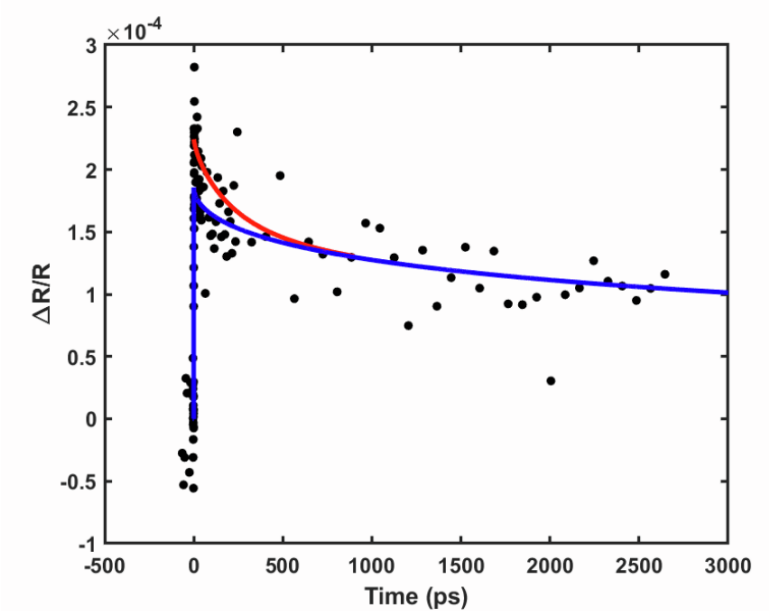

Figure B.3: **Transient Absorption Measurement of BAs Single Crystal** The black dots represent the experimental data. The blue solid line represents a model assuming the photoexcited carriers diffuse away from the sample surface with the equilibrium diffusivity 45 cm^2/s, while the red solid line represents a model taking into account hot photocarrier transport with a time scale of 220 ps as observed in the SUEM measurements.

B.2 Additional BAs SUEM Data Sets

Sample	Optical Fluence ($\mu J/cm^2$)	τ (ps)	Shown in Figure
Flake 1	100	220	Fig. 4.7A and Fig. 4.8A
Flake 1	80	233	Fig. B.5
Flake 1	130	145	Fig. B.6
Flake 2	130	160	Fig. 4.8B and Fig. B.7
Flake 2	80	250	Fig. B.8
Flake 1	235		Fig. 4.11
Flake 2	185		Fig. B.10

Table B.2: **Summary of SUEM Measurements.** The first five datasets were obtained using lower optical fluences, while the last 2 datasets were obtained using higher optical fluences.

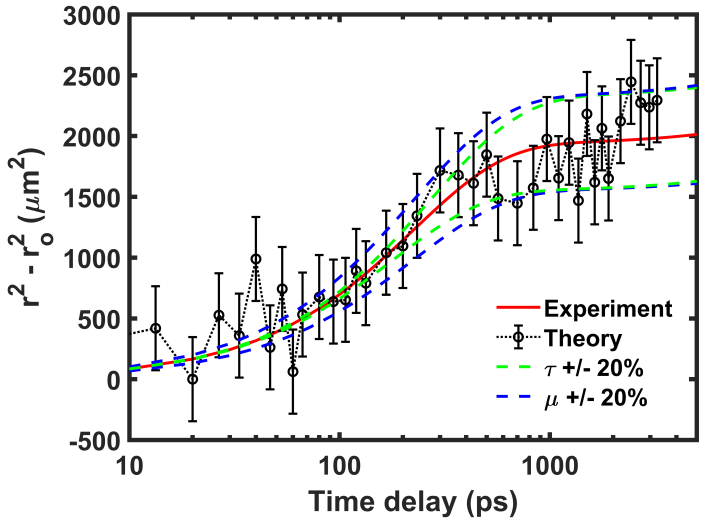

Figure B.4: The squared radius (r^2) of the bright contrast shown in Fig. 4.8A is shown here with additional early time points included. A pump fluence of 100 μJ/cm^2 was used for this measurement. The extracted hot carrier time constant τ was 220 ps.

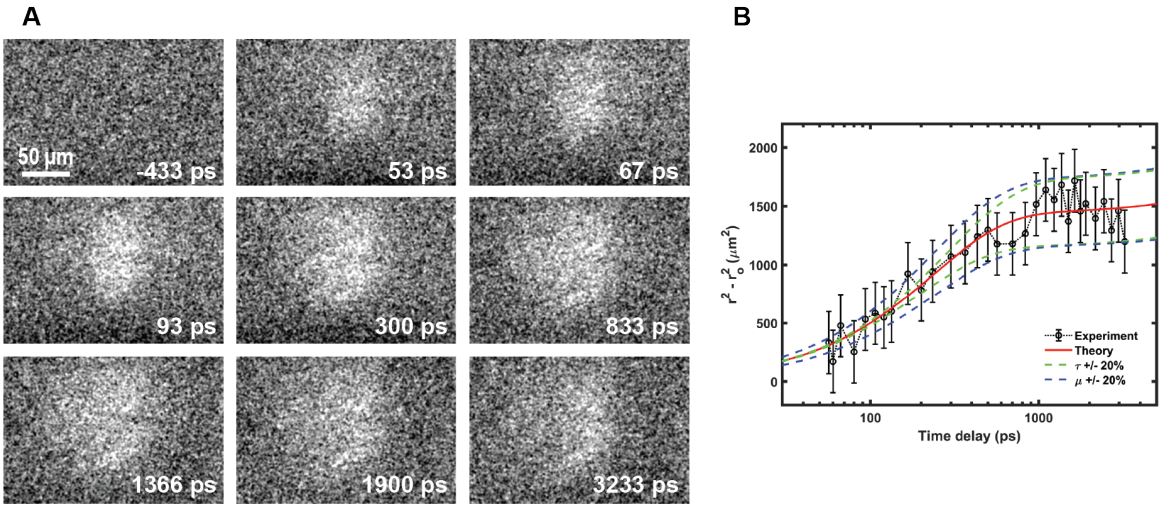

Figure B.5: Additional SUEM difference images taken on BAs single crystals. A pump fluence of 80 μJ/cm^2 was used for this measurement. The extracted hot carrier time constant τ was 233 ps.

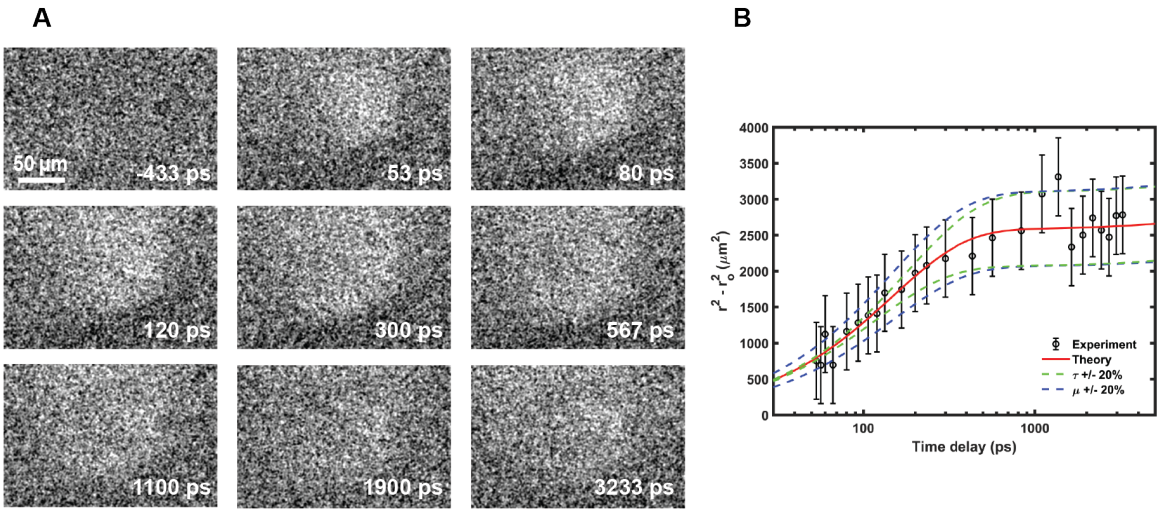

Figure B.6: Additional SUEM difference images taken on BAs single crystals. A pump fluence of 130 μJ/cm^2 was used for this measurement. The extracted hot carrier time constant τ was 145 ps.

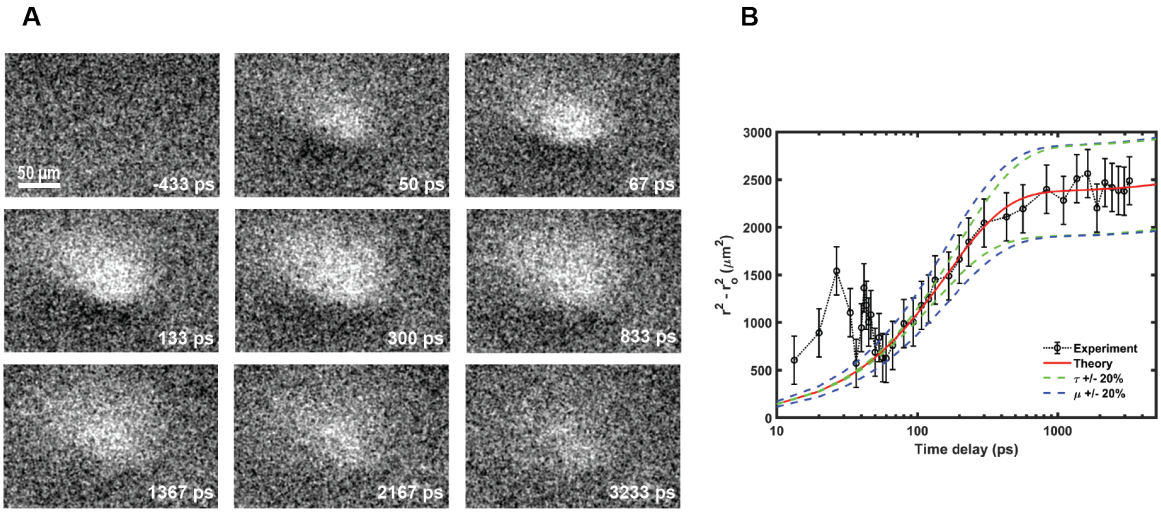

Figure B.7: Additional SUEM difference images taken on BAs single crystals. A pump fluence of 130 μJ/cm^2 was used for this measurement. The extracted hot carrier time constant τ was 160 ps. Initial noisiness is due to weak image contrast before 40 ps.

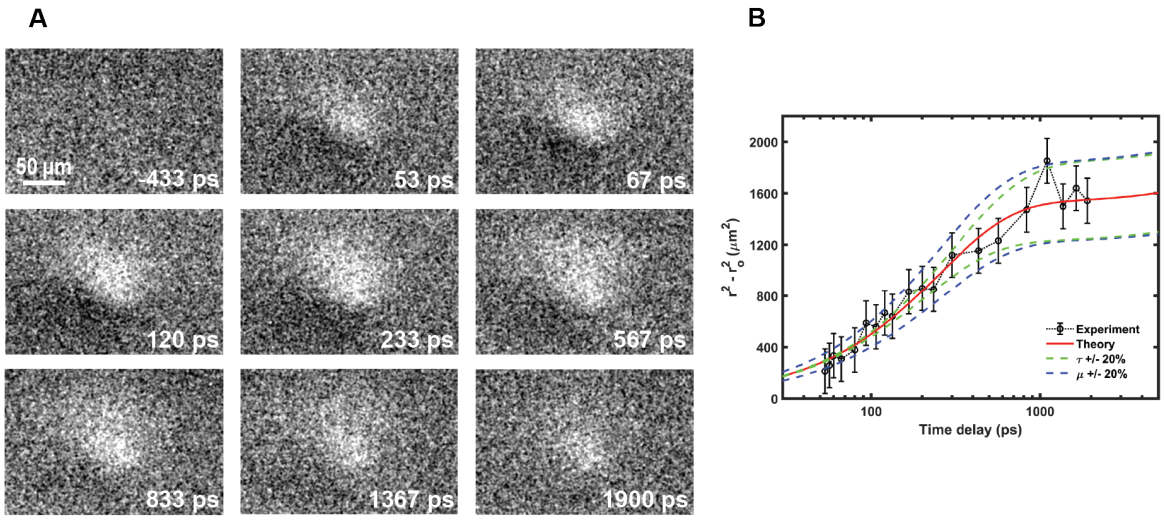

Figure B.8: Additional SUEM difference images taken on BAs single crystals. A pump fluence of 80 μJ/cm^2 was used for this measurement. The extracted hot carrier time constant τ was 250 ps.

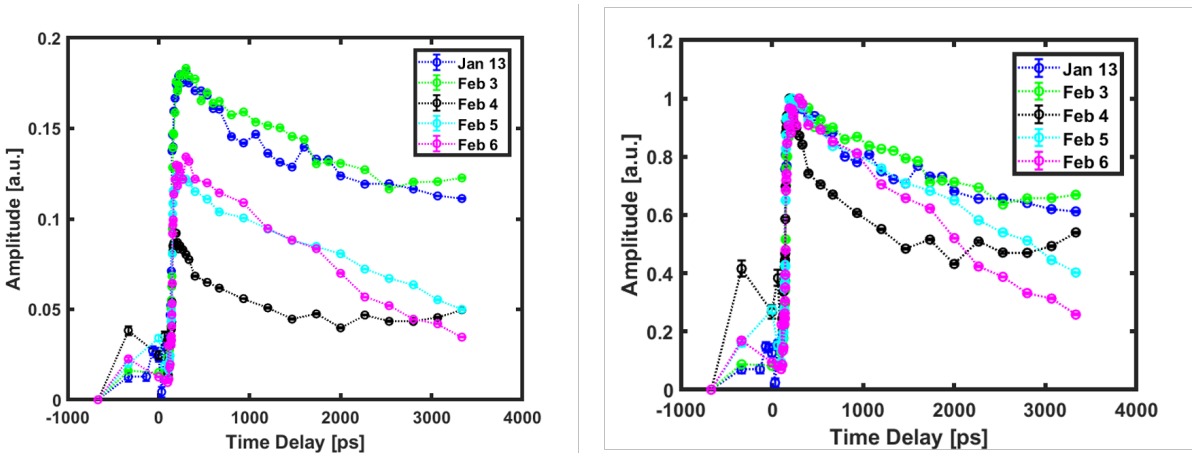

Figure B.9: Left shows BAs amplitude fits vs. time delay for the low fluence data sets. Right shows the normalized fits. No obvious changes in relaxatin dynamics are observed.

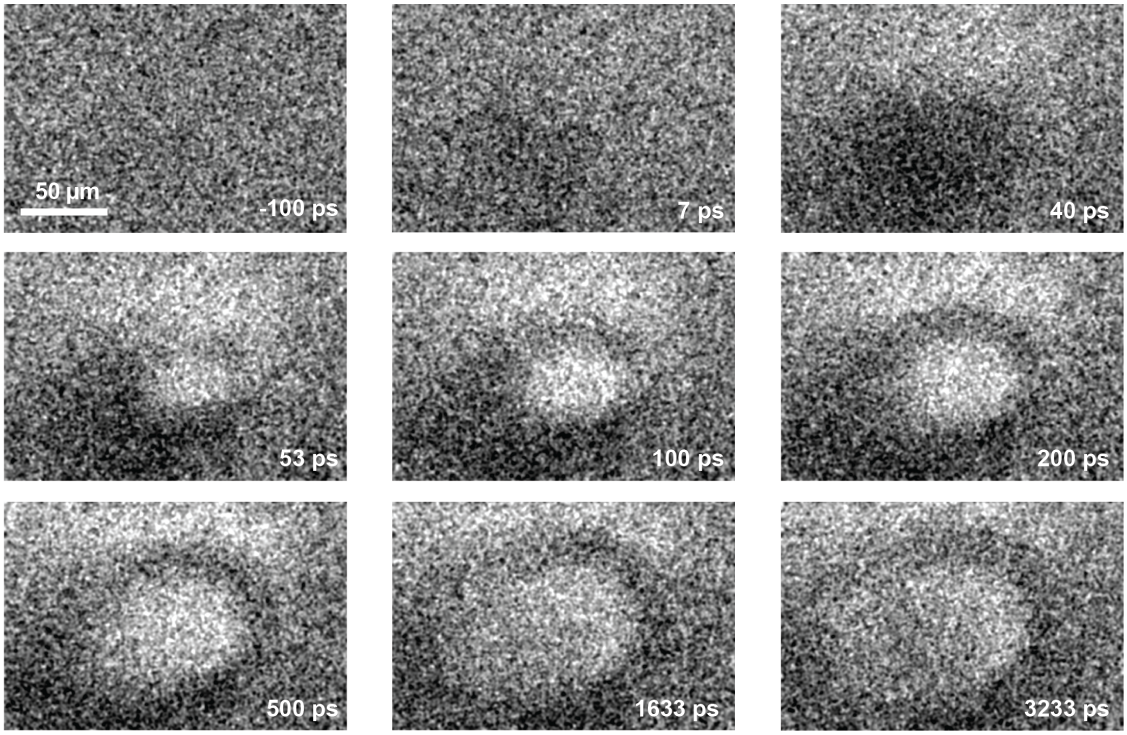

Figure B.10: SUEM difference images taken on BAs single crystal sample. A pump fluence of 185 μJ/cm^2 was used for this measurement.

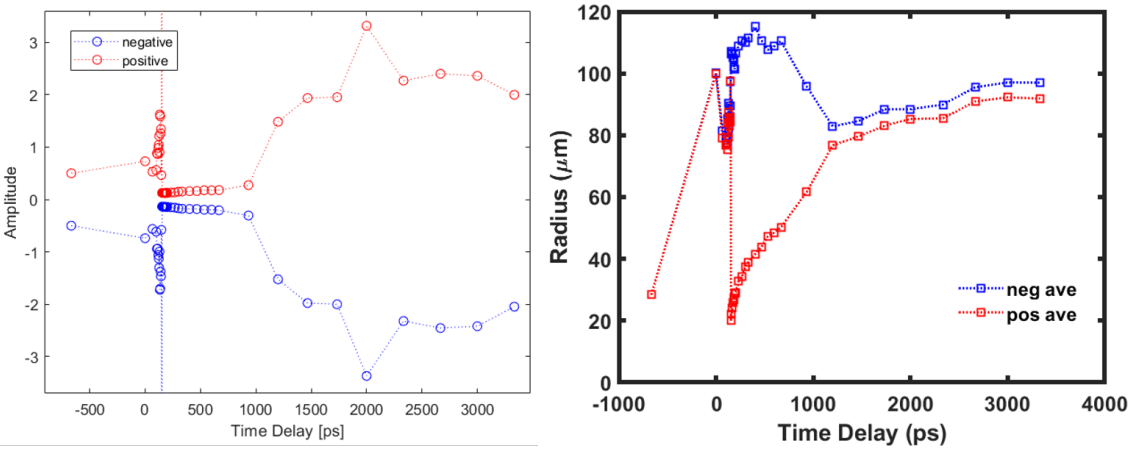

Figure B.11: **Fitting coefficients using superposed Gaussian model.** Left shows extracted amplitudes and right shows averaged radii of the electron and hole distributions shown in Fig. 4.11. A pump fluence of 235 μJ/cm^2 was used for this measurement.

Positive refers to the electron distribution while negative refers to the holes. At early times, the fitting results are reasonable, while at later times the fitting becomes insensitive, as evidenced by the converging radii and diverging amplitudes.

B.3 Growth of BAs thin films

While outside of the scope of this thesis, given it's attractive thermal and optoelectronic properties, growth of BAs high quality thin films has the potential to have great impact in multiple fields. However, there are significant challenges associated with growing thin films of BAs. Elemental boron has a very high melting point and a very low vapor pressure, comparable to elements such as tungsten, niobium, tantalum, and molybdenum, all of which are frequently used in high temperature vacuum applications due to these properties. This makes the vaporization of elemental boron quite difficult and expensive, requiring either an electron beam evaporation system or a suitable furnace. There are some examples of MBE setups incorporating boron sources, such as Hoke et al. who grew boron-doped GaAs films using an MBE machine with a high temperature furnace using a pyrolytic boron nitride crucible [283]. They did not observe any reaction between the boron and the crucible at temperatures up to 1900°C, though nitrogen backflows from the crucible were observed. Another potentially simpler route would be to use metalorganic precursors in a metalorganic chemical vapor deposition (MOCVD) or chemical beam epitaxy (CBE) configuration. MOCVD growth of BN and BP has been demonstrated [284, 285], as has MOCVD growth of boron-doped AlAs and GaAs films [286].

Lattice matching BAs films may also prove challenging. The BAs lattice constant of 4.777 Å is significantly smaller than other III-V semiconductors with similar bonding,

and significantly larger than the wurtzite nitrides that have become very popular in power electronics applications that may benefit from improved heat dissipation. Some additional candidates include the rutile TiO_2 and MgF_2, which have lattice constants of 4.59 Å and 4.64 Å respectively. The (111) plane of BAs has a lattice constant of 3.380 Å, making ZnO (3.249 Å) and GaN (3.189 Å) potential candidates as well. InGaN alloys have lattice constants between 3.189-3.533 Å, also making them intriguing candidates for growth of (111) BAs [287].

The prediction and validation of ultrahigh thermal conductivity in BAs was a remarkable success for the thermal transport community, validating the predictive power of the iterative BTE formalism. However, significant challenges remain that must be addressed before the remarkable thermal properties of BAs can be leveraged in useful electronic devices. The ability to grow high-quality thin films would enable the integration of BAs in devices and could be a potential solution to the thermal management issues in many devices. A CBE based approach using metalorganic boron precursors could be a viable path forward for growth of high-quality BAs films.

Appendix C

Additional α-$RuCl_3$ Data

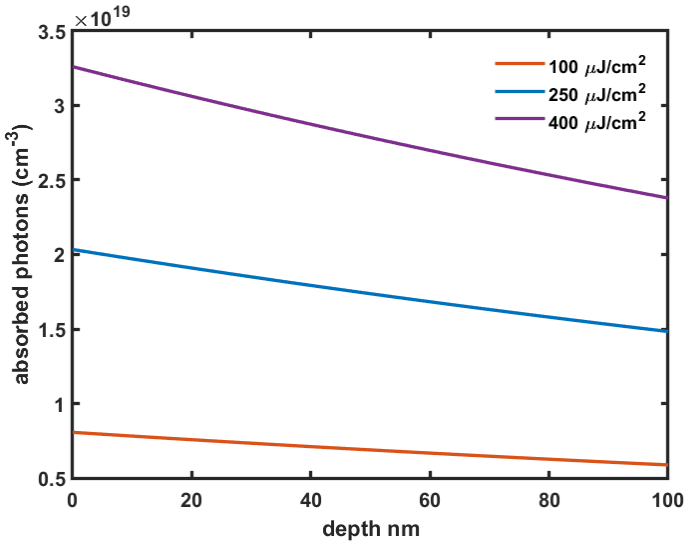

Figure C.1: This figure shows the optically induced excited carrier concentration in the α-$RuCl_3$ flakes as a function of depth in the sample for a few select fluences. The concentration is calculated assuming Beer-Lambert absorption and is given as: $\Delta n(z, t = 0) = F\alpha \exp(-\alpha z)$, where F is the laser fluence in $\frac{\text{photons}}{cm^2}$ and α is the absorption coefficient in cm^{-1}.

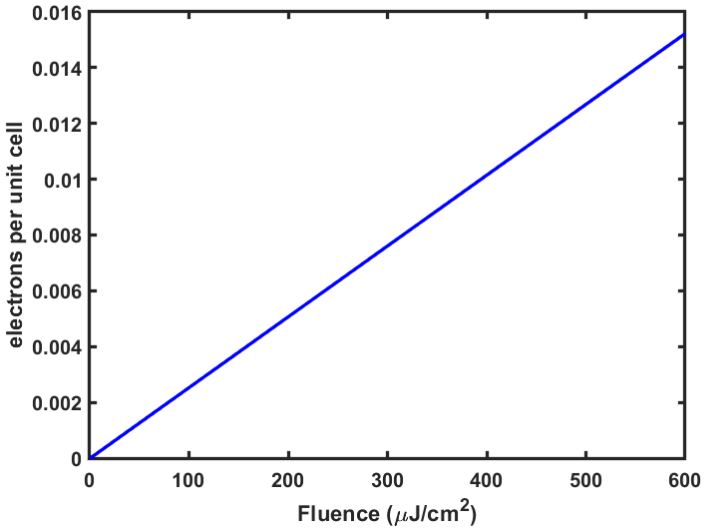

Figure C.2: This figure shows the number of optically induced excited carriers in the α-$RuCl_3$ flakes as a function of fluence.

The transient temperature rise induced by the laser pulse can be estimated by:

$$\Delta T = \frac{E}{CV_v} \tag{C.1}$$

where E is the pulse energy, C_v is the volumetric heat capacity, and V is the volume of the sample being illuminated by the pump. The volume is $V = \pi r^2 d$ where r is the $1/e^2$ radius of the pump beam on the sample and d is the estimated thickness of the α-$RuCl_3$ flake. Only pump laser heating is calculated in this estimation, the effects of electron beam heating are not considered.

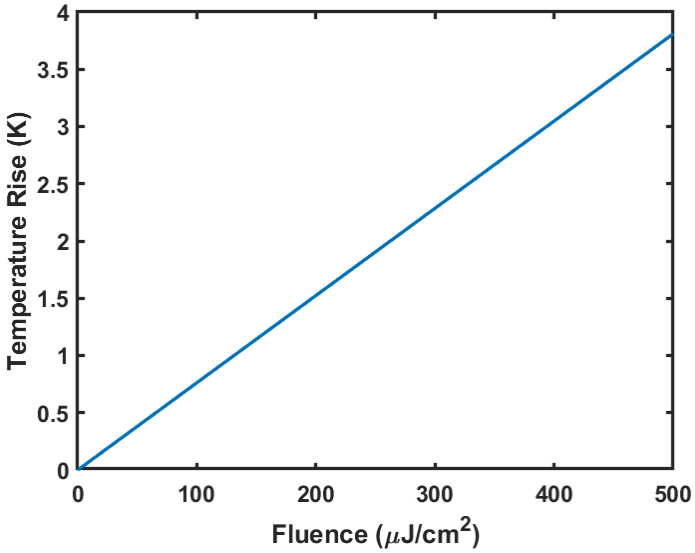

Figure C.3: **Transient temperature rise vs. Fluence** The transient temperature rise induced by absorption of the pump pulse is plotted vs fluence. At very high fluences, a temperature rise of a few K is expected. The heat capacity of α-$RuCl_3$ was taken from [288].

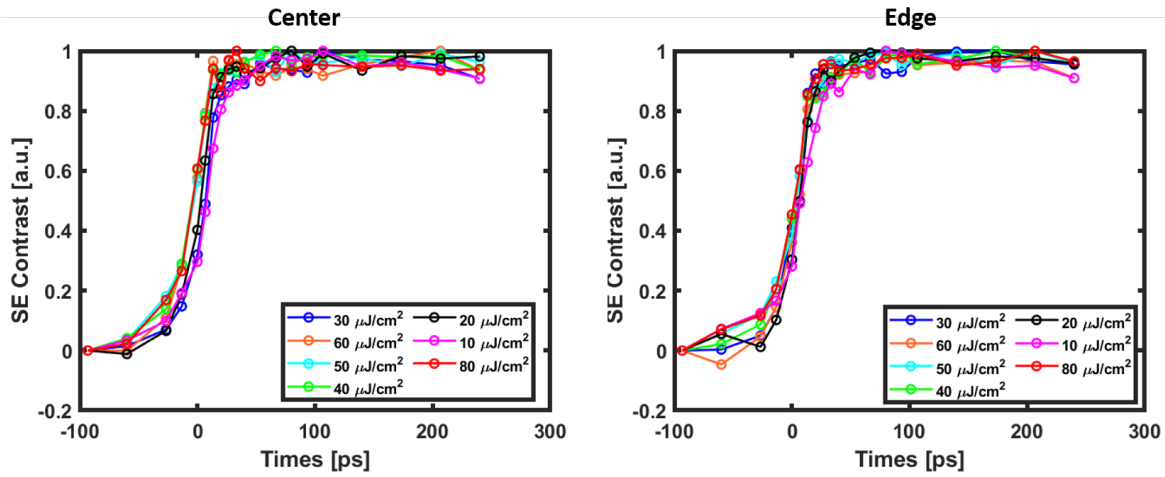

Figure C.4: This figure shows normalized versions of Fig. 5.10. At fluences near the crossover fluence, there's no obvious change in relaxation dynamics at short times.

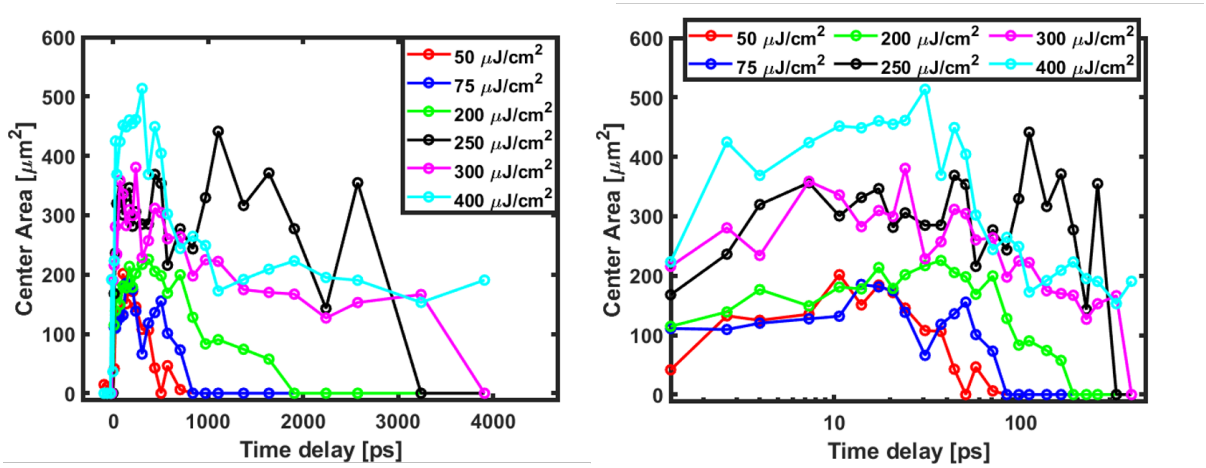

Figure C.5: This figure shows the approximate area of reduced contrast for the datasets shown in Fig. 5.9. The areas were chosen by approximating the inflection point on the edge of the pump spot where the contrast was brightest. While this method is qualitative and very approximate, it does suggest that the overall area that experiences reduced contrast increases with fluence.

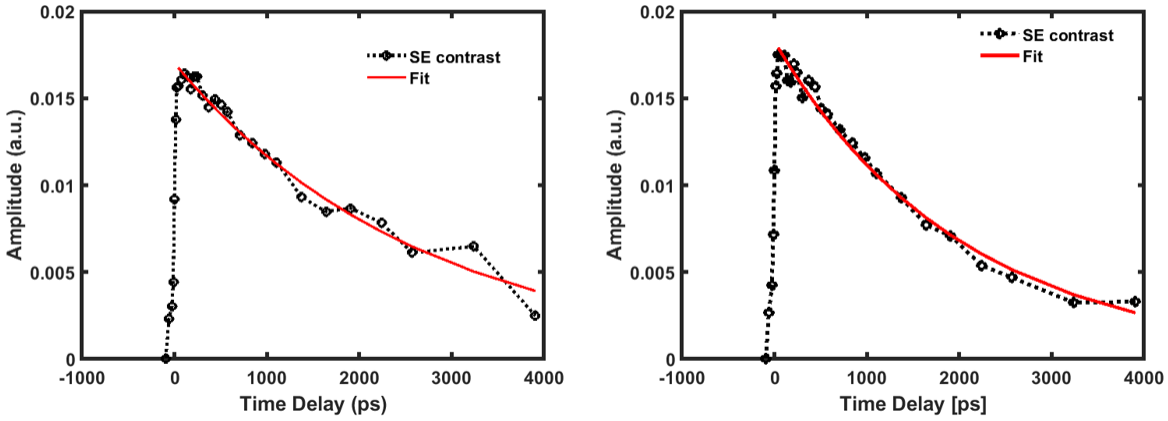

Figure C.6: This figure shows fits of the SE contrast to $exp(-t/\tau)$ in order to determine the approximate timescale of the decay in contrast. The figures on the left and right correspond to a fluences of 30 and 100 $\mu J/cm^2$ respectively. The extracted time constants were τ=2,2656 $\pm$ 264 ps and τ=2,025 $\pm$ 150 ps for the two measurements shown.

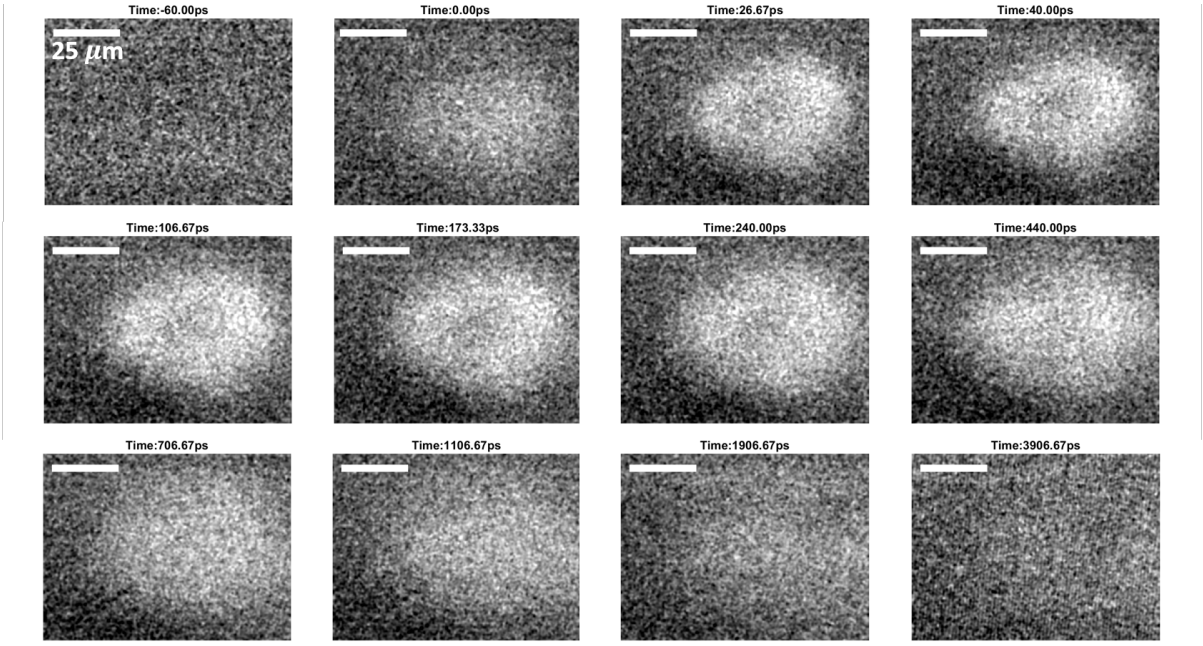

Figure C.7: SUEM difference images taken on α-$RuCl_3$ flake. A pump fluence of 50 $\mu J/cm^2$ was used for this measurement.

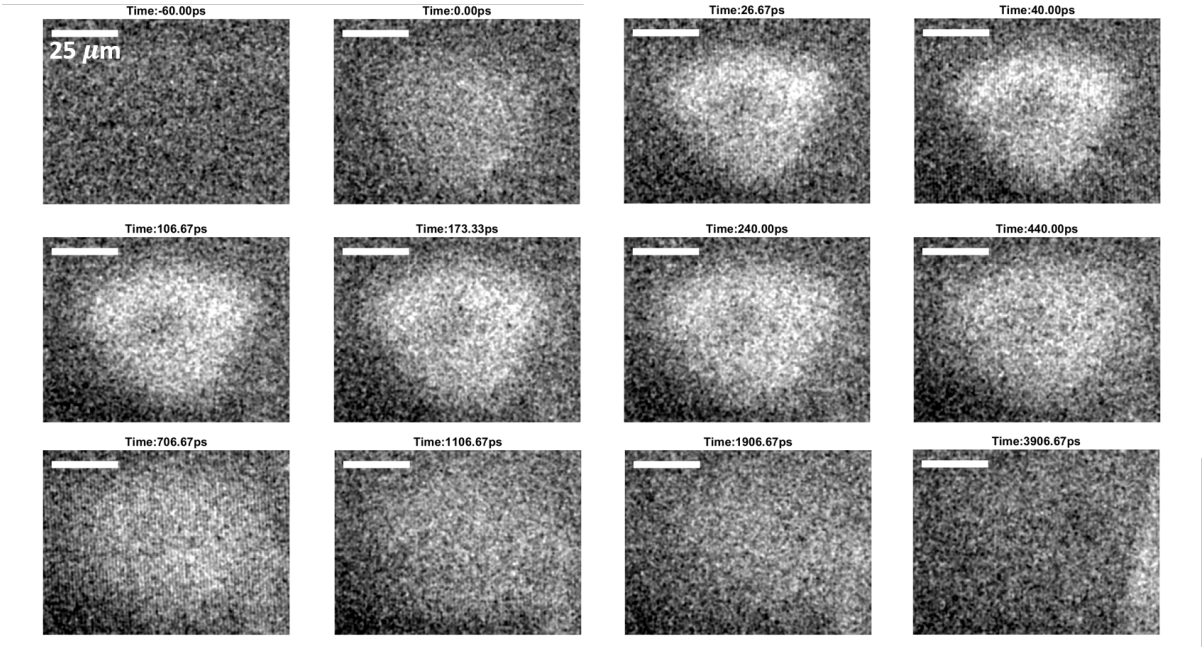

Figure C.8: SUEM difference images taken on α-$RuCl_3$ flake. A pump fluence of 75 $\mu J/cm^2$ was used for this measurement.

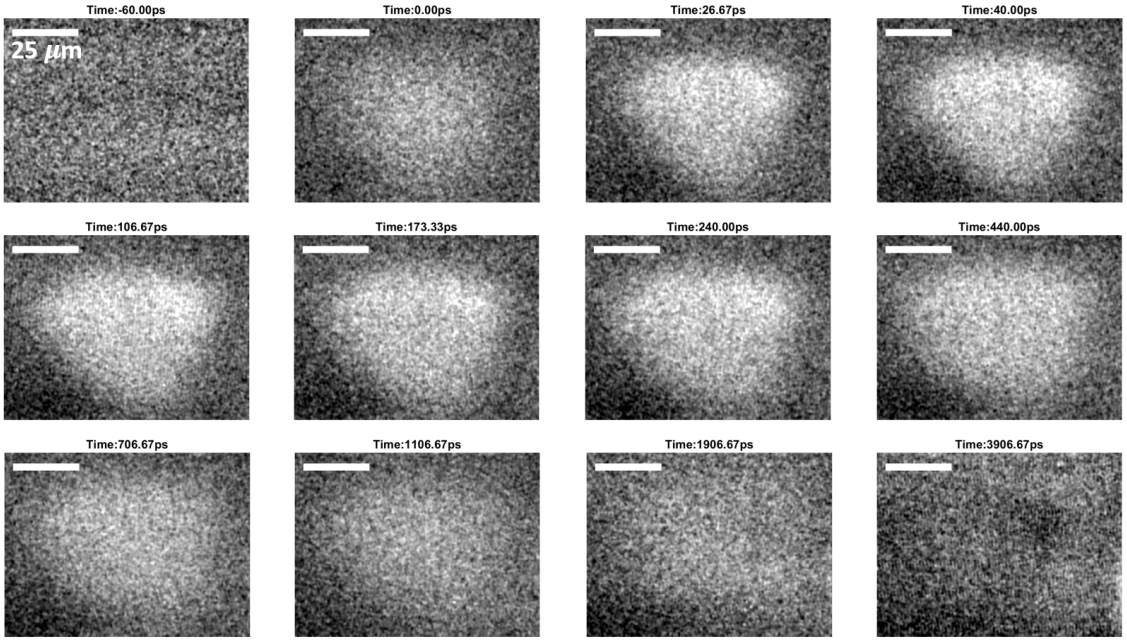

Figure C.9: SUEM difference images taken on α-$RuCl_3$ flake. A pump fluence of 100 $\mu J/cm^2$ was used for this measurement.

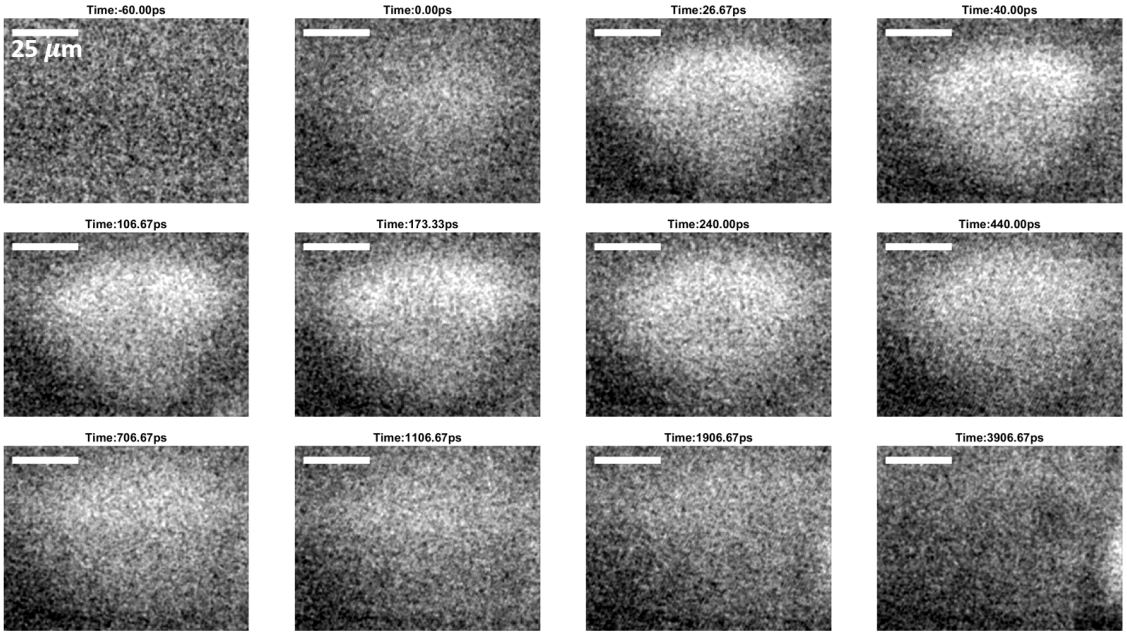

Figure C.10: SUEM difference images taken on α-$RuCl_3$ flake. A pump fluence of 150 $\mu J/cm^2$ was used for this measurement.

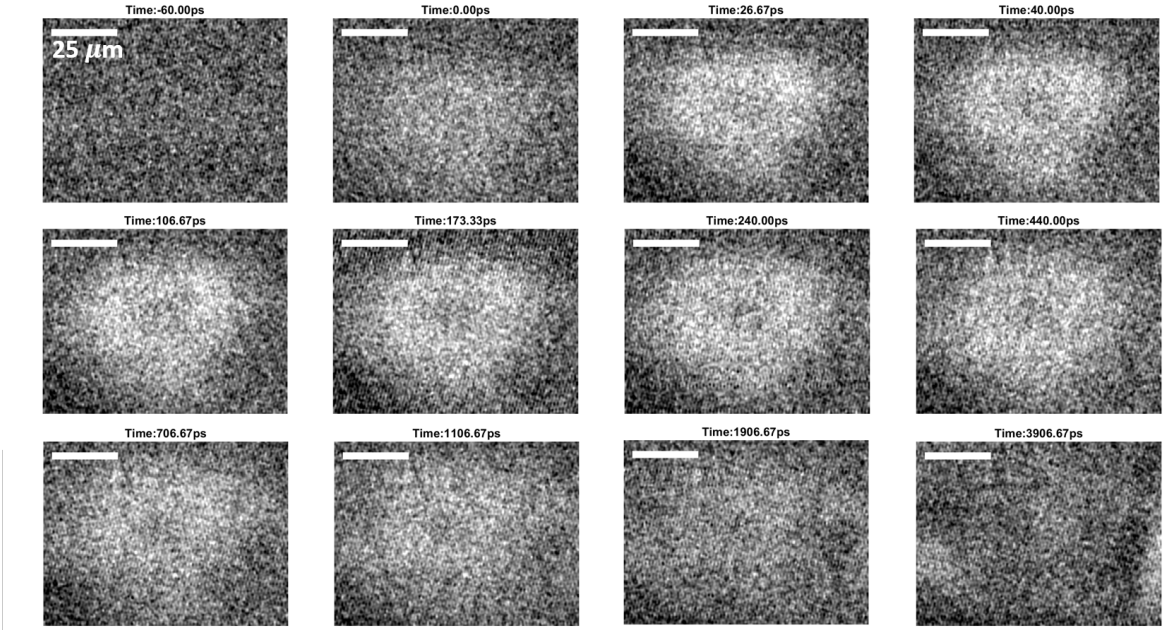

Figure C.11: SUEM difference images taken on α-$RuCl_3$ flake. A pump fluence of 200 $\mu J/cm^2$ was used for this measurement.

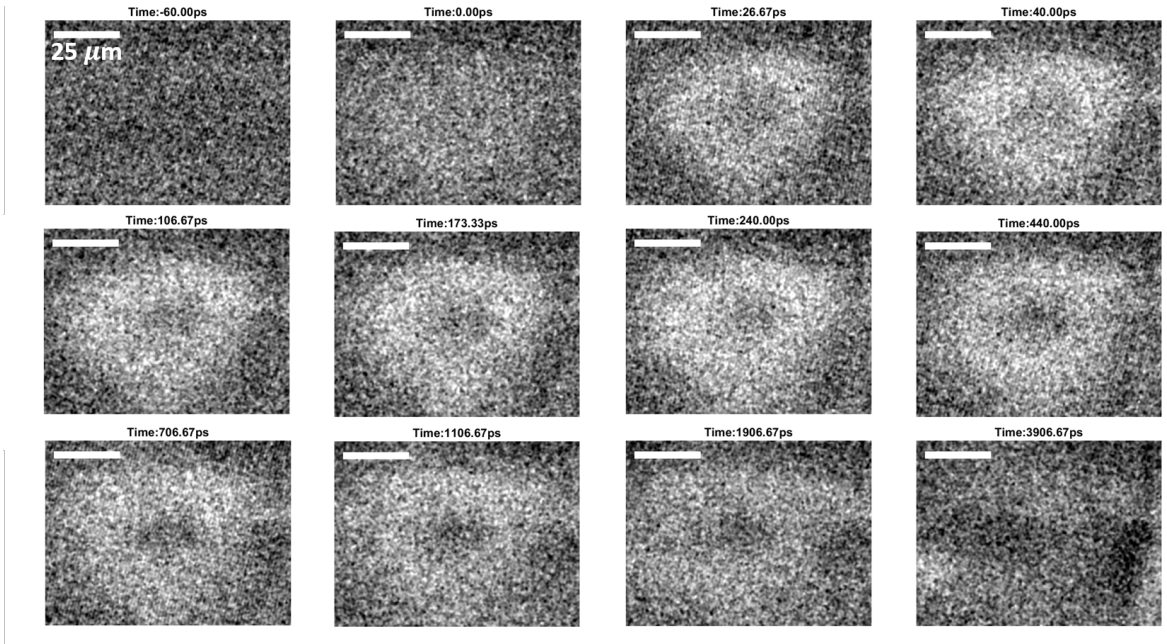

Figure C.12: SUEM difference images taken on α-$RuCl_3$ flake. A pump fluence of 250 $\mu J/cm^2$ was used for this measurement.

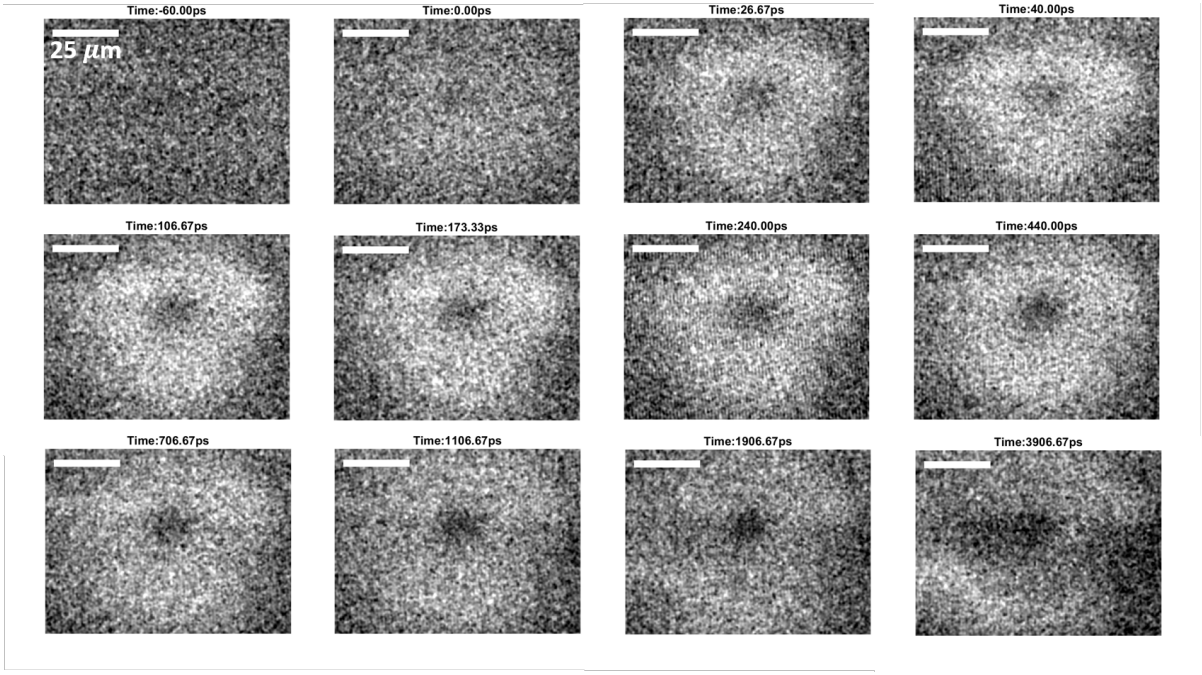

Figure C.13: SUEM difference images taken on α-$RuCl_3$ flake. A pump fluence of 300 $\mu J/cm^2$ was used for this measurement.

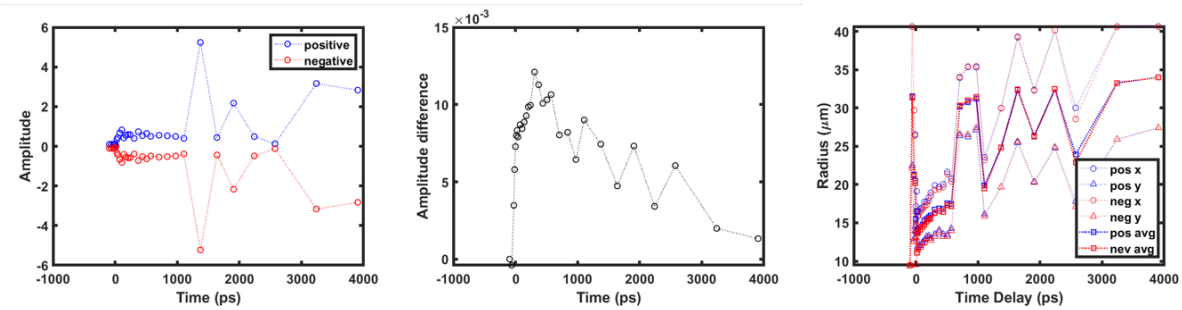

Figure C.14: Some sample 2D Gaussian fits for the 75 $\mu J/cm^2$ measurement shown in Fig. C.8 are shown. The left shows the positive and negative amplitudes, the center shows the amplitude difference, and the right shows the radius.

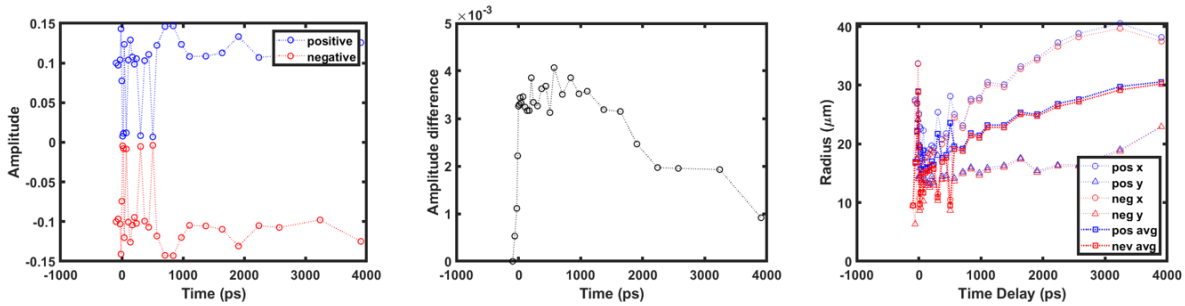

Figure C.15: Some sample 2D Gaussian fits for the 75 μJ/cm^2 measurement shown in Fig. C.11 are shown. The left shows the positive and negative amplitudes, the center shows the amplitude difference, and the right shows the radius.

Bibliography

[1] T. H. Maiman, *Stimulated Optical Radiation in Ruby*, *Nature* **187** (Aug., 1960) 493–494.

[2] F. J. McClung and R. W. Hellwarth, *Giant Optical Pulsations from Ruby*, *Applied Optics* **1** (Jan., 1962) 103–105.

[3] A. J. DeMaria, R. Gagosz, and G. Barnard, *Ultrasonic-Refraction Shutter for Optical Maser Oscillators*, *Journal of Applied Physics* **34** (Mar., 1963) 453–456.

[4] L. E. Hargrove, R. L. Fork, and M. A. Pollack, *Locking of He–Ne Laser Modes Induced by Synchronous Intracavity Modulation*, *Applied Physics Letters* **5** (July, 1964) 4–5.

[5] W. E. Lamb, *Theory of an Optical Maser*, *Physical Review* **134** (June, 1964) A1429–A1450.

[6] M. A. Kovacs, G. W. Flynn, and A. Javan, Q *Switching of Molecular Laser Transitions*, *Applied Physics Letters* **8** (Feb., 1966) 62–63.

[7] U. Choudhry, T. Kim, M. Adams, J. Ranasinghe, R. Yang, and B. Liao, *Characterizing microscale energy transport in materials with transient grating spectroscopy*, *Journal of Applied Physics* **130** (Dec., 2021) 231101.

[8] R. W. Schoenlein, W. Z. Lin, J. G. Fujimoto, and G. L. Eesley, *Femtosecond studies of nonequilibrium electronic processes in metals*, *Physical Review Letters* **58** (Apr., 1987) 1680–1683.

[9] M. Q. Weng, M. W. Wu, and H. L. Cui, *Spin relaxation in n-type GaAs quantum wells with transient spin grating*, *Journal of Applied Physics* **103** (Mar., 2008) 063714.

[10] J. D. Koralek, C. P. Weber, J. Orenstein, B. A. Bernevig, S.-C. Zhang, S. Mack,

and D. D. Awschalom, *Emergence of the persistent spin helix in semiconductor quantum wells*, *Nature* **458** (Apr., 2009) 610–613.

[11] M. Dantus, M. J. Rosker, and A. H. Zewail, *Real-time femtosecond probing of "transition states" in chemical reactions*, *The Journal of Chemical Physics* **87** (Aug., 1987) 2395–2397.

[12] A. M. Weiner, D. E. Leaird, G. P. Wiederrecht, and K. A. Nelson, *Femtosecond Pulse Sequences Used for Optical Manipulation of Molecular Motion*, *Science* **247** (Mar., 1990) 1317–1319.

[13] S. Pedersen, J. L. Herek, and A. H. Zewail, *The Validity of the "Diradical" Hypothesis: Direct Femtoscond Studies of the Transition-State Structures*, *Science* **266** (Nov., 1994) 1359–1364.

[14] S. Huberman, R. A. Duncan, K. Chen, B. Song, V. Chiloyan, Z. Ding, A. A. Maznev, G. Chen, and K. A. Nelson, *Observation of second sound in graphite at temperatures above 100 K*, *Science* **364** (Apr., 2019) 375–379.

[15] Y. Wang and M. Trenary, *Surface chemistry of boron oxidation. 2. The reactions of boron oxides B2O2 and B2O3 with boron films grown on tantalum(110)*, *Chemistry of Materials* **5** (Feb., 1993) 199–205.

[16] J. G. Fujimoto, S. D. Silvestri, E. P. Ippen, C. A. Puliafito, R. Margolis, and A. Oseroff, *Femtosecond optical ranging in biological systems*, *Optics Letters* **11** (Mar., 1986) 150–152.

[17] J. T. Kennis and M.-L. Groot, *Ultrafast spectroscopy of biological photoreceptors*, *Current Opinion in Structural Biology* **17** (Oct., 2007) 623–630.

[18] P. Agostini and L. F. DiMauro, *The physics of attosecond light pulses*, *Reports on Progress in Physics* **67** (May, 2004) 813.

[19] R. López-Martens, K. Varjú, P. Johnsson, J. Mauritsson, Y. Mairesse, P. Salières, M. B. Gaarde, K. J. Schafer, A. Persson, S. Svanberg, C.-G. Wahlström, and A. L'Huillier, *Amplitude and Phase Control of Attosecond Light Pulses*, *Physical Review Letters* **94** (Jan., 2005) 033001.

[20] A. L. Cavalieri, N. Müller, T. Uphues, V. S. Yakovlev, A. Baltuška, B. Horvath, B. Schmidt, L. Blümel, R. Holzwarth, S. Hendel, M. Drescher, U. Kleineberg, P. M. Echenique, R. Kienberger, F. Krausz, and U. Heinzmann, *Attosecond spectroscopy in condensed matter*, *Nature* **449** (Oct., 2007) 1029–1032.

[21] F. Krausz and M. Ivanov, *Attosecond physics*, *Reviews of Modern Physics* **81** (Feb., 2009) 163–234.

[22] E. Ruska, *The development of the electron microscope and of electron microscopy*, *Reviews of Modern Physics* **59** (July, 1987) 627–638.

[23] D. J. Bradley and W. Sibbett, *Subpicosecond chronoscopy*, *Applied Physics Letters* **27** (Oct., 1975) 382–384.

[24] J. Cao, Z. Hao, H. Park, C. Tao, D. Kau, and L. Blaszczyk, *Femtosecond electron diffraction for direct measurement of ultrafast atomic motions*, *Applied Physics Letters* **83** (July, 2003) 1044–1046.

[25] M. S. Grinolds, V. A. Lobastov, J. Weissenrieder, and A. H. Zewail, *Four-dimensional ultrafast electron microscopy of phase transitions*, *Proceedings of the National Academy of Sciences* **103** (Dec., 2006) 18427–18431.

[26] B. Liao and E. Najafi, *Scanning ultrafast electron microscopy: A novel technique to probe photocarrier dynamics with high spatial and temporal resolutions*, *Materials Today Physics* **2** (Sept., 2017) 46–53.

[27] E. Najafi, T. D. Scarborough, J. Tang, and A. Zewail, *Four-dimensional imaging of carrier interface dynamics in p-n junctions*, *Science* **347** (Jan., 2015) 164–167.

[28] B. Liao, H. Zhao, E. Najafi, X. Yan, H. Tian, J. Tice, A. J. Minnich, H. Wang, and A. H. Zewail, *Spatial-Temporal Imaging of Anisotropic Photocarrier Dynamics in Black Phosphorus*, *Nano Letters* **17** (June, 2017) 3675–3680.

[29] J. Wong, A. Davoyan, B. Liao, A. Krayev, K. Jo, E. Rotenberg, A. Bostwick, C. M. Jozwiak, D. Jariwala, A. H. Zewail, and H. A. Atwater, *Spatiotemporal Imaging of Thickness-Induced Band-Bending Junctions*, *Nano Letters* **21** (July, 2021) 5745–5753.

[30] H. Abraham and J. Lemoine, *Disparition instantanée du phénomène de kerr*, *CR Acad. Sci. Hebd Seances Acad. Sci. D* **129** (1899) 206–208.

[31] R. G. W. Norrish and G. Porter, *Chemical reactions produced by very high light intensities*, *Nature* **164** (1949), no. 4172 658–658.

[32] A. H. Zewail, *Femtochemistry*, *The Journal of Physical Chemistry* **97** (1993), no. 48 12427–12446.

[33] A. H. Zewail, *Femtochemistry: Atomic-scale dynamics of the chemical bond*, *The Journal of Physical Chemistry A* **104** (2000), no. 24 5660–5694.

[34] R. Berera, R. van Grondelle, and J. T. Kennis, *Ultrafast transient absorption spectroscopy: principles and application to photosynthetic systems*, *Photosynthesis research* **101** (2009) 105–118.

[35] M. Maiuri, M. Garavelli, and G. Cerullo, *Ultrafast spectroscopy: State of the art and open challenges*, *Journal of the American Chemical Society* **142** (2019), no. 1 3–15.

[36] G. Hastings, J. R. Durrant, J. Barber, G. Porter, and D. R. Klug, *Observation of pheophytin reduction in photosystem two reaction centers using femtosecond transient absorption spectroscopy*, *Biochemistry* **31** (1992), no. 33 7638–7647.

[37] H. Visser, F. Kleima, I. Van Stokkum, R. Van Grondelle, and H. Van Amerongen, *Probing the many energy-transfer processes in the photosynthetic light-harvesting complex ii at 77 k using energy-selective sub-picosecond transient absorption spectroscopy*, *Chemical physics* **210** (1996), no. 1-2 297–312.

[38] D. Polli, P. Altoè, O. Weingart, K. M. Spillane, C. Manzoni, D. Brida, G. Tomasello, G. Orlandi, P. Kukura, R. A. Mathies, *et. al.*, *Conical intersection dynamics of the primary photoisomerization event in vision*, *Nature* **467** (2010), no. 7314 440–443.

[39] T. Yoshihara, R. Katoh, A. Furube, Y. Tamaki, M. Murai, K. Hara, S. Murata, H. Arakawa, and M. Tachiya, *Identification of reactive species in photoexcited nanocrystalline tio2 films by wide-wavelength-range (400- 2500 nm) transient absorption spectroscopy*, *The Journal of Physical Chemistry B* **108** (2004), no. 12 3817–3823.

[40] Q. Cui, F. Ceballos, N. Kumar, and H. Zhao, *Transient absorption microscopy of monolayer and bulk wse2*, *ACS nano* **8** (2014), no. 3 2970–2976.

[41] J. K. Cooper, S. E. Reyes-Lillo, L. H. Hess, C.-M. Jiang, J. B. Neaton, and I. D. Sharp, *Physical origins of the transient absorption spectra and dynamics in thin-film semiconductors: the case of bivo4*, *The Journal of Physical Chemistry C* **122** (2018), no. 36 20642–20652.

[42] J. Tang, J. R. Durrant, and D. R. Klug, *Mechanism of photocatalytic water splitting in tio2. reaction of water with photoholes, importance of charge carrier dynamics, and evidence for four-hole chemistry*, *Journal of the American Chemical Society* **130** (2008), no. 42 13885–13891.

[43] F. M. Pesci, A. J. Cowan, B. D. Alexander, J. R. Durrant, and D. R. Klug, *Charge carrier dynamics on mesoporous wo3 during water splitting*, *The Journal of Physical Chemistry Letters* **2** (2011), no. 15 1900–1903.

[44] R. Godin, Y. Wang, M. A. Zwijnenburg, J. Tang, and J. R. Durrant, *Time-resolved spectroscopic investigation of charge trapping in carbon nitrides photocatalysts for hydrogen generation*, *Journal of the American Chemical Society* **139** (2017), no. 14 5216–5224.

[45] S. K. Cushing, J. Li, F. Meng, T. R. Senty, S. Suri, M. Zhi, M. Li, A. D. Bristow, and N. Wu, *Photocatalytic activity enhanced by plasmonic resonant energy transfer from metal to semiconductor*, *Journal of the American Chemical Society* **134** (2012), no. 36 15033–15041.

[46] V. I. Klimov, S. A. Ivanov, J. Nanda, M. Achermann, I. Bezel, J. A. McGuire, and A. Piryatinski, *Single-exciton optical gain in semiconductor nanocrystals*, *Nature* **447** (2007), no. 7143 441–446.

[47] K. Wu, J. Chen, J. R. McBride, and T. Lian, *Efficient hot-electron transfer by a plasmon-induced interfacial charge-transfer transition*, *Science* **349** (2015), no. 6248 632–635.

[48] S. Rawalekar, S. Kaniyankandy, S. Verma, and H. N. Ghosh, *Ultrafast charge carrier relaxation and charge transfer dynamics of cdte/cds core- shell quantum dots as studied by femtosecond transient absorption spectroscopy*, *The Journal of Physical Chemistry C* **114** (2010), no. 3 1460–1466.

[49] J. Chwalek, C. Uher, J. F. Whitaker, G. A. Mourou, J. Agostinelli, and M. Lelental, *Femtosecond optical absorption studies of nonequilibrium electronic processes in high t c superconductors*, *Applied Physics Letters* **57** (1990), no. 16 1696–1698.

[50] S. Brorson, A. Kazeroonian, D. Face, T. Cheng, G. Doll, M. Dresselhaus, G. Dresselhaus, E. Ippen, T. Venkatesan, X. Wu, *et. al.*, *Femtosecond thermomodulation study of high-tc superconductors*, *Solid state communications* **74** (1990), no. 12 1305–1308.

[51] G. P. Segre, N. Gedik, J. Orenstein, D. A. Bonn, R. Liang, and W. N. Hardy, *Photoinduced changes of reflectivity in single crystals of yba 2 cu 3 o 6.5 (ortho ii)*, *Physical review letters* **88** (2002), no. 13 137001.

[52] M. F. Jager, C. Ott, P. M. Kraus, C. J. Kaplan, W. Pouse, R. E. Marvel, R. F. Haglund, D. M. Neumark, and S. R. Leone, *Tracking the insulator-to-metal phase transition in vo2 with few-femtosecond extreme uv transient absorption spectroscopy*, *Proceedings of the National Academy of Sciences* **114** (2017), no. 36 9558–9563.

[53] Y. Kim, *Ultrafast transient absorption spectroscopy of strongly correlated mott insulators*, *Physical Review B* **108** (2023), no. 3 035122.

[54] A. Vega-Flick, D. Jung, S. Yue, J. E. Bowers, and B. Liao, *Reduced thermal conductivity of epitaxial GaAs on Si due to symmetry-breaking biaxial strain*, *Physical Review Materials* **3** (Mar., 2019).

[55] W. Ouyang, Y. Li, B. Yurash, N. Schopp, A. Vega-Flick, V. Brus, T.-Q. Nguyen, and B. Liao, *Transient grating spectroscopy of photocarrier dynamics in semiconducting polymer thin films*, *Applied Physics Letters* **117** (2020), no. 25.

[56] R. Yang, H. Szeto, B. Zou, E. Spitaleri, B. Liao, and Y. Zhu, *In situ monitoring of lithium electrodeposition using transient grating spectroscopy*, *Applied Physics Letters* **123** (2023), no. 15.

[57] N. Gedik, *Diffusion of Nonequilibrium Quasi-Particles in a Cuprate Superconductor*, *Science* **300** (May, 2003) 1410–1412.

[58] C. P. Weber, N. Gedik, J. E. Moore, J. Orenstein, J. Stephens, and D. D. Awschalom, *Observation of spin Coulomb drag in a two-dimensional electron gas*, *Nature* **437** (Oct., 2005) 1330–1333.

[59] J. A. Johnson, A. A. Maznev, J. Cuffe, J. K. Eliason, A. J. Minnich, T. Kehoe, C. M. S. Torres, G. Chen, and K. A. Nelson, *Direct Measurement of Room-Temperature Nondiffusive Thermal Transport Over Micron Distances in a Silicon Membrane*, *Physical Review Letters* **110** (Jan., 2013) 025901.

[60] L. Huang, G. V. Hartland, L.-Q. Chu, Luxmi, R. M. Feenstra, C. Lian, K. Tahy, and H. Xing, *Ultrafast transient absorption microscopy studies of carrier dynamics in epitaxial graphene*, *Nano letters* **10** (2010), no. 4 1308–1313.

[61] Z. Guo, Y. Wan, M. Yang, J. Snaider, K. Zhu, and L. Huang, *Long-range hot-carrier transport in hybrid perovskites visualized by ultrafast microscopy*, *Science* **356** (2017), no. 6333 59–62.

[62] J. M. Cowley, *Electron Diffraction Techniques*. International Union of Crystallography, 1992.

[63] B. K. Vainshtein, *Structure Analysis by Electron Diffraction*. Elsevier, Oct., 2013.

[64] L. O. Brockway, *Electron Diffraction by Gas Molecules*, *Reviews of Modern Physics* **8** (July, 1936) 231–266.

[65] I. Hargittai and M. Hargittai, *Stereochemical Applications of Gas-Phase Electron Diffraction, Part A*. John Wiley & Sons, Oct., 1988.

[66] A. H. Zewail, *4d Ultrafast Electron Diffraction, Crystallography, and Microscopy*, *Annual Review of Physical Chemistry* **57** (2006), no. 1 65–103.

[67] A. M. PROKHOROV and M. Y. SCHELEV, *Streak-camera technology makes rapid strides*, *Streak-camera technology makes rapid strides* **25** (1989), no. 2 85–92.

[68] G. Mourou and S. Williamson, *Picosecond electron diffraction*, *Applied Physics Letters* **41** (July, 1982) 44–45.

[69] S. Williamson, G. Mourou, and J. C. M. Li, *Time-Resolved Laser-Induced Phase Transformation in Aluminum*, *Physical Review Letters* **52** (June, 1984) 2364–2367.

[70] H. E. Elsayed-Ali and G. A. Mourou, *Picosecond reflection high-energy electron diffraction*, *Applied Physics Letters* **52** (Jan., 1988) 103–104.

[71] H. E. Elsayed-Ali and J. W. Herman, *Ultrahigh vacuum picosecond laser-driven electron diffraction system*, *Review of Scientific Instruments* **61** (June, 1990) 1636–1647.

[72] J. C. Williamson, J. Cao, H. Ihee, H. Frey, and A. H. Zewail, *Clocking transient chemical changes by ultrafast electron diffraction*, *Nature* **386** (Mar., 1997) 159–162.

[73] J. C. Williamson and A. H. Zewail, *Structural femtochemistry: Experimental methodology.*, *Proceedings of the National Academy of Sciences* **88** (June, 1991) 5021–5025.

[74] A. H. Zewail, *Femtosecond transition-state dynamics*, *Faraday Discussions of the Chemical Society* **91** (Jan., 1991) 207–237.

[75] J. C. Williamson, M. Dantus, S. B. Kim, and A. H. Zewail, *Ultrafast diffraction and molecular structure*, *Chemical Physics Letters* **196** (Aug., 1992) 529–534.

[76] C.-Y. Ruan, F. Vigliotti, V. A. Lobastov, S. Chen, and A. H. Zewail, *Ultrafast electron crystallography: Transient structures of molecules, surfaces, and phase transitions*, *Proceedings of the National Academy of Sciences* **101** (Feb., 2004) 1123–1128.

[77] H. Ihee, V. A. Lobastov, U. M. Gomez, B. M. Goodson, R. Srinivasan, C. Y. Ruan, and A. H. Zewail, *Direct imaging of transient molecular structures with ultrafast diffraction*, *Science (New York, N.Y.)* **291** (Jan., 2001) 458–462.

[78] R. Srinivasan, J. S. Feenstra, S. T. Park, S. Xu, and A. H. Zewail, *Dark Structures in Molecular Radiationless Transitions Determined by Ultrafast Diffraction*, *Science* **307** (Jan., 2005) 558–563.

[79] V. A. Lobastov, R. Srinivasan, F. Vigliotti, C.-Y. Ruan, J. S. Feenstra, S. Chen, S. T. Park, S. Xu, and A. H. Zewail, *Ultrafast Electron Diffraction*, in *Ultrafast Optics IV: Selected Contributions to the 4th International Conference on Ultrafast Optics, Vienna, Austria* (F. Krausz, G. Korn, P. Corkum, and I. A. Walmsley, eds.), Springer Series in OPTICAL SCIENCES, pp. 419–435. Springer, New York, NY, 2004.

[80] B. J. Siwick, J. R. Dwyer, R. E. Jordan, and R. J. D. Miller, *An Atomic-Level View of Melting Using Femtosecond Electron Diffraction*, *Science* **302** (Nov., 2003) 1382–1385.

[81] A. A. Ischenko, S. A. Aseyev, V. N. Bagratashvili, V. Y. Panchenko, and E. A. Ryabov, *Ultrafast electron diffraction and electron microscopy: Present status and future prospects*, *Physics-Uspekhi* **57** (July, 2014) 633.

[82] F. Vigliotti, S. Chen, C.-Y. Ruan, V. A. Lobastov, and A. H. Zewail, *Ultrafast Electron Crystallography of Surface Structural Dynamics with Atomic-Scale Resolution*, *Angewandte Chemie* **116** (2004), no. 20 2759–2763.

[83] D. S. Badali, R. Y. N. Gengler, and R. J. D. Miller, *Ultrafast electron diffraction optimized for studying structural dynamics in thin films and monolayers*, *Structural Dynamics* **3** (May, 2016) 034302.

[84] M. Z. Mo, Z. Chen, R. K. Li, M. Dunning, B. B. L. Witte, J. K. Baldwin, L. B. Fletcher, J. B. Kim, A. Ng, R. Redmer, A. H. Reid, P. Shekhar, X. Z. Shen, M. Shen, K. Sokolowski-Tinten, Y. Y. Tsui, Y. Q. Wang, Q. Zheng, X. J. Wang, and S. H. Glenzer, *Heterogeneous to homogeneous melting transition visualized with ultrafast electron diffraction*, *Science* **360** (June, 2018) 1451–1455.

[85] V. R. Morrison, Robert. P. Chatelain, K. L. Tiwari, A. Hendaoui, A. Bruhács, M. Chaker, and B. J. Siwick, *A photoinduced metal-like phase of monoclinic VO2 revealed by ultrafast electron diffraction*, *Science* **346** (Oct., 2014) 445–448.

[86] A. Zong, A. Kogar, and N. Gedik, *Unconventional light-induced states visualized by ultrafast electron diffraction and microscopy*, *MRS Bulletin* **46** (Aug., 2021) 720–730.

[87] J. Yang, X. Zhu, J. P. F. Nunes, J. K. Yu, R. M. Parrish, T. J. A. Wolf, M. Centurion, M. Gühr, R. Li, Y. Liu, B. Moore, M. Niebuhr, S. Park, X. Shen, S. Weathersby, T. Weinacht, T. J. Martinez, and X. Wang, *Simultaneous*

observation of nuclear and electronic dynamics by ultrafast electron diffraction, *Science* **368** (May, 2020) 885–889.

[88] R. P. Chatelain, V. R. Morrison, B. L. M. Klarenaar, and B. J. Siwick, *Coherent and Incoherent Electron-Phonon Coupling in Graphite Observed with Radio-Frequency Compressed Ultrafast Electron Diffraction*, *Physical Review Letters* **113** (Dec., 2014) 235502.

[89] R. Li, C. Tang, Y. Du, W. Huang, Q. Du, J. Shi, L. Yan, and X. Wang, *Experimental demonstration of high quality MeV ultrafast electron diffraction*, *Review of Scientific Instruments* **80** (Aug., 2009) 083303.

[90] S. P. Weathersby, G. Brown, M. Centurion, T. F. Chase, R. Coffee, J. Corbett, J. P. Eichner, J. C. Frisch, A. R. Fry, M. Gühr, N. Hartmann, C. Hast, R. Hettel, R. K. Jobe, E. N. Jongewaard, J. R. Lewandowski, R. K. Li, A. M. Lindenberg, I. Makasyuk, J. E. May, D. McCormick, M. N. Nguyen, A. H. Reid, X. Shen, K. Sokolowski-Tinten, T. Vecchione, S. L. Vetter, J. Wu, J. Yang, H. A. Dürr, and X. J. Wang, *Mega-electron-volt ultrafast electron diffraction at SLAC National Accelerator Laboratory*, *Review of Scientific Instruments* **86** (July, 2015) 073702.

[91] X. Shen, J. P. F. Nunes, J. Yang, R. K. Jobe, R. K. Li, M.-F. Lin, B. Moore, M. Niebuhr, S. P. Weathersby, T. J. A. Wolf, C. Yoneda, M. Guehr, M. Centurion, and X. J. Wang, *Femtosecond gas-phase mega-electron-volt ultrafast electron diffraction*, *Structural Dynamics* **6** (Oct., 2019) 054305.

[92] J. P. F. Nunes, K. Ledbetter, M. Lin, M. Kozina, D. P. DePonte, E. Biasin, M. Centurion, C. J. Crissman, M. Dunning, S. Guillet, K. Jobe, Y. Liu, M. Mo, X. Shen, R. Sublett, S. Weathersby, C. Yoneda, T. J. A. Wolf, J. Yang, A. A. Cordones, and X. J. Wang, *Liquid-phase mega-electron-volt ultrafast electron diffraction*, *Structural Dynamics* **7** (Mar., 2020) 024301.

[93] C. Xu, C. Jin, Z. Chen, Q. Lu, Y. Cheng, B. Zhang, F. Qi, J. Chen, X. Yin, G. Wang, D. Xiang, and D. Qian, *Transient dynamics of the phase transition in VO2 revealed by mega-electron-volt ultrafast electron diffraction*, *Nature Communications* **14** (Mar., 2023) 1265.

[94] V. A. Lobastov, R. Srinivasan, and A. H. Zewail, *Four-dimensional ultrafast electron microscopy*, *Proceedings of the National Academy of Sciences* **102** (2005), no. 20 7069–7073.

[95] O. Bostanjoglo, *High-speed electron microscopy*, in *Advances in imaging and electron physics*, vol. 121, pp. 1–51. Elsevier, 2002.

[96] H. S. Park, J. S. Baskin, O.-H. Kwon, and A. H. Zewail, *Atomic-scale imaging in*

real and energy space developed in ultrafast electron microscopy, *Nano Letters* **7** (2007), no. 9 2545–2551.

[97] D. R. Cremons, D. A. Plemmons, and D. J. Flannigan, *Femtosecond electron imaging of defect-modulated phonon dynamics*, *Nature communications* **7** (2016), no. 1 11230.

[98] D. A. Plemmons, P. K. Suri, and D. J. Flannigan, *Probing structural and electronic dynamics with ultrafast electron microscopy*, *Chemistry of Materials* **27** (2015), no. 9 3178–3192.

[99] O.-H. Kwon, B. Barwick, H. S. Park, J. S. Baskin, and A. H. Zewail, *Nanoscale mechanical drumming visualized by 4d electron microscopy*, *Nano letters* **8** (2008), no. 11 3557–3562.

[100] D. J. Flannigan and A. H. Zewail, *Optomechanical and crystallization phenomena visualized with 4d electron microscopy: Interfacial carbon nanotubes on silicon nitride*, *Nano letters* **10** (2010), no. 5 1892–1899.

[101] A. J. McKenna, J. K. Eliason, and D. J. Flannigan, *Spatiotemporal evolution of coherent elastic strain waves in a single mos2 flake*, *Nano letters* **17** (2017), no. 6 3952–3958.

[102] D. T. Valley, V. E. Ferry, and D. J. Flannigan, *Imaging intra-and interparticle acousto-plasmonic vibrational dynamics with ultrafast electron microscopy*, *Nano letters* **16** (2016), no. 11 7302–7308.

[103] R. A. Gnabasik, P. K. Suri, J. Chen, and D. J. Flannigan, *Imaging coherent phonons and precursor dynamics in lafeaso with 4d ultrafast electron microscopy*, *Physical Review Materials* **6** (2022), no. 2 024802.

[104] A. Yurtsever and A. H. Zewail, *4d nanoscale diffraction observed by convergent-beam ultrafast electron microscopy*, *Science* **326** (2009), no. 5953 708–712.

[105] A. Yurtsever and A. H. Zewail, *Kikuchi ultrafast nanodiffraction in four-dimensional electron microscopy*, *Proceedings of the National Academy of Sciences* **108** (2011), no. 8 3152–3156.

[106] A. Yurtsever, S. Schaefer, and A. H. Zewail, *Ultrafast kikuchi diffraction: Nanoscale stress–strain dynamics of wave-guiding structures*, *Nano letters* **12** (2012), no. 7 3772–3777.

[107] R. M. Van Der Veen, O.-H. Kwon, A. Tissot, A. Hauser, and A. H. Zewail,

Single-nanoparticle phase transitions visualized by four-dimensional electron microscopy, *Nature chemistry* **5** (2013), no. 5 395–402.

[108] D. J. Flannigan, D. R. Cremons, and D. T. Valley, *Multimodal visualization of the optomechanical response of silicon cantilevers with ultrafast electron microscopy*, *Journal of Materials Research* **32** (2017), no. 1 239–247.

[109] O.-H. Kwon, V. Ortalan, and A. H. Zewail, *Macromolecular structural dynamics visualized by pulsed dose control in 4d electron microscopy*, *Proceedings of the National Academy of Sciences* **108** (2011), no. 15 6026–6031.

[110] B. Barwick, H. S. Park, O.-H. Kwon, J. S. Baskin, and A. H. Zewail, *4D Imaging of Transient Structures and Morphologies in Ultrafast Electron Microscopy*, *Science* **322** (Nov., 2008) 1227–1231.

[111] B. Barwick, D. J. Flannigan, and A. H. Zewail, *Photon-induced near-field electron microscopy*, *Nature* **462** (2009), no. 7275 902–906.

[112] A. Yurtsever and A. H. Zewail, *Direct visualization of near-fields in nanoplasmonics and nanophotonics*, *Nano letters* **12** (2012), no. 6 3334–3338.

[113] L. Piazza, T. Lummen, E. Quinonez, Y. Murooka, B. Reed, B. Barwick, and F. Carbone, *Simultaneous observation of the quantization and the interference pattern of a plasmonic near-field*, *Nature communications* **6** (2015), no. 1 6407.

[114] D. J. Flannigan, W. A. Curtis, E. J. VandenBussche, and Y. Zhang, *Low repetition-rate, high-resolution femtosecond transmission electron microscopy*, *The Journal of chemical physics* **157** (2022), no. 18.

[115] P. Baum and A. H. Zewail, *Attosecond electron pulses for 4d diffraction and microscopy*, *Proceedings of the National Academy of Sciences* **104** (2007), no. 47 18409–18414.

[116] K. E. Priebe, C. Rathje, S. V. Yalunin, T. Hohage, A. Feist, S. Schäfer, and C. Ropers, *Attosecond electron pulse trains and quantum state reconstruction in ultrafast transmission electron microscopy*, *Nature Photonics* **11** (Dec., 2017) 793–797.

[117] Y. Morimoto and P. Baum, *Diffraction and microscopy with attosecond electron pulse trains*, *Nature Physics* **14** (2018), no. 3 252–256.

[118] M. T. Hassan, *Attomicroscopy: from femtosecond to attosecond electron microscopy*, *Journal of Physics B: Atomic, Molecular and Optical Physics* **51** (2018), no. 3 032005.

[119] Y. Morimoto, *Attosecond electron-beam technology: a review of recent progress*, *Microscopy* **72** (2023), no. 1 2–17.

[120] S. R. Ellis, N. C. Bartelt, F. Léonard, K. C. Celio, E. J. Fuller, D. R. Hughart, D. Garland, M. J. Marinella, J. R. Michael, D. W. Chandler, B. Liao, and A. A. Talin, *Scanning ultrafast electron microscopy reveals photovoltage dynamics at a deeply buried p - Si / Si O 2 interface*, *Physical Review B* **104** (Oct., 2021) L161303.

[121] M. W. H. Garming, M. Bolhuis, S. Conesa-Boj, P. Kruit, and J. P. Hoogenboom, *Lock-in Ultrafast Electron Microscopy Simultaneously Visualizes Carrier Recombination and Interface-Mediated Trapping*, *The Journal of Physical Chemistry Letters* (Oct., 2020) 8880–8886.

[122] M. W. H. Garming, I. G. C. Weppelman, M. Lee, T. Stavenga, and J. P. Hoogenboom, *Ultrafast scanning electron microscopy with sub-micrometer optical pump resolution*, *Applied Physics Reviews* **9** (June, 2022) 021418.

[123] M. W. Garming, P. Kruit, and J. P. Hoogenboom, *Imaging resonant micro-cantilever movement with ultrafast scanning electron microscopy*, *Review of Scientific Instruments* **93** (2022), no. 9.

[124] D.-S. Yang, O. F. Mohammed, and A. H. Zewail, *Scanning ultrafast electron microscopy*, *Proceedings of the National Academy of Sciences* **107** (Aug., 2010) 14993–14998.

[125] D. C. Joy, *Beam interactions, contrast and resolution in the sem*, *Journal of Microscopy* **136** (1984), no. 2 241–258.

[126] W. Ouyang, X. Zuo, and B. Liao, *Impact of photoexcitation on secondary electron emission: A Monte Carlo study*, *Journal of Applied Physics* **133** (Feb., 2023) 064301.

[127] E. Najafi, V. Ivanov, A. Zewail, and M. Bernardi, *Super-diffusion of excited carriers in semiconductors*, *Nature Communications* **8** (May, 2017) 15177.

[128] B. Liao, E. Najafi, H. Li, A. J. Minnich, and A. H. Zewail, *Photo-excited hot carrier dynamics in hydrogenated amorphous silicon imaged by 4D electron microscopy*, *Nature Nanotechnology* **12** (Sept., 2017) 871–876.

[129] J. Cho, T. Y. Hwang, and A. H. Zewail, *Visualization of carrier dynamics in p(n)-type GaAs by scanning ultrafast electron microscopy*, *Proceedings of the National Academy of Sciences* **111** (Feb., 2014) 2094–2099.

[130] Z. Zhang and J. T. Yates Jr, *Band bending in semiconductors: chemical and physical consequences at surfaces and interfaces*, *Chemical reviews* **112** (2012), no. 10 5520–5551.

[131] D. Perovic, M. Castell, A. Howie, C. Lavoie, T. Tiedje, and J. Cole, *Field-emission sem imaging of compositional and doping layer semiconductor superlattices*, *Ultramicroscopy* **58** (1995), no. 1 104–113.

[132] Y. Li, U. Choudhry, J. Ranasinghe, A. Ackerman, and B. Liao, *Probing Surface Photovoltage Effect Using Photoassisted Secondary Electron Emission*, *The Journal of Physical Chemistry A* **124** (June, 2020) 5246–5252.

[133] F. Humphreys, *Review grain and subgrain characterisation by electron backscatter diffraction*, *Journal of materials science* **36** (2001) 3833–3854.

[134] S. Zaefferer, *On the formation mechanisms, spatial resolution and intensity of backscatter kikuchi patterns*, *Ultramicroscopy* **107** (2007), no. 2-3 254–266.

[135] O. F. Mohammed, D.-S. Yang, S. K. Pal, and A. H. Zewail, *4D Scanning Ultrafast Electron Microscopy: Visualization of Materials Surface Dynamics*, *Journal of the American Chemical Society* **133** (May, 2011) 7708–7711.

[136] S. Meuret, M. S. Garcia, T. Coenen, E. Kieft, H. Zeijlemaker, M. Lätzel, S. Christiansen, S. Woo, Y. Ra, Z. Mi, *et. al.*, *Complementary cathodoluminescence lifetime imaging configurations in a scanning electron microscope*, *Ultramicroscopy* **197** (2019) 28–38.

[137] M. Solà-Garcia, K. W. Mauser, M. Liebtrau, T. Coenen, S. Christiansen, S. Meuret, and A. Polman, *Photon Statistics of Incoherent Cathodoluminescence with Continuous and Pulsed Electron Beams*, *ACS Photonics* **8** (Mar., 2021) 916–925.

[138] M. Solà-Garcia, S. Meuret, T. Coenen, and A. Polman, *Electron-Induced State Conversion in Diamond NV Centers Measured with Pump–Probe Cathodoluminescence Spectroscopy*, *ACS Photonics* **7** (Jan., 2020) 232–240.

[139] R. M. Feenstra and J. A. Stroscio, *Tunneling spectroscopy of the GaAs(110) surface*, *Journal of Vacuum Science & Technology B: Microelectronics Processing and Phenomena* **5** (July, 1987) 923–929.

[140] B. Sapoval and C. Hermann, *Physics of Semiconductors*. Springer Science & Business Media, Oct., 2003.

[141] H. Du, X. Lin, Z. Xu, and D. Chu, *Recent developments in black phosphorus transistors*, *Journal of Materials Chemistry C* **3** (Aug., 2015) 8760–8775.

[142] J. Kim, S. S. Baik, S. H. Ryu, Y. Sohn, S. Park, B.-G. Park, J. Denlinger, Y. Yi, H. J. Choi, and K. S. Kim, *Observation of tunable band gap and anisotropic Dirac semimetal state in black phosphorus*, *Science* **349** (Aug., 2015) 723–726.

[143] V. Tran, R. Soklaski, Y. Liang, and L. Yang, *Layer-controlled band gap and anisotropic excitons in few-layer black phosphorus*, *Physical Review B* **89** (June, 2014) 235319.

[144] A. Castellanos-Gomez, *Black Phosphorus: Narrow Gap, Wide Applications*, *The Journal of Physical Chemistry Letters* **6** (Nov., 2015) 4280–4291.

[145] X. Wang, A. M. Jones, K. L. Seyler, V. Tran, Y. Jia, H. Zhao, H. Wang, L. Yang, X. Xu, and F. Xia, *Highly anisotropic and robust excitons in monolayer black phosphorus*, *Nature Nanotechnology* **10** (June, 2015) 517–521.

[146] H. Liu, A. T. Neal, Z. Zhu, Z. Luo, X. Xu, D. Tománek, and P. D. Ye, *Phosphorene: An Unexplored 2D Semiconductor with a High Hole Mobility*, *ACS Nano* **8** (Apr., 2014) 4033–4041.

[147] B. Liao, J. Zhou, B. Qiu, M. S. Dresselhaus, and G. Chen, *Ab initio study of electron-phonon interaction in phosphorene*, *Physical Review B* **91** (June, 2015) 235419.

[148] E. Najafi, B. Liao, T. Scarborough, and A. Zewail, *Imaging surface acoustic wave dynamics in semiconducting polymers by scanning ultrafast electron microscopy*, *Ultramicroscopy* **184** (Jan., 2018) 46–50.

[149] W. van Roosbroeck and H. C. Casey, *Transport in Relaxation Semiconductors*, *Physical Review B* **5** (Mar., 1972) 2154–2175.

[150] J. Sun, V. A. Melnikov, J. I. Khan, and O. F. Mohammed, *Real-Space Imaging of Carrier Dynamics of Materials Surfaces by Second-Generation Four-Dimensional Scanning Ultrafast Electron Microscopy*, *The Journal of Physical Chemistry Letters* **6** (Oct., 2015) 3884–3890.

[151] B. S. Shaheen, J. Sun, D.-S. Yang, and O. F. Mohammed, *Spatiotemporal Observation of Electron-Impact Dynamics in Photovoltaic Materials Using 4D Electron Microscopy*, *The Journal of Physical Chemistry Letters* **8** (June, 2017) 2455–2462.

[152] J. I. Khan, A. Adhikari, J. Sun, D. Priante, R. Bose, B. S. Shaheen, T. K. Ng,

C. Zhao, O. M. Bakr, B. S. Ooi, and O. F. Mohammed, *Enhanced Optoelectronic Performance of a Passivated Nanowire-Based Device: Key Information from Real-Space Imaging Using 4D Electron Microscopy*, *Small* **12** (2016), no. 17 2313–2320.

[153] R. Bose, A. Adhikari, V. M. Burlakov, G. Liu, M. A. Haque, D. Priante, M. N. Hedhili, N. Wehbe, C. Zhao, H. Yang, T. K. Ng, A. Goriely, O. M. Bakr, T. Wu, B. S. Ooi, and O. F. Mohammed, *Imaging Localized Energy States in Silicon-Doped InGaN Nanowires Using 4D Electron Microscopy*, *ACS Energy Letters* **3** (Feb., 2018) 476–481.

[154] R. Bose, A. Bera, M. R. Parida, A. Adhikari, B. S. Shaheen, E. Alarousu, J. Sun, T. Wu, O. M. Bakr, and O. F. Mohammed, *Real-Space Mapping of Surface Trap States in CIGSe Nanocrystals Using 4D Electron Microscopy*, *Nano Letters* **16** (July, 2016) 4417–4423.

[155] G. Meizyte, R. Bose, A. Adhikari, J. Yin, M. A. Haque, M. R. Parida, M. N. Hedhili, T. Wu, O. M. Bakr, and O. F. Mohammed, *Imaging the Reduction of Electron Trap States in Shelled Copper Indium Gallium Selenide Nanocrystals Using Ultrafast Electron Microscopy*, *The Journal of Physical Chemistry C* **122** (July, 2018) 15010–15016.

[156] A. M. El-Zohry, B. S. Shaheen, V. M. Burlakov, J. Yin, M. N. Hedhili, S. Shikin, B. Ooi, O. M. Bakr, and O. F. Mohammed, *Extraordinary carrier diffusion on cdte surfaces uncovered by 4d electron microscopy*, *Chem* **5** (2019), no. 3 706–718.

[157] R. O. Nughays, C. Yang, S. Nematulloev, J. Yin, G. T. Harrison, J. Zhao, S. Fatayer, O. M. Bakr, and O. F. Mohammed, *Visualization of surface charge carrier diffusion lengths in different perovskite crystal orientations using 4d electron imaging*, *Advanced Optical Materials* **11** (2023), no. 10 2300190.

[158] D. Tuggle and L. Swanson, *Emission characteristics of the zro/w thermal field electron source*, *Journal of Vacuum Science & Technology B: Microelectronics Processing and Phenomena* **3** (1985), no. 1 220–223.

[159] M. Fransen, J. Faber, T. L. Van Rooy, P. Tiemeijer, and P. Kruit, *Experimental evaluation of the extended schottky model for zro/w electron emission*, *Journal of Vacuum Science & Technology B: Microelectronics and Nanometer Structures Processing, Measurement, and Phenomena* **16** (1998), no. 4 2063–2072.

[160] M. Bronsgeest and P. Kruit, *Temperature dependence of the work function of the zr/ o/ w (100) schottky electron source in typical operating conditions and its effect on beam brightness*, *Journal of Vacuum Science & Technology B:*

Microelectronics and Nanometer Structures Processing, Measurement, and Phenomena **24** (2006), no. 2 887–891.

[161] J. Orloff, *Handbook of charged particle optics*. CRC press, 2017.

[162] M. S. Bronsgeest, *Physics of schottky electron sources*, .

[163] K. Brown and G. Tautfest, *Faraday-cup monitors for high-energy electron beams*, *Review of Scientific Instruments* **27** (1956), no. 9 696–702.

[164] B. Barwick, C. Corder, J. Strohaber, N. Chandler-Smith, C. Uiterwaal, and H. Batelaan, *Laser-induced ultrafast electron emission from a field emission tip*, *New Journal of Physics* **9** (2007), no. 5 142.

[165] A. Gahlmann, S. T. Park, and A. H. Zewail, *Ultrashort electron pulses for diffraction, crystallography and microscopy: theoretical and experimental resolutions*, *Physical Chemistry Chemical Physics* **10** (2008), no. 20 2894–2909.

[166] C. Ropers, D. Solli, C. Schulz, C. Lienau, and T. Elsaesser, *Localized multiphoton emission of femtosecond electron pulses from metal nanotips*, *Physical review letters* **98** (2007), no. 4 043907.

[167] P. Hommelhoff, Y. Sortais, A. Aghajani-Talesh, and M. A. Kasevich, *Field emission tip as a nanometer source of free electron femtosecond pulses*, *Physical review letters* **96** (2006), no. 7 077401.

[168] D. Venus and M. Lee, *Polarization dependence of photoexcitation in photofield emission*, *Surface Science* **125** (1983), no. 2 452–472.

[169] L. Novotny, R. X. Bian, and X. S. Xie, *Theory of nanometric optical tweezers*, *Physical Review Letters* **79** (1997), no. 4 645.

[170] Y. C. Martin, H. F. Hamann, and H. K. Wickramasinghe, *Strength of the electric field in apertureless near-field optical microscopy*, *Journal of applied physics* **89** (2001), no. 10 5774–5778.

[171] X. Zhang, X. Cen, R. Ravichandran, L. A. Hughes, and K. van Benthem, *Simultaneous Scanning Electron Microscope Imaging of Topographical and Chemical Contrast Using In-Lens, In-Column, and Everhart-Thornley Detector Systems*, *Microscopy and Microanalysis: The Official Journal of Microscopy Society of America, Microbeam Analysis Society, Microscopical Society of Canada* **22** (June, 2016) 565–575.

[172] P. E. Russell and J. F. Mancuso, *Microchannel plate detector for low voltage scanning electron microscopes*, *Journal of Microscopy* **140** (1985), no. 3 323–330.

[173] M. T. Postek, W. J. Keery, and N. V. Frederick, *Low-profile high-efficiency microchannel-plate detector system for scanning electron microscopy applications*, *Review of Scientific Instruments* **61** (June, 1990) 1648–1657.

[174] T. E. Everhart and R. F. M. Thornley, *Wide-band detector for micro-microampere low-energy electron currents*, *Journal of Scientific Instruments* **37** (July, 1960) 246.

[175] L. Reimer, *Scanning Electron Microscopy: Physics of Image Formation and Microanalysis*, vol. 45 of *Springer Series in Optical Sciences*. Springer, Berlin, Heidelberg, 1998.

[176] J. A. Stratton, *Electromagnetic Theory*. McGraw Hill, 1941.

[177] K. M. McPeak, S. V. Jayanti, S. J. P. Kress, S. Meyer, S. Iotti, A. Rossinelli, and D. J. Norris, *Plasmonic Films Can Easily Be Better: Rules and Recipes*, *ACS Photonics* **2** (Mar., 2015) 326–333.

[178] R. Autrata, P. Schauer, J. Kvapil, and J. Kvapil, *A single crystal of YALO3: Ce3+ as a fast scintillator in SEM*, *Scanning* **5** (1983), no. 2 91–96.

[179] C. W. Oatley, *The detective quantum efficiency of the scintillator/photomultiplier in the scanning electron microscope*, *Journal of Microscopy* **139** (1985), no. 2 153–166.

[180] J. Pawley, *Performance of sem scintillation materials*, in *Scanning electron microscopy, 1974*, 1974.

[181] J. Lin, Q. Su, S. Wang, and H. Zhang, *Influence of crystal structure on the luminescence properties of bismuth(III), europium(III) and dysprosium(III) in Y2SiO5*, *Journal of Materials Chemistry* **6** (Jan., 1996) 265–269.

[182] K. L. Poff, U. Burkart, D.-P. Hauder, and R. D. Vierstra, *The Transmission of Combined Neutral Density Filters*, *Photochemistry and Photobiology* **39** (1984), no. 1 119–122.

[183] S. N. Mohammad, A. A. Salvador, and H. Morkoc, *Emerging gallium nitride based devices*, *Proceedings of the IEEE* **83** (1995), no. 10 1306–1355.

[184] S. Nakamura, M. Senoh, S.-i. Nagahama, N. Iwasa, T. Yamada, T. Matsushita, H. K. H. Kiyoku, and Y. S. Y. Sugimoto, *Ingan-based*

multi-quantum-well-structure laser diodes, *Japanese Journal of Applied Physics* **35** (1996), no. 1B L74.

[185] B. J. Baliga, *Gallium nitride devices for power electronic applications*, *Semiconductor Science and Technology* **28** (2013), no. 7 074011.

[186] K. J. Chen, O. Häberlen, A. Lidow, C. lin Tsai, T. Ueda, Y. Uemoto, and Y. Wu, *Gan-on-si power technology: Devices and applications*, *IEEE Transactions on Electron Devices* **64** (2017), no. 3 779–795.

[187] P. J. Treado, I. W. Levin, and E. N. Lewis, *Indium antimonide (insb) focal plane array (fpa) detection for near-infrared imaging microscopy*, *Applied spectroscopy* **48** (1994), no. 5 607–615.

[188] C. Grein, P. Young, M. Flatté, and H. Ehrenreich, *Long wavelength inas/ingasb infrared detectors: Optimization of carrier lifetimes*, *Journal of Applied Physics* **78** (1995), no. 12 7143–7152.

[189] P. Gu, M. Tani, S. Kono, K. Sakai, and X.-C. Zhang, *Study of terahertz radiation from InAs and InSb*, *Journal of Applied Physics* **91** (May, 2002) 5533–5537.

[190] R. Adomavičius, G. Molis, A. Krotkus, and V. Sirutkaitis, *Spectral dependencies of terahertz emission from inas and insb*, *Applied Physics Letters* **87** (2005), no. 26.

[191] J. S. Kang, M. Li, H. Wu, H. Nguyen, and Y. Hu, *Basic physical properties of cubic boron arsenide*, *Applied Physics Letters* **115** (Sept., 2019) 122103.

[192] T. Feng, L. Lindsay, and X. Ruan, *Four-phonon scattering significantly reduces intrinsic thermal conductivity of solids*, *Physical Review B* **96** (Oct., 2017) 161201.

[193] H. Welker and H. Weiss, *Group III-Group V Compounds*, in *Solid State Physics* (F. Seitz and D. Turnbull, eds.), vol. 3, pp. 1–78. Academic Press, Jan., 1956.

[194] J. A. Perri, S. La Placa, and B. Post, *New group III-group V compounds: BP and BAs*, *Acta Crystallographica* **11** (Apr., 1958) 310–310.

[195] P. Popper and T. A. Ingles, *Boron Phosphide, a III–V Compound of Zinc-Blende Structure*, *Nature* **179** (May, 1957) 1075–1075.

[196] F. V. Williams and R. A. Ruehrwein, *The Preparation and Properties of Boron Phosphides and Arsenides [1]*, *Journal of the American Chemical Society* **82** (Mar., 1960) 1330–1332.

[197] P. E. Grayson, J. T. Buford, and A. F. Armington, *Pressure Synthesis of Boron Phosphide and Boron Arsenide*. Air Force Cambridge Research Laboratories, Office of Aerospace Research, United States Air Force, 1966.

[198] A. F. Armington, *Vapor transport of boron, boron phosphide and boron arsenide*, *Journal of Crystal Growth* **1** (Jan., 1967) 47–48.

[199] T. L. Chu and A. E. Hyslop, *Crystal Growth and Properties of Boron Monoarsenide*, *Journal of Applied Physics* **43** (Feb., 1972) 276–279.

[200] T. L. Chu and A. E. Hyslop, *Preparation and Properties of Boron Arsenide Films*, *Journal of The Electrochemical Society* **121** (1974), no. 3 412.

[201] C. Prasad and M. Sahay, *Electronic Structure and Properties of Boron Phosphide and Boron Arsenide*, *physica status solidi (b)* **154** (1989), no. 1 201–207.

[202] C. L. Beckel, N. Lu, B. Abbott, and M. Yousaf, *Lattice vibrations of the icosahedral solid boron arsenide, B12As2*, *Inorganica Chimica Acta* **289** (June, 1999) 198–209.

[203] R. H. Wang, D. Zubia, T. O'Neil, D. Emin, T. Aselage, W. Zhang, and S. D. Hersee, *Chemical vapor deposition of B12As2 thin films on 6H-SiC*, *Journal of Electronic Materials* **29** (Nov., 2000) 1304–1306.

[204] Y. Gong, M. Tapajna, S. Bakalova, Y. Zhang, J. H. Edgar, Y. Zhang, M. Dudley, M. Hopkins, and M. Kuball, *Demonstration of boron arsenide heterojunctions: A radiation hard wide band gap semiconductor device*, *Applied Physics Letters* **96** (May, 2010) 223506.

[205] Y. Gong, Y. Zhang, M. Dudley, Y. Zhang, J. H. Edgar, P. J. Heard, and M. Kuball, *Thermal conductivity and Seebeck coefficients of icosahedral boron arsenide films on silicon carbide*, *Journal of Applied Physics* **108** (Oct., 2010) 084906.

[206] D. A. Broido, M. Malorny, G. Birner, N. Mingo, and D. A. Stewart, *Intrinsic lattice thermal conductivity of semiconductors from first principles*, *Applied Physics Letters* **91** (Dec., 2007) 231922.

[207] A. Ward, D. A. Broido, D. A. Stewart, and G. Deinzer, Ab Initio *theory of the lattice thermal conductivity in diamond*, *Physical Review B* **80** (Sept., 2009) 125203.

[208] L. Lindsay, W. Li, J. Carrete, N. Mingo, D. A. Broido, and T. L. Reinecke,

Phonon thermal transport in strained and unstrained graphene from first principles, *Physical Review B* **89** (Apr., 2014).

[209] L. Lindsay, D. A. Broido, and T. L. Reinecke, *First-Principles Determination of Ultrahigh Thermal Conductivity of Boron Arsenide: A Competitor for Diamond?*, *Physical Review Letters* **111** (July, 2013) 025901.

[210] B. Lv, Y. Lan, X. Wang, Q. Zhang, Y. Hu, A. J. Jacobson, D. Broido, G. Chen, Z. Ren, and C.-W. Chu, *Experimental study of the proposed super-thermal-conductor: BAs*, *Applied Physics Letters* **106** (Feb., 2015) 074105.

[211] N. H. Protik, J. Carrete, N. A. Katcho, N. Mingo, and D. Broido, Ab Initio *study of the effect of vacancies on the thermal conductivity of boron arsenide*, *Physical Review B* **94** (July, 2016) 045207.

[212] S. Li, Q. Zheng, Y. Lv, X. Liu, X. Wang, P. Y. Huang, D. G. Cahill, and B. Lv, *High thermal conductivity in cubic boron arsenide crystals*, *Science* **361** (Aug., 2018) 579–581.

[213] J. S. Kang, M. Li, H. Wu, H. Nguyen, and Y. Hu, *Experimental observation of high thermal conductivity in boron arsenide*, *Science* **361** (Aug., 2018) 575–578.

[214] F. Tian, B. Song, X. Chen, N. K. Ravichandran, Y. Lv, K. Chen, S. Sullivan, J. Kim, Y. Zhou, T.-H. Liu, M. Goni, Z. Ding, J. Sun, G. A. G. Udalamatta Gamage, H. Sun, H. Ziyaee, S. Huyan, L. Deng, J. Zhou, A. J. Schmidt, S. Chen, C.-W. Chu, P. Y. Huang, D. Broido, L. Shi, G. Chen, and Z. Ren, *Unusual high thermal conductivity in boron arsenide bulk crystals*, *Science* **361** (Aug., 2018) 582–585.

[215] J. S. Kang, M. Li, H. Wu, H. Nguyen, T. Aoki, and Y. Hu, *Integration of boron arsenide cooling substrates into gallium nitride devices*, *Nature Electronics* **4** (June, 2021) 416–423.

[216] B. Song, K. Chen, K. Bushick, K. A. Mengle, F. Tian, G. A. G. U. Gamage, Z. Ren, E. Kioupakis, and G. Chen, *Optical properties of cubic boron arsenide*, *Applied Physics Letters* **116** (Apr., 2020) 141903.

[217] H. Zhong, F. Pan, S. Yue, C. Qin, V. Hadjiev, F. Tian, X. Liu, F. Lin, Z. Wang, and J. Bao, *Idealizing tauc plot for accurate bandgap determination of semiconductor with ultraviolet–visible spectroscopy: A case study for cubic boron arsenide*, *The Journal of Physical Chemistry Letters* **14** (2023), no. 29 6702–6708.

[218] T.-H. Liu, B. Song, L. Meroueh, Z. Ding, Q. Song, J. Zhou, M. Li, and G. Chen,

Simultaneously high electron and hole mobilities in cubic boron-V compounds: BP, BAs, and BSb, *Physical Review B* **98** (Aug., 2018) 081203.

[219] Z. Y. Tian, Q. Y. Zhang, Y. W. Xiao, G. A. Gamage, F. Tian, S. Yue, V. G. Hadjiev, J. Bao, Z. Ren, E. Liang, and J. Zhao, *Ultraweak electron-phonon coupling strength in cubic boron arsenide unveiled by ultrafast dynamics*, *Physical Review B* **105** (May, 2022) 174306.

[220] J. Shin, G. A. Gamage, Z. Ding, K. Chen, F. Tian, X. Qian, J. Zhou, H. Lee, J. Zhou, L. Shi, T. Nguyen, F. Han, M. Li, D. Broido, A. Schmidt, Z. Ren, and G. Chen, *High ambipolar mobility in cubic boron arsenide*, *Science* **377** (July, 2022) 437–440.

[221] S. Yue, F. Tian, X. Sui, M. Mohebinia, X. Wu, T. Tong, Z. Wang, B. Wu, Q. Zhang, Z. Ren, J. Bao, and X. Liu, *High ambipolar mobility in cubic boron arsenide revealed by transient reflectivity microscopy*, *Science* **377** (July, 2022) 433–436.

[222] S. Sadasivam, M. K. Y. Chan, and P. Darancet, *Theory of Thermal Relaxation of Electrons in Semiconductors*, *Physical Review Letters* **119** (Sept., 2017) 136602.

[223] D. König, K. Casalenuovo, Y. Takeda, G. Conibeer, J. F. Guillemoles, R. Patterson, L. M. Huang, and M. A. Green, *Hot carrier solar cells: Principles, materials and design*, *Physica E: Low-dimensional Systems and Nanostructures* **42** (Sept., 2010) 2862–2866.

[224] L. Zhou, D. F. Swearer, C. Zhang, H. Robatjazi, H. Zhao, L. Henderson, L. Dong, P. Christopher, E. A. Carter, P. Nordlander, and N. J. Halas, *Quantifying hot carrier and thermal contributions in plasmonic photocatalysis*, *Science* **362** (Oct., 2018) 69–72.

[225] F. Tian, K. Luo, C. Xie, B. Liu, X. Liang, L. Wang, G. A. Gamage, H. Sun, H. Ziyaee, J. Sun, Z. Zhao, B. Xu, G. Gao, X.-F. Zhou, and Z. Ren, *Mechanical properties of boron arsenide single crystal*, *Applied Physics Letters* **114** (Apr., 2019) 131903.

[226] J. Buckeridge and D. O. Scanlon, *Electronic band structure and optical properties of boron arsenide*, *Physical Review Materials* **3** (May, 2019) 051601.

[227] X. Chen, C. Li, Y. Xu, A. Dolocan, G. Seward, A. Van Roekeghem, F. Tian, J. Xing, S. Guo, N. Ni, Z. Ren, J. Zhou, N. Mingo, D. Broido, and L. Shi, *Effects of Impurities on the Thermal and Electrical Transport Properties of Cubic Boron Arsenide*, *Chemistry of Materials* **33** (Sept., 2021) 6974–6982.

[228] F. Pan, G. A. G. Udalamatta Gamage, H. Sun, and Z. Ren, *Recent progress on cubic boron arsenide with ultrahigh thermal conductivity*, *Journal of Applied Physics* **131** (2022), no. 5.

[229] M. Fava, N. H. Protik, C. Li, N. K. Ravichandran, J. Carrete, A. van Roekeghem, G. K. H. Madsen, N. Mingo, and D. Broido, *How dopants limit the ultrahigh thermal conductivity of boron arsenide: A first principles study*, *npj Computational Materials* **7** (Apr., 2021) 1–7.

[230] K. Bushick, K. Mengle, N. Sanders, and E. Kioupakis, *Band structure and carrier effective masses of boron arsenide: Effects of quasiparticle and spin-orbit coupling corrections*, *Applied Physics Letters* **114** (Jan., 2019) 022101.

[231] S. Chae, K. Mengle, J. T. Heron, and E. Kioupakis, *Point defects and dopants of boron arsenide from first-principles calculations: Donor compensation and doping asymmetry*, *Applied Physics Letters* **113** (Nov., 2018) 212101.

[232] J. Kim, D. A. Evans, D. P. Sellan, O. M. Williams, E. Ou, A. H. Cowley, and L. Shi, *Thermal and thermoelectric transport measurements of an individual boron arsenide microstructure*, *Applied Physics Letters* **108** (May, 2016) 201905.

[233] G. A. Gamage, K. Chen, G. Chen, F. Tian, and Z. Ren, *Effect of nucleation sites on the growth and quality of single-crystal boron arsenide*, *Materials Today Physics* **11** (2019) 100160.

[234] T. Sjodin, H. Petek, and H.-L. Dai, *Ultrafast Carrier Dynamics in Silicon: A Two-Color Transient Reflection Grating Study on a (111) Surface*, *Physical Review Letters* **81** (Dec., 1998) 5664–5667.

[235] G. Grimvall, *The electron-phonon interaction in metals*, .

[236] G. Chen, *Nanoscale energy transport and conversion: a parallel treatment of electrons, molecules, phonons, and photons*. Oxford university press, 2005.

[237] G. Klatt, F. Hilser, W. Qiao, M. Beck, R. Gebs, A. Bartels, K. Huska, U. Lemmer, G. Bastian, M. B. Johnston, M. Fischer, J. Faist, and T. Dekorsy, *Terahertz emission from lateral photo-Dember currents*, *Optics Express* **18** (Mar., 2010) 4939–4947.

[238] E. Najafi, A. Jafari, and B. Liao, *Carrier density oscillation in the photoexcited semiconductor*, *Journal of Physics D: Applied Physics* **54** (Jan., 2021) 125102.

[239] J. H. de Boer and E. J. Verwey, *Semi-conductors with partially and with*

completely filled 3d-lattice bands, *Proceedings of the Physical Society* **49** (1937), no. 4S 59.

[240] N. Mott and R. Peierls, *Discussion of the paper by de boer and verwey*, *Proceedings of the Physical Society* **49** (1937), no. 4S 72.

[241] N. F. Mott, *The basis of the electron theory of metals, with special reference to the transition metals*, *Proceedings of the Physical Society. Section A* **62** (1949), no. 7 416.

[242] M. Cyrot, *Theory of mott transition: Applications to transition metal oxides*, *Journal de Physique* **33** (1972), no. 1 125–134.

[243] M. Imada, A. Fujimori, and Y. Tokura, *Metal-insulator transitions*, *Reviews of modern physics* **70** (1998), no. 4 1039.

[244] E. Greenberg, I. Leonov, S. Layek, Z. Konopkova, M. P. Pasternak, L. Dubrovinsky, R. Jeanloz, I. A. Abrikosov, and G. K. Rozenberg, *Pressure-induced site-selective mott insulator-metal transition in fe 2 o 3*, *Physical Review X* **8** (2018), no. 3 031059.

[245] J. Kokalj, *Bad-metallic behavior of doped mott insulators*, *Physical Review B* **95** (2017), no. 4 041110.

[246] M. Eckstein and P. Werner, *Photoinduced states in a mott insulator*, *Physical review letters* **110** (2013), no. 12 126401.

[247] A. Takahashi, H. Itoh, and M. Aihara, *Photoinduced insulator-metal transition in one-dimensional mott insulators*, *Physical Review B* **77** (2008), no. 20 205105.

[248] H. Okamoto, T. Miyagoe, K. Kobayashi, H. Uemura, H. Nishioka, H. Matsuzaki, A. Sawa, and Y. Tokura, *Photoinduced transition from mott insulator to metal in the undoped cuprates nd 2 cuo 4 and la 2 cuo 4*, *Physical Review B* **83** (2011), no. 12 125102.

[249] Z. He and A. J. Millis, *Photoinduced phase transitions in narrow-gap mott insulators: The case of vo 2*, *Physical Review B* **93** (2016), no. 11 115126.

[250] S. Iwai, M. Ono, A. Maeda, H. Matsuzaki, H. Kishida, H. Okamoto, and Y. Tokura, *Ultrafast optical switching to a metallic state by photoinduced mott transition in a halogen-bridged nickel-chain compound*, *Physical review letters* **91** (2003), no. 5 057401.

[251] K. W. Plumb, J. P. Clancy, L. J. Sandilands, V. V. Shankar, Y. F. Hu, K. S.

Burch, H.-Y. Kee, and Y.-J. Kim, α - *RuCl 3 : A spin-orbit assisted Mott insulator on a honeycomb lattice*, *Physical Review B* **90** (July, 2014) 041112.

[252] L. Binotto, I. Pollini, and G. Spinolo, *Optical and transport properties of the magnetic semiconductor α-RuCl3*, *physica status solidi (b)* **44** (1971), no. 1 245–252.

[253] I. Pollini, *Electronic properties of the narrow-band material α-rucl 3*, *Physical Review B* **53** (1996), no. 19 12769.

[254] A. Kitaev, *Anyons in an exactly solved model and beyond*, *Annals of Physics* **321** (Jan., 2006) 2–111, [cond-mat/0506438].

[255] A. Banerjee, J. Yan, J. Knolle, C. A. Bridges, M. B. Stone, M. D. Lumsden, D. G. Mandrus, D. A. Tennant, R. Moessner, and S. E. Nagler, *Neutron scattering in the proximate quantum spin liquid α-RuCl3*, *Science* **356** (June, 2017) 1055–1059.

[256] A. Y. Kitaev, *Fault-tolerant quantum computation by anyons*, *Annals of physics* **303** (2003), no. 1 2–30.

[257] C. Nayak, S. H. Simon, A. Stern, M. Freedman, and S. D. Sarma, *Non-abelian anyons and topological quantum computation*, *Reviews of Modern Physics* **80** (2008), no. 3 1083.

[258] S.-H. Do, S.-Y. Park, J. Yoshitake, J. Nasu, Y. Motome, Y. S. Kwon, D. T. Adroja, D. J. Voneshen, K. Kim, T.-H. Jang, J.-H. Park, K.-Y. Choi, and S. Ji, *Majorana fermions in the Kitaev quantum spin system α-RuCl3*, *Nature Physics* **13** (Nov., 2017) 1079–1084.

[259] T. Yokoi, S. Ma, Y. Kasahara, S. Kasahara, T. Shibauchi, N. Kurita, H. Tanaka, J. Nasu, Y. Motome, C. Hickey, *et. al.*, *Half-integer quantized anomalous thermal hall effect in the kitaev material candidate α-rucl3*, *Science* **373** (2021), no. 6554 568–572.

[260] A. Banerjee, P. Lampen-Kelley, J. Knolle, C. Balz, A. A. Aczel, B. Winn, Y. Liu, D. Pajerowski, J. Yan, C. A. Bridges, A. T. Savici, B. C. Chakoumakos, M. D. Lumsden, D. A. Tennant, R. Moessner, D. G. Mandrus, and S. E. Nagler, *Excitations in the field-induced quantum spin liquid state of α-RuCl3*, *npj Quantum Materials* **3** (Dec., 2018) 8.

[261] P. Czajka, T. Gao, M. Hirschberger, P. Lampen-Kelley, A. Banerjee, J. Yan, D. G. Mandrus, S. E. Nagler, and N. Ong, *Oscillations of the thermal conductivity in the spin-liquid state of α-rucl3*, *Nature Physics* **17** (2021), no. 8 915–919.

[262] Y. Tian, W. Gao, E. A. Henriksen, J. R. Chelikowsky, and L. Yang, *Optically driven magnetic phase transition of monolayer rucl3*, *Nano Letters* **19** (2019), no. 11 7673–7680.

[263] J. Zhang, N. Tancogne-Dejean, L. Xian, E. V. Bostrom, M. Claassen, D. M. Kennes, and A. Rubio, *Ultrafast spin dynamics and photoinduced insulator-to-metal transition in α-rucl3*, *Nano Letters* **23** (2023), no. 18 8712–8718.

[264] Y. Wang, J. Balgley, E. Gerber, M. Gray, N. Kumar, X. Lu, J.-Q. Yan, A. Fereidouni, R. Basnet, S. J. Yun, D. Suri, H. Kitadai, T. Taniguchi, K. Watanabe, X. Ling, J. Moodera, Y. H. Lee, H. O. H. Churchill, J. Hu, L. Yang, E.-A. Kim, D. G. Mandrus, E. A. Henriksen, and K. S. Burch, *Modulation Doping via a Two-Dimensional Atomic Crystalline Acceptor*, *Nano Letters* **20** (Dec., 2020) 8446–8452.

[265] U. Choudhry, F. Pan, X. He, B. Shaheen, T. Kim, R. Gnabasik, G. A. Gamage, H. Sun, A. Ackerman, D.-S. Yang, Z. Ren, and B. Liao, *Persistent hot carrier diffusion in boron arsenide single crystals imaged by ultrafast electron microscopy*, *Matter* **6** (Jan., 2023) 206–216.

[266] N. Strohmaier, D. Greif, R. Jördens, L. Tarruell, H. Moritz, T. Esslinger, R. Sensarma, D. Pekker, E. Altman, and E. Demler, *Observation of elastic doublon decay in the fermi-hubbard model*, *Physical review letters* **104** (2010), no. 8 080401.

[267] M. Eckstein and P. Werner, *Thermalization of a pump-excited mott insulator*, *Physical Review B* **84** (2011), no. 3 035122.

[268] R. Sensarma, D. Pekker, E. Altman, E. Demler, N. Strohmaier, D. Greif, R. Jördens, L. Tarruell, H. Moritz, and T. Esslinger, *Lifetime of double occupancies in the fermi-hubbard model*, *Physical Review B* **82** (2010), no. 22 224302.

[269] F. H. Essler, F. Gebhard, and E. Jeckelmann, *Excitons in one-dimensional mott insulators*, *Physical Review B* **64** (2001), no. 12 125119.

[270] D. Nevola, A. Bataller, A. Kumar, S. Sridhar, J. Frick, S. O'Donnell, H. Ade, P. A. Maggard, A. F. Kemper, K. Gundogdu, *et. al.*, *Timescales of excited state relaxation in α- ru cl 3 observed by time-resolved two-photon photoemission spectroscopy*, *Physical Review B* **103** (2021), no. 24 245105.

[271] K. Al-Hassanieh, F. A. Reboredo, A. Feiguin, I. González, and E. Dagotto,

Excitons in the one-dimensional hubbard model: a real-time study, *Physical review letters* **100** (2008), no. 16 166403.

[272] N. Bittner, D. Golež, M. Eckstein, and P. Werner, *Photoenhanced excitonic correlations in a mott insulator with nonlocal interactions*, *Physical Review B* **101** (2020), no. 8 085127.

[273] D. Lovinger, M. Brahlek, P. Kissin, D. Kennes, A. Millis, R. Engel-Herbert, and R. Averitt, *Influence of spin and orbital fluctuations on mott-hubbard exciton dynamics in lavo$_3$ thin films*, *Physical Review B* **102** (2020), no. 11 115143.

[274] L. Perfetti, P. A. Loukakos, M. Lisowski, U. Bovensiepen, M. Wolf, H. Berger, S. Biermann, and A. Georges, *Femtosecond dynamics of electronic states in the mott insulator 1t-tas2 by time resolved photoelectron spectroscopy*, *New Journal of Physics* **10** (2008), no. 5 053019.

[275] D. Wegkamp, M. Herzog, L. Xian, M. Gatti, P. Cudazzo, C. L. McGahan, R. E. Marvel, R. F. Haglund Jr, A. Rubio, M. Wolf, *et. al.*, *Instantaneous band gap collapse in photoexcited monoclinic vo 2 due to photocarrier doping*, *Physical review letters* **113** (2014), no. 21 216401.

[276] X. Wang, R. Y. Engel, I. Vaskivskyi, D. Turenne, V. Shokeen, A. Yaroslavtsev, O. Grånäs, R. Knut, J. O. Schunck, S. Dziarzhytski, *et. al.*, *Ultrafast manipulation of the nio antiferromagnetic order via sub-gap optical excitation*, *Faraday discussions* **237** (2022) 300–316.

[277] O. Grånäs, I. Vaskivskyi, X. Wang, P. Thunström, S. Ghimire, R. Knut, J. Söderström, L. Kjellsson, D. Turenne, R. Engel, *et. al.*, *Ultrafast modification of the electronic structure of a correlated insulator*, *Physical Review Research* **4** (2022), no. 3 L032030.

[278] F. Novelli, G. De Filippis, V. Cataudella, M. Esposito, I. Vergara, F. Cilento, E. Sindici, A. Amaricci, C. Giannetti, D. Prabhakaran, *et. al.*, *Witnessing the formation and relaxation of dressed quasi-particles in a strongly correlated electron system*, *Nature communications* **5** (2014), no. 1 5112.

[279] S. M. Gilbertson, T. Durakiewicz, G. L. Dakovski, Y. Li, J.-X. Zhu, S. D. Conradson, S. A. Trugman, and G. Rodriguez, *Ultrafast photoemission spectroscopy of the uranium dioxide uo 2 mott insulator: Evidence for a robust energy gap structure*, *Physical Review Letters* **112** (2014), no. 8 087402.

[280] V. Hadjiev, M. Iliev, B. Lv, Z. Ren, and C. Chu, *Anomalous vibrational properties of cubic boron arsenide*, *Physical Review B* **89** (2014), no. 2 024308.

[281] H. Sun, K. Chen, G. A. Gamage, H. Ziyaee, F. Wang, Y. Wang, V. G. Hadjiev, F. Tian, G. Chen, and Z. Ren, *Boron isotope effect on the thermal conductivity of boron arsenide single crystals*, *Materials Today Physics* **11** (2019) 100169.

[282] X. He, N. Punpongjareorn, C. Wu, I. A. Davydov, and D.-S. Yang, *Ultrafast carrier dynamics of cdte: surface effects*, *The Journal of Physical Chemistry C* **120** (2016), no. 17 9350–9356.

[283] W. E. Hoke, *Molecular-beam epitaxial growth of boron-doped GaAs films*, *Journal of Vacuum Science & Technology B: Microelectronics and Nanometer Structures* **11** (May, 1993) 902.

[284] P. A. Caban, D. Teklinska, P. P. Michalowski, J. Gaca, M. Wojcik, J. Grzonka, P. Ciepielewski, M. Mozdzonek, and J. M. Baranowski, *The role of hydrogen in carbon incorporation and surface roughness of MOCVD-grown thin boron nitride*, *Journal of Crystal Growth* **498** (Sept., 2018) 71–76.

[285] M. Odawara, T. Udagawa, and G. Shimaoka, *Organometallic Chemical Vapor Deposition Growth of Heterostructure of Wide Band Gap and Transparent Boron Phosphide on Silicon*, *Japanese Journal of Applied Physics* **44** (Jan., 2005) 681–683.

[286] M. A. Tischler, P. M. Mooney, B. D. Parker, F. Cardone, and M. S. Goorsky, *Metalorganic vapor phase epitaxy and characterization of boron-doped (Al,Ga)As*, *Journal of Applied Physics* **71** (Jan., 1992) 984–992.

[287] K. Bushick, S. Chae, Z. Deng, J. T. Heron, and E. Kioupakis, *Boron arsenide heterostructures: Lattice-matched heterointerfaces and strain effects on band alignments and mobility*, *npj Computational Materials* **6** (Dec., 2020) 3.

[288] S. Widmann, V. Tsurkan, D. A. Prishchenko, V. G. Mazurenko, A. A. Tsirlin, and A. Loidl, *Thermodynamic evidence of fractionalized excitations in α-rucl$_3$*, *Physical Review B* **99** (2019), no. 9 094415.